Antibody-Functionalized Nanoporous Surfaces Enable High Throughput Specific Cell Capture

by

Sukant Mittal

B.S. Biomedical Engineering, University of California, Irvine (2005)
S.M. Electrical Engineering and Computer Sciences, Massachusetts Institute of Technology (2008)

Submitted to the Harvard-MIT Division of Health Sciences and Technology
in partial fulfillment of the requirements for the degree of

Doctor of Philosophy in Medical and Electrical Engineering

at the

MASSACHUSETTS INSTITUTE OF TECHNOLOGY

June 2012

Signature of Author:____
Harvard-MIT Division of Health Sciences and Technology
May 17th, 2012

Certified by:____
Prof. Mehmet Toner
Harvard-MIT Division of Health Sciences and Technology, Massachusetts General Hospital
Thesis Supervisor

Accepted by:____
Prof. Ram Sasisekharan
Harvard-MIT Division of Health Sciences and Technology
Chairman, Committee for Graduate Students

Contents

List of Figures

List of Tables

Antibody-Functionalized Nanoporous Surfaces Enable High Throughput Specific Cell Capture

by

Sukant Mittal

Submitted to the Harvard-MIT Division of Health Sciences and Technology
in partial fulfillment of the requirements for the degree of
Doctor of Philosophy in Medical and Electrical Engineering

Abstract

Adhesion-based cell capture on surfaces in microfluidic devices forms the basis of numerous biomedical diagnostics and *in vitro* assays. Solid surface microfluidic platforms have been widely explored for biomedical diagnostics since samples can be precisely and reproducibly manipulated under well-defined physicochemical conditions. However, at these small length scales, the fluid dynamics are dominated by the high surface-to-volume ratio and interfacial phenomena limiting device performance at high flow rates. In contrast, cell homing to porous vasculature is highly effective *in vivo* during inflammation; stem cell trafficking and cancer metastasis. In this work, we demonstrate that fluid-permeable surface functionalized with cell-specific antibodies can promote efficient and selective cell capture *in vitro*. This architecture might be advantageous due to enhanced transport due to fluid field modification leading to diverted streamlines towards the surface. Moreover, specific cell-surface interactions can be promoted due to reduced shear, allowing gentle cell rolling and arrest. Together, these synergistic effects enable highly effective target cell capture at flow rates over an order of magnitude larger than existing devices with solid surfaces. Additionally, in this study, we overcome a major limitation relevant to porous surfaces due to formation of stagnant layers of cells from non-target background population. These stagnant layers are detrimental to device performance as they act to reduce interaction of the cells with the reactive surface thereby reducing capture efficiency. We theoretically and experimentally understand the mechanisms for formation of the stagnant bioparticle layer in microfluidic devices and define a parameter space for optimal operation of the device over long periods of time. Key insights from these studies, collectively allow us to design a spatially modified microfluidic devices that allow us to isolate cancer lines as low as 5 cells/mL spiked into buffy coat.

Thesis supervisor: Mehmet Toner

Title: Professor of Surgery and Health Sciences and Technology

Acknowledgements

Completion of this dissertation has been one of the key accomplishments in my life, and I owe my gratitude to several people who have helped me along the way.

First and foremost, I would like to thank my thesis committee for being very generous with their time and guidance steering the dissertation towards a fulfilling and a successful experience. My dissertation advisor, Prof. Mehmet Toner, whose wisdom, scientific knowledge and outlook on life has taught me valuable lessons that will help me in my future professional and personal life. Dissertation chair, Prof. Joel Voldman, who provided key insights on relevant problems inspiring essential modeling and experimental results. Dissertation committee members, Prof. William Deen, for his generous advice on modeling and interpretation of key mass transport phenomenon explored in the thesis and Prof. Hatice Altug, for her insights on key phenomenon occurring on porous surfaces. Collectively, the committee provided a fun and intellectual atmosphere for completion of this work making it truly an amazing experience!

Although, my thesis committee provided me with the tools to complete a successful dissertation, friends I met during this time deserve an equal mention. These are people with whom I shared the highs and lows of my Ph.D. on a daily basis. My long term roommates, Dipanjan Sen, Srikanth Patala, Bobak Mosadegh and HST friends: Antonio Molins, Mara MacDonald, Aleksandar Radovic Moreno, Divya Bolar, Miriam Makhlouf, Stephanie Piecewicz, Pamela Basto, Ming Zher Poh, Grace Chen, Ajay Shah and friends outside of the HST program Vivek Inder Sharma, Srujan Linga, Harish Sundaresh, Harry Sin have all shared this amazing experience with me. I am grateful for their friendship, advice and support over the years. I would also like to pay my gratitude to all members of the Center of Engineering and Medicine at Massachusetts General Hospital, who over the years have provided a collaborative and a amenable environment for working. Amongst these colleagues, I would like to give a special mention to post-doc extraordinaire Dr. Ian Wong, for his significant contributions in helping brainstorm ideas and representing data.

The last and biggest part of my gratitude goes to my family. No amount of words can justify their love and support. My father for his "pearls of wisdom", my mom for inculcating an amazing work ethic and teaching the importance of remaining humble, and my brother and sister in law for being my role models in life, I look up to them in the highest regard, professionally and personally. My amazingly talented girlfriend, Christina, for being patient, understanding and forever supportive and helping me tread through the complexities of PhD. I feel overjoyed and lucky to have a proud and loving family (grandparents, uncles and aunts) without whose support I could not have embraced this experience. Thank you all of you !!!

Chapter 1

Introduction

The efficient isolation of specific cells in lab-on-a-chip platforms is important for many applications in clinical diagnostics and biomedical research. These cells can be classified as prevalent cells (~10,000's cells in a mL of blood) or rare cells (~ as low as 1 cell in a mL of blood). Separating cells based on recognition of characteristic molecules, or more commonly known as, immuno-chromatography based separation, represents a highly specific way of isolating otherwise homogenous population of cells. In the past decade, a large number of microfluidic devices have been designed for isolating specific cells based on immuno-chromatography. However, these devices use solid surfaces for immobilization of moieties complimentary to the receptors on cells of interest. Use of solid surfaces poses certain critical challenges in capturing specific cells at high flow rates: The first limitation in this regime arises because the transport of analytes to the solid surface is slow compared to the speed of transport through the microfluidic device. This is particularly problematic at high flow rates due to rapid advection of analytes through the device (analogous to high Peclet number), as well as poor mixing of viscous flows (low Reynolds number). The second limitation subsequently arises because of insufficient time required for reaction of analytes with the surface. This is particularly problematic for cells moving rapidly across the surface, since they require the formation of multiple adhesive bonds between the characteristic molecules on the cell surface and the complimentary antibodies on the solid surface, to be fully arrested.

In this thesis, we study the effect of fluid permeable nano-porous membrane surface integrated in microfluidic devices on specific cell capture at high flow rates. We show that these fluid permeable surfaces allow for flow field modification, and allow bulk and surface cooperative mechanisms to efficiently isolate specific cells. Additionally, in this thesis we study the effect of background non-specific cells which lead to formation of stagnant 'cake' cell layers. These cake layers are reminiscent of many chemical engineering processes such as concentration of slurries in food and beverage industry, pretreatment of water and microbial separation in the biotechnology industry, and once formed significantly reduce capture efficiency of specific target cells. We model the transient and steady state conditions of stagnant cell layer formation and extend our findings to improve device design and alleviate the above mentioned problems. Further, simple device design and commercially available porous surfaces, allow scaling up of the device, which allow us to reach the goal of high throughput cell capture in microfluidic devices.

1.1 Motivation

The identification, selection and separation of a subpopulation of target cells from a larger heterogeneous population is essential for blood-based point-of-care diagnostics, personalized therapies and cell biology [9-11]. These cells of interest may be rare and present in extraordinarily low numbers relative to the general population, necessitating the processing of large sample volumes in order to accumulate a useful number. For instance, 1 mL of whole blood contains billions of red blood cells, millions of white blood cells, thousands of hematopoietic stem cells, hundreds of endothelial progenitor cells and dozens of circulating tumor cells (Fig. 1-1) [12, 13]. Thus, even a perfectly efficient separation scheme requires at least 10 mL of whole blood to capture a usable sample of the rarest cell types, which must be rapidly processed to limit degradation and provide timely information to patients.

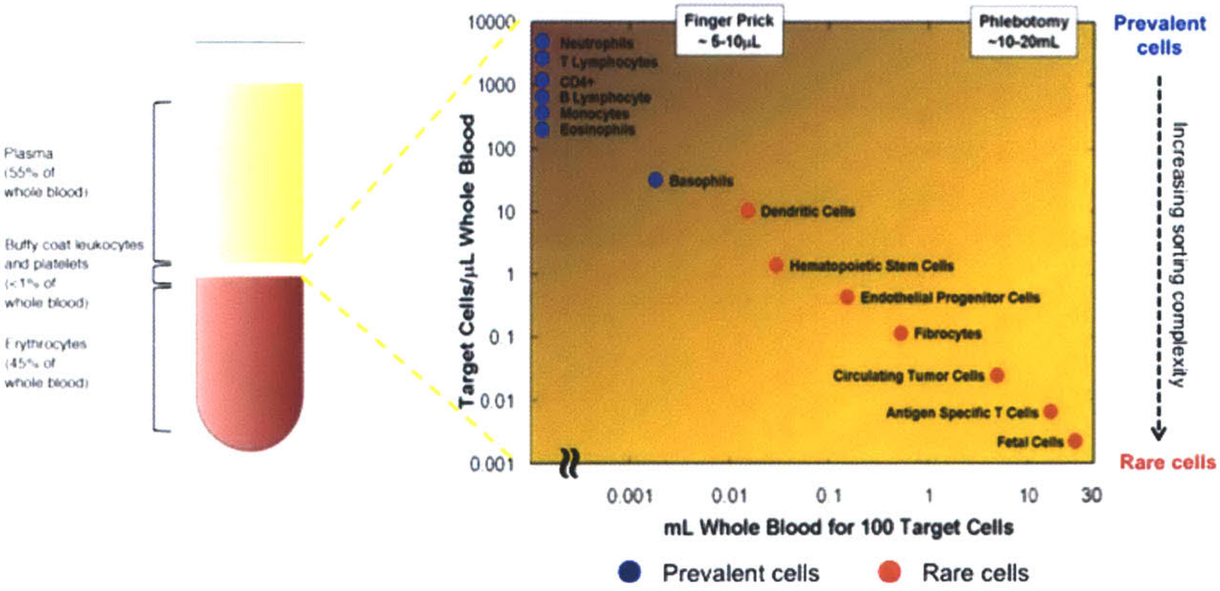

Fig. 1-1 Blood composition and frequency of rare cells for disease diagnosis

A number of approaches have been demonstrated to separate subpopulations of cells through their differential physical and biochemical phenotypes, which serve as "handles" for direct manipulation. For example, physical fields can partition a complex mixture of cells based on size, shape, deformability, density, electrical, magnetic or optical properties [10, 14]. These approaches are advantageous since they can be label-free and relatively high-throughput, but are often confounded by the considerable variability found even within a specific cell type. Instead, greater specificity can be achieved using molecular recognition of unique cell surface markers. Cells in solution can be labeled and subsequently sorted using fluorescent molecules [15] or magnetic beads [16]. Alternatively, cells can be captured on solid surfaces functionalized with ligands complementary to a specific cell surface receptor [17, 18]. This approach has been previously utilized to isolate neutrophils [19, 20], monocytes [20], lymphocytes [20-22], fibroblasts [23], endothelial progenitor cells [24], hematopoietic stem cells [25], mesenchymal stem cells [26] and circulating tumor cells [27-32]. In these schemes, specific cell adhesion depends on the interactions between the cell and surface, requiring the operating conditions to be carefully controlled.

Microfluidic platforms have been widely explored for biomedical diagnostics since samples can be precisely and reproducibly manipulated under well-defined physicochemical conditions. At these small length scales, the fluid dynamics are dominated by the high surface-to-volume ratio and interfacial phenomena [33, 34]. Although these effects have been cleverly exploited for various applications, they severely hinder throughput for analyte capture on solid surfaces [35, 36].

The first limitation in this regime arises because the transport of analytes to the surface may be too slow compared to the speed of transport through the microfluidic device. This is particularly problematic at high flow rates due to rapid advection of analytes through the device (analogous to high Peclet number), as well as poor mixing of viscous flows (low Reynolds number). These issues can be partially overcome by increasing the effective surface area [27, 30, 31], as well as using "herringbone" chaotic micromixers to disrupt fluidic streamlines through the microfluidic device [28, 29, 37].

The second limitation subsequently arises if the reaction of analytes with the surface does not have sufficient time to occur. This is particularly problematic for cells moving rapidly across the surface, since they require the formation of multiple adhesive bonds to be fully arrested [38]. Indeed, any bonds that do form between cellular receptors and surface-immobilized ligands are more likely to dissociate at high shear rates [39]. On the other hand, a certain threshold shear rate is necessary for adhesion-based capture to occur selectively [17], since weaker non-specific molecular bonds are pulled apart more easily. This mechanism has been used to select for certain subpopulations with differential expression levels using a precisely controlled shear rate [21, 22]. Another danger is that cell sedimentation may dominate at low flow rates, which would further decrease selectivity. Overall, the effectiveness of adhesion-based capture is limited at high flow rates both by transport of cells to the surface as well as the subsequent reaction of cells with the surface.

Here, we show that microfluidic devices incorporating porous, fluid-permeable surfaces functionalized with cell-specific antibodies can be used to capture a rare subpopulation of target cells with excellent efficiency, selectivity and throughput. The effectiveness of this platform arises both from enhanced mass transport to the porous surface, as well as enhanced cell-surface interactions that promote dynamic rolling adhesion with high specificity. These cooperative mechanisms enable optimum performance at extremely fast flow rates. These flow rates are over an order of magnitude faster than what can be achieved with conventional devices.

1.2 Thesis Structure

This thesis introduces the incorporation and use of antibody functionalized porous surfaces for specific cell capture at high flow rates and their advantage over the solid counterparts. Chapter 2 highlights some of the major advancements on the macro- and micro- scale lab on chip cell separation systems. We highlight some of the most prevalent methods of cell separation with a specific focus on immuno-chromatography based methods. Additionally in this chapter, we introduce the reader to the current use of porous surfaces in biology and cell separation. An understanding of the limitations of these current platforms elucidates the motivation for this thesis.

In chapter 3, we describe the fabrication methodology for incorporating commercially available nano-porous surfaces into the micro-fluidic devices. Methods to sandwich porous surfaces in microfluidic devices have previously been described. However, in order to allow large flow rates in these channels, we optimize one of these methods to insure device integrity during the course of these experiments. Additionally, in chapter 3 we investigate different known functionalization strategies for different porous surface materials and optimize the pore sizes needed to achieve enhanced mass transport and surface interactions of cells with the surface without physical trapping of cells within the pores. Additionally, we introduce and describe different modes of device operation that are a characteristic of every experiment. Lastly, we develop a lumped resistance model for the two-layered porous surface device which describes the use of high external resistances in reliably performing the experiments and measurement of the device function through fluid flux measurements. This model is the mainstay of replicating capture efficiency results, even in the presence of porous surface variations in commercially available membranes.

In Chapter 4, the effectiveness of the two channel micro-fluidic platform with sandwiched porous surface platform to capture specific cells is studied. An analytical model for cell transport to the porous surface using Faxen's Law is developed allowing insight into the linear relationship between permeation flux through the porous surface and the total percentage of cells that get convected to the porous surface. Once on the surface, we understand the motion of unencumbered cells on the porous surface and derive an analytical expression that highlights the reduced velocity of cells on porous surface and compare it to Goldman's equation for particle rolling close to a solid wall. Additionally, we present a state diagram generated from experimental conditions that elaborates the rolling velocity of cells on porous surfaces as a function of shear stress and permeation flux. The state space model explains the equivalency relationship that exists between shear and permeation flux for different channel dimensions thereby providing a general rule of thumb for designing devices, depending on the desired application. We utilize these results to demonstrate the effectiveness of porous surface in capturing various cell lines and demonstrate that the flow rates under which capture takes place is over an order of magnitude faster than what can be achieved with conventional devices. Capture of different cancer cell lines with varying levels of surface antigens demonstrates the versatility of the device in capturing cells with low and high expressing Ep-CAM receptors.

Lastly, we compare the theoretical and the experimental rate of capture of in our device using the Bell model.

Chapter 5 studies the effect of permeation flux on target cell capture efficiency in the presence of significantly larger number of non-specific background cells. Using prior work from Romero and Davis, a steady state and transient model for formation of stagnant 'cake' cell layer on the surface is studied which allows optimization of controllable operational parameters such as fluid shear stress, permeation flux and cell feed concentration for and avoiding the detrimental effects of stagnant layer formation on rare specific cell capture. In this chapter, careful study of the phenomenon allowed us to understand the inevitable dependence of the cake layer formation on the porous surface on cell feed fraction and permeation flux. In our study, we find two mechanisms responsible for formation of the stagnant layer. Firstly, the critical distance from the entrance beyond which the shear rate is not strong enough to sweep non-specifically captured particles tangentially. Secondly, we investigate and alleviate the reduction in translational shear forces due to wall effects. Temporal data on stagnant layer formation indicates that even under optimal critical distance conditions, microfluidic channel "edge effects" reduce shear at the edges and promote white blood cell layer formation. By engineering nano-pore distributions through a channel width we control these "wall effects" and shift the tangential shear to permeation flux ratio back into the optimal regime. We extend the same principal into a multi-channel indented microfluidic device where we demonstrate capture efficiency of ~70% for rare cancer cell numbers (~5 cells /mL) by processing ~48 mL of sample in 1 hr.

Chapter 6 summarizes the main findings of the previous chapters and provides suggestions for future directions. In this chapter we discuss the exciting possibilities that have opened up as a result of the insights developed through the theoretical and experimental analysis of results in this thesis. Firstly, the use of the system developed during this thesis in conjunction with the developed theory towards a multiplexed cell arrest device can allow for understanding of interactions between the cell antigens and the complimentary antibodies. These studies can shed light on important properties of cells, the complimentary antibodies and the interactions between them that lead to "arrest" or "no arrest" modes. Secondly, the same device can be used for building an in-vitro model for cell trafficking usually encountered in bio-mimetic settings during cancer cell chemotaxis and leukocyte homing and finally, the rigorous understanding of the fluidic forces in this thesis can enable us to engineer a “perfect” porous surface using silicon nitride substrate which can enable isolation of rare cells from clinical samples in an extremely well controlled manner thereby providing opportunity for clinical application.

Chapter 2

Background and Prior Work

Identification, detection and separation of cells from complex mixtures such as blood and sputum have become the mainstay for diagnosis and prognosis of many diseases [21, 40-43]. Low numbers of these cells in some cases such as, circulating tumor cells in cancer, antigen specific T cells in tuberculosis and fetal cells in prenatal diagnosis necessitate the use of large volumes of these samples in order to accumulate a useful number for diagnosis. In this chapter we will focus on macro and micro scale technologies that leverage different physical as well as bio-chemical properties of cells for identification and isolation. Section 2.1 will discuss some of the traditional macro- techniques used in clinical, research and industrial settings for large volume sample processing and discuss their advantages and disadvantages. In section 2.2, we explore microfluidic technologies that leverage the use of forces unique and effective on micron scales for cell separation. In section 2.3 we introduce separation of specific cells on the principles of immunochromatography and discuss different variants of this technique (FACS, MACS) on macro scale. Section 2.4 explores the use of microfluidic devices for specific cell capture in microfluidic devices. Section 2.5 discusses the historical account of porous surfaces in microfluidic and their use in immonochromatography based capture. Finally, section 2.6 we discuss limitations in currently microfluidic particle separation technologies and how our work with nano-porous surfaces in microfluidics has the potential to overcome some of these challenges.

2.1 Macroscale separation based on physical properties

Importance of bioparticle separation has led to development of several techniques on a clinical (Centrifugation), industrial (Filtration) and research (Electrophoresis) level in the past century. In this section we will discuss some of the most prevalent and commonly used techniques that leverage physical properties of bioparticles for separation. Traditional macroscale technologies techniques primarily make use of physical properties such as size, shape and density and mobility induced by electric field forces. These techniques are usually used as pre-concentration techniques upstream of the more specific techniques. Even though these pre-concentration techniques are able to process large volumes of samples in a short time (aka high throughput), they suffer from severe lack of sensitivity and specificity in samples that have low target cell numbers, rendering them unsuitable for use. A few examples of the most common techniques are elucidated in this section.

Centrifugation: Often used as the first step in preparation of biological samples, centrifugation has established its position in the clinical and research settings as one of the most instrumental tools for separation of bioparticles on the basis of size and density. Sophisticated ultracentrifuge machines today can generate centrifugal forces on the order of $1\text{x}10^6$g, thereby expediting sample processing and increasing resolution of bioparticle detection on the basis of size and relative density difference of the bioparticle and the media (Fig. 2-1a). The method of centrifugation accelerates the process of sedimentation of various cellular components in the sample and allows concentration of bioparticles with similar size and density in "bands"(Fig. 2-1b). Improvements over this initial principal have been achieved by using density enhancing media such as (1) Ficoll (a polysaccharide media used for separation blood into its cellular components) and (2) Percoll (a coilloidal silica media used for separating cells, viruses and organelles), and sugar media such as sucrose.

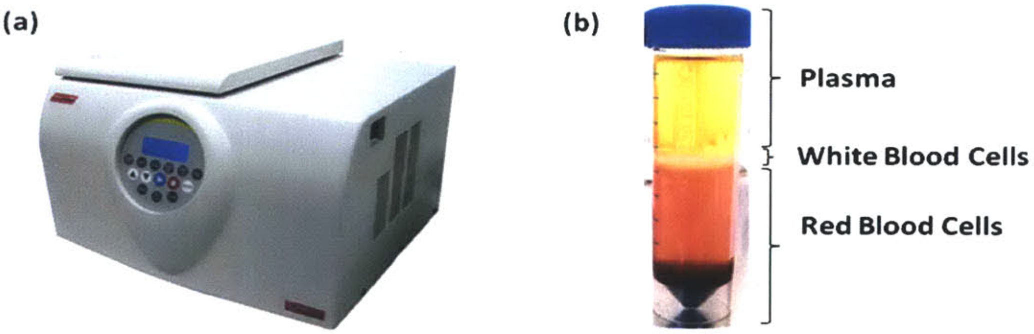

Fig. 2-1 (a) Modern day ultracentrifuge **(b)** Bands of different components of blood after ultracentrifugation

Size Based Filtration: Size based filtration using porous surfaces is one of the most commonly used methods to separate mixture of bioparticle populations based on size and shape differential and when the biomolecular properties of the cells are not well known. Flowing a sample through the device bearing the porous surface, bioparticles larger than the pore size are unable to pass through the surface and get retained on the surface, whereas the smaller sized bioparticles pass through with ease (Fig.2-2a). Due to operational ease and its scalability, size based filtration has been utilized in large scale industrial applications such as separation of bacteria and viruses from water in water [1] and colloidal particles in coal slurries [44], and clinical applications such as toxins from blood in hemodialysis [2]. One major disadvantage of this configuration of filtration is the rapid deterioration of the device performance due to blocking of pores as a consequence of particle retention [1]. We will discuss the mechanisms behind fouling and blockage of these pores in Chapter 4 and discuss ways to assuage it.

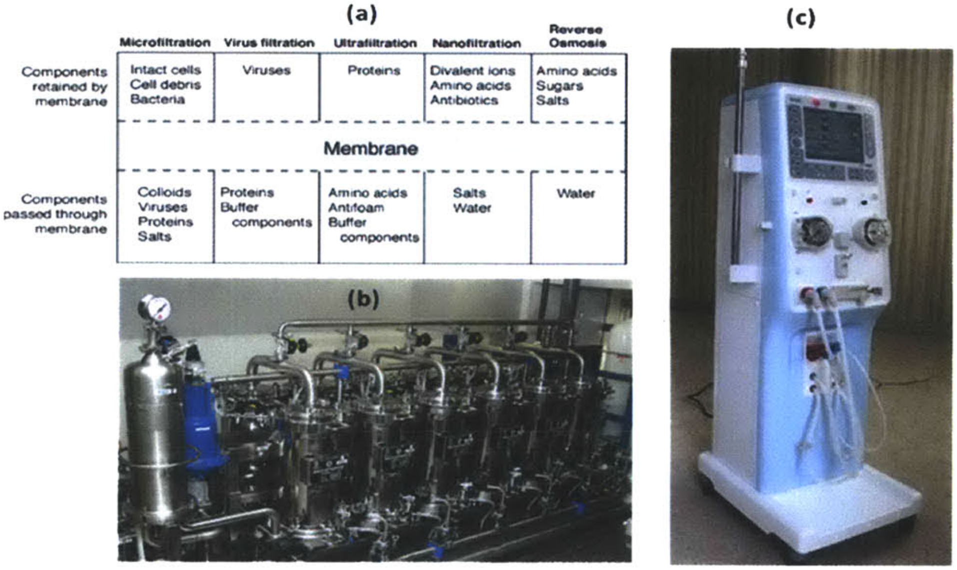

	Microfiltration	Virus filtration	Ultrafiltration	Nanofiltration	Reverse Osmosis
Components retained by membrane	Intact cells Cell debris Bacteria	Viruses	Proteins	Divalent ions Amino acids Antibiotics	Amino acids Sugars Salts
Components passed through membrane	Colloids Viruses Proteins Salts	Proteins Buffer components	Amino acids Antifoam Buffer components	Salts Water	Water

Fig. 2-2: (a) Comparison of removal characteristics of different pressure driven membrane processes [1] **(b)** Large scale industrial modules containing porous surfaces for removal of bacteria from water [1] **(c)** Modern day hemo-dialysis machine for removal of toxins from blood using 15 nm porous surface [2]

2.2 Microscale bioparticle separation techniques based on physical characteristics

Use of microfabrication techniques in designing devices over the past few decades has opened up possibilities to exploit optical, dielectrophoretic, acoustic and fluidic forces, , which become relevant and powerful on the length scales of the bioparticle. These forces allow accurate manipulation of the local bioparticle environment down to the single particle level. Although selective, weak nature of some of these manipulative forces limits throughput of sample processing.

Optical manipulation: Optical forces provide a precise, non-contact and contamination free method to identify and select cells from a mixture. The most common technique utilized using this principle is optical tweezers where a focused laser confines dielectric particles in a 3 dimensional environment and imparts attractive or repulsive forces based on the mismatch of the refractive indices [45, 46]. Manipulation of bioparticles from a few angstroms to ten's of microns is possible using this technique.

Dielectrophoretic manipulation (DEP): Dielectrophoretic manipulation of cells is analogous to optical forces. The dielectrophoretic manipulation force depends on the clausius-mossotti factor, which takes into account the dielectric constants of the bioparticle and the surrounding media in a non-uniform magnetic field that imparts attractive or repulsive forces. The phenomenon was first described in the 1950s by Henry Pohl and since has been utilized by many groups to sort cells. Use of microfabrication techniques allow fabrication of electrodes of various materials that generate well controlled non-uniform electric fields. One such example is the use in a microcytometer where an array of electrodes use dielectrophorretic forces to hold the cells in place as the surrounding media flows by and the optical system luminiscently interrogates the held particle for identification [47]. These forces have also been used to pattern and concentrate bioparticles ranging a few microns upto ten's of microns [3, 48, 49].

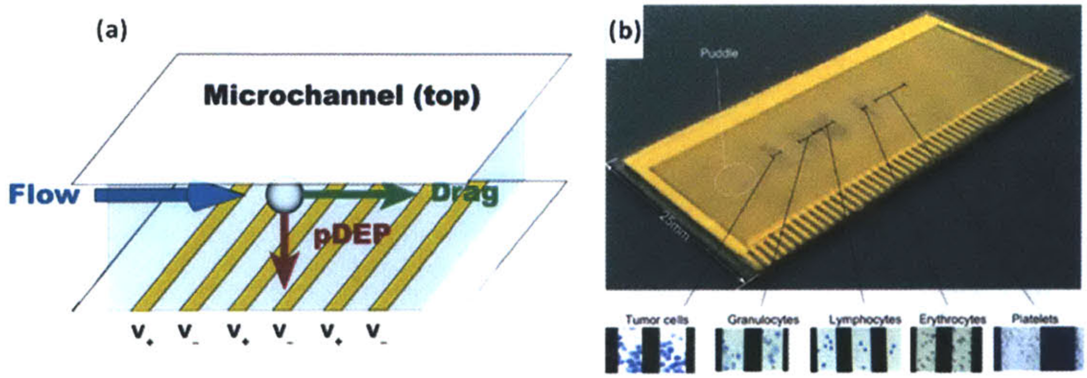

Fig. 2-3: (a) Schematic of the interdigitated electrodes and DEP forces with respect the sample flow **(b)** fractionation of tumor cells and other blood components on the DEP chip [3]

Acoustic manipulation : Acoustic sorting provides yet another method for bioparticle sorting, concentration and patterning by application of externally controllable field [50-52]. In this method, ultrasonic standing waves produce stationary pressure gradients at well defined intervals (nodes) which in liquid medium imparts radial forces to position cells at specific intervals i.e. at the nodes. Concerns over cell due to the radial force and rise in temperature have been raised. However, a recent study by Johanson shows that the amount of force on the bioparticles is ~ 0.5 nN, which is similar to the forces applied using optical and dielectrophoretic forces [53]. Additionally, acoustic forces provide a higher continuous throughput over the optical and dielectrophoretic external fields.

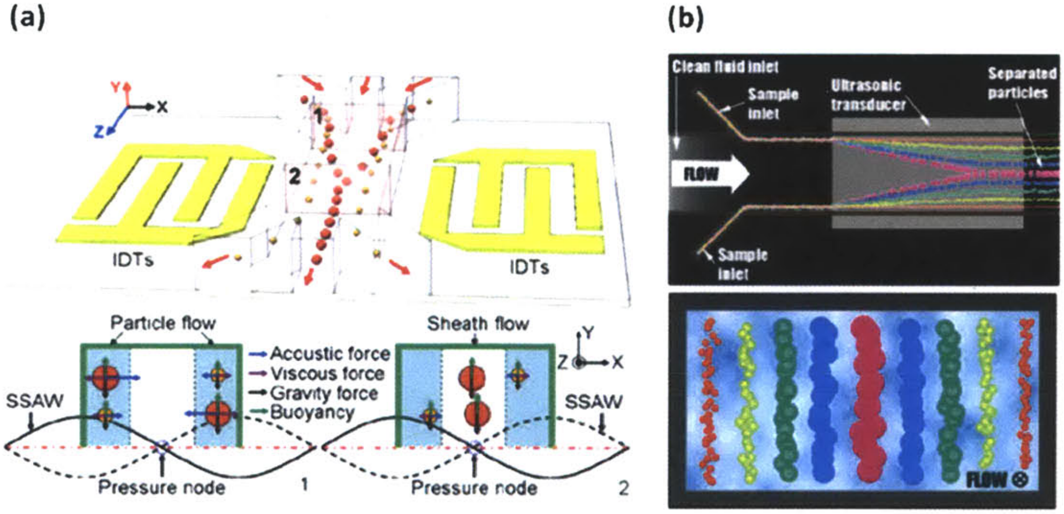

Fig. 2-4: **(a)** Schematic illustrating the principle of acoustic separation by standing surface acoustic waves (SSAW) generated using interdigital transducers (IDT). The varying acoustic forces repositions the larger cells closer to the channel center and smaller cells farther from the center **(b)** Cells of varying sizes align at distinct positions across the microchannel cross-section based on the acoustic primary radiation force experienced.

Fluid force manipulation : One of the biggest advantages of miniaturization of the existing macro scale cell sorting principles is in manipulation of fluid forces. Laminar flows simplify the Navier-Stokes equations and therefore allow understanding and control of bioparticles in microfluidic channels through clever design.

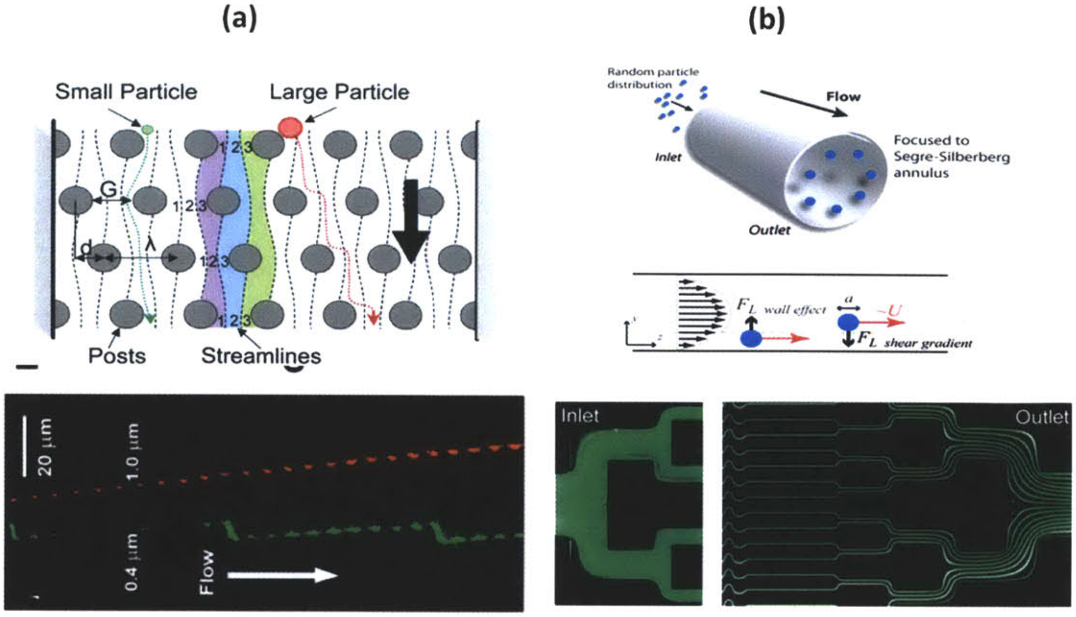

Fig. 2-5: (a) Top schematic shows asymmetric obstacles separating out particles of different size. The bottom figure shows separation of 0.4 µm and 1 µm beads and the respective trajectories. **(b)** Top schematic shows the focusing of particle in an annulus. The middle figure illustrated the different forces that determine the eullibrium position of focusing and the bottom figure shows focusing of fluorescent fluid in the microfluidic channels.

Deterministic hydrodynamics make use of low Reynolds number laminar flows ($Re \ll 1$) in microfluidic devices. The approach makes use of the asymmetric bifurcations which act as obstructions to the particle in the flow direction (Fig. 2-5a). Based on the size and deformability, separation of RBC's, WBC's, bacteria and solid latex particles have been achieved [54, 55].

In contrast to the low Reynolds number regime used for deterministic lateral displacement where viscous forces dominate over inertial forces, for large Reynolds number ($Re > 1$), the vice versa is true. These conditions can be achieved at high flow rates, which enable high throughput processing of samples. These inertial forces tend to push or 'focus' the particles in the channel to equilibrium positions which are determined by Reynolds number, ratio of the particle diameter to channel dimensions and the shape of the particles (fig. 2-5b). Several groups have studied this phenomenon and reported the optimal regimes under which this focusing is high quality [56-58]. Applications of inertial focusing have been used in making micro-scale flow cytometers [59].

2. 3 Separation of bioparticles based on specific biomolecular recognition

Separation using specific biomolecular recognition ("affinity chromatography") exploits use of unique markers on surfaces of cells of interest. In contrast to the purely physical methods of separation, this technique is highly specific and allows differentiation between cells that are otherwise similar in shape, size and density. Selected complimentary molecules identify the surface markers on target cells by forming biochemical bonds. Various methods have been devised in order to leverage this technique identifying and sorting target cells in solution (FACS and MACS) or on a fixed substrate. Some of the most famous ones are discussed in this section.

Flow activated cell sorting: Fluorescence activated cell sorting (FACS) is widely used in laboratory and clinics. Due to its high sensitivity and mature technology, FACS has become the technique of choice to use commercially [60]. The target cells are focused using sheath flow around the sample injection port to file the cells in the sample within a confined region. The cells are identified via the fluorescent markers tagged onto the complimentary molecules that bind to the surface markers or cytosolic proteins (Fig. 2-6a). The detector in the FACS detects the presence or absence of the fluorescent signal from each cell and records it [4]. Whereas there are several advantages to FACS some of the limitations include clogging, contamination, cell viability and the expensive nature of the instrument. In order to alleviate some of the above mentioned disadvantages, various groups have developed a microfluidic versions of flow cytometers. One typical format of a μ-flow cytometer is the T-junction design where, similar to the original FACS, sample is injected through one port and the sheath flow provides a narrow band of ordered cells which can be interrogated one at a time by the detected. Another variation is generation of droplets that encapsulate cells in order to preserve cells from excessive shear and maintain viability (Fig. 2-6b). Besides, portability, cheap cost and ability to parallelize these devices to increase throughput, microfluidics reduces the drag experienced by the cells due to droplet switching compared to flow switching in its macro counterpart [61].

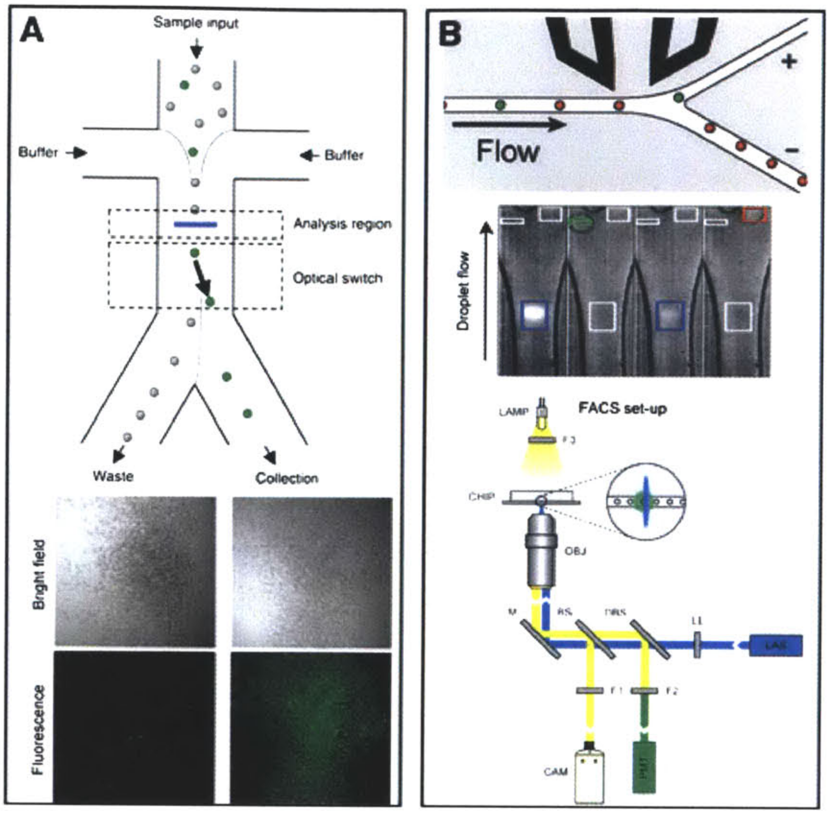

Fig. 2-6 (a) FACS schematic illustrating the principle of FACS **(b)** Variation of the original FACS principal where droplets are generated encapsulating cells are generated to preserve cells from excessive shear at high flow rates [4].

Magnetically activated cell sorting: A variant to FACS is Magnetically Activated Cell Sorting (MACS), where magnetic beads instead of fluorescence, bear the recognition molecule that label the target cells [62]. Once labeled with magnetic beads, the target cells are picked out from the general population by using a magnetic field gradient. One of the advantages of MACS lies in the flexibility of its application in either batch or continuous processing modes on large scales. Batch processing involves placement of magnets next to a column containing ferromagnetic material where alternating presence and absence of magnetic fields collects the cells [63]. In continuous processing, a quadrapole magnet is placed next to liquid columns and cell solution flows through the column. Cells attached to magnetic beads get deflected, whereas the others flow straight through [64]. Similar devices are also implemented in microfluidic formats. These microfluidic MACS devices can be broadly classified into two categories: active and passive traps. In active traps, electrical power is used to generate the desired magnetic field characteristics through on-chip electromagnets (Fig. 2-7a). In contrast, a passive trap uses a permanent magnet, with on chip iron or nickel elements acting as field gradient concentrators (Fig. 2-7b) [65, 66]. Advantages to MACS include the possibility of collecting large number of target cells at the same time and low cost. However, some of the drawbacks include time consuming and sensitive process of labeling the cells with magnetic beads, low sensitivity and removal of unbound beads [16].

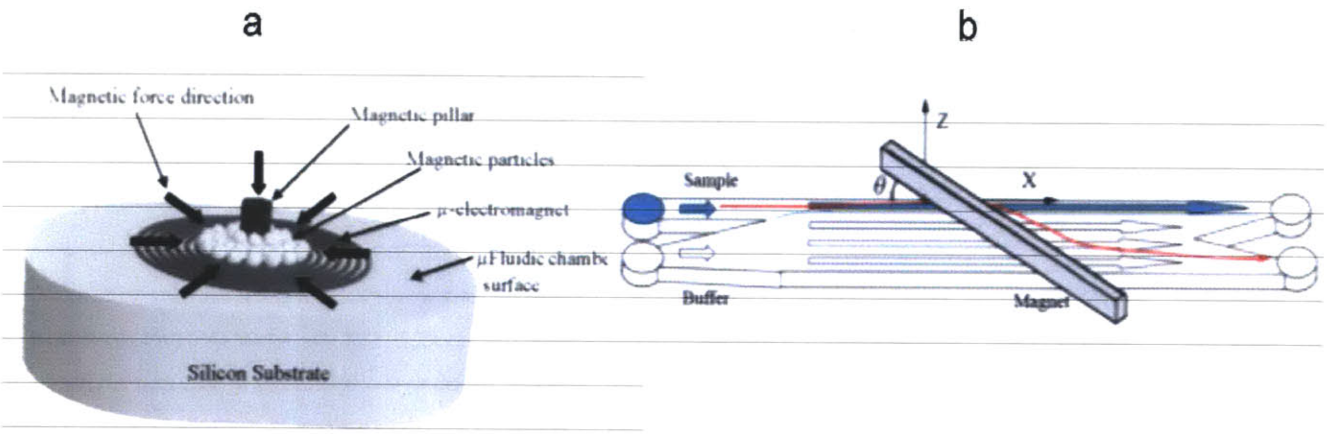

Fig. 2-7 (a) Active method of magnetically activated cell separation using on chip fabricated coils [5] **(b)** Schematic of passive MACS using an external magnetic to deflect magnetically attached cells [6].

2.4 Immunochromatography separation using microfluidic devices

Use of specific cells through biomolecular recognition has recently become popular due to the recent developments in the field of microtechnology, which have opened up avenues for studying chemical and biological samples in microfluidic devices, and have started playing important roles in tissue engineering, neurobiology, cell biology and cell sorting. Sensitivity of immunochromatography is increased by the use of microfluidic devices, where microenvironments can be controlled precisely in order to facilitate the biochemical reactions between the complimentary molecules. In contrast to capturing target particles in solution like in FACS/MACS, specific cell capture can be achieved by immobilizing complimentary molecules on the solid surfaces of the microfluidic devices. By controlling the fluidic forces in the microfluidic laminar regime, several groups have used clever design to isolate target cells from the general population. This methodology has several advantages over the FACS or MACS method of separation using immunochromatography. Firstly, capturing cells on microfluidic solid surfaces does not require pre-mixing of the samples with labels such as magnetic beads and fluorophores. Secondly, Capturing cells on solid surfaces allows for simple addition of subsequent steps for cell lysis, detection and amplification. Thirdly, expensive and bulky components such as lasers and permanent magnets are not required. Lastly, being able to control the fluid dynamics in microfluidic device allows greater reliability in results.

Within a microfluidic device several factors such as shear stress, surface topography and concentration, specificity and concentration of immobilized adhesive molecules as well as the target cell type affect cell adhesion in microfluidic devices. Various groups have optimized functionalization with the adhesive molecules in order to maximize cell capture [67-70]. For all these affinity based microfluidic devices, the sample is processed in two steps. The first step, "capture step", aims at capturing the specific cells, whereas the second step, "washing step", removes the non-specifically bound cells on the surface using a washing buffer solution.

Likewise, models describing flow characteristics of the fluid on cell capture for various device designs have been studied. For example Cheng and colleagues developed a straight rectangular channel device with immobilized anti-CD4 immobilized on the surfaces using silence chemistry. The study demonstrated the capability of the device to separate CD4+ T cells. Optimization of the shear stress under which only CD4+ T cells would stick but not the CD4+ monocytes was characterized in this study (Fig. 2-8a) [71]. However, this device geometry suffers from mass transport problems at high flow rate, which reduce the ability of the target cells to contact the reactive surface. This is a big hurdle in cases where the number of cells in the sample is rare (<100 cells/mL) (Section 2.4). By making parallel channels this problem can be partially alleviated, however it comes at the cost of increasing real estate and hence larger area over which rare cells need to be detected (Fig. 2-8b). In order to increase the encounter between the target cells and hence the sensitivity of the device, pillars (Fig. 2-8c) [40] and "herringbone"[72] (Fig. 2-8d) like structures functionalized with specific antibodies are built on the microfluidic surface. These devices modify the parallel streamlines in the straight channel and allow greater interaction of cells with the antibody covered surface. These devices demonstrate ability to capture small numbers of circulating tumor cells from whole blood. However, like the flat channel devices these devices also suffer from capture of specific cells at low flow rates. In order to alleviate the low flow rates in these devices (< 0.3 mL/hr) parallel channels are fabricated. As microfluidics provide a predictable fluidics environment, Adams. et. al. desgined curvy channels of small dimensions (30 μm x 45 μm) using deen flows to enhance specific cell capture (Fig. 2-8e) [35] and Yang et. al. designed a combinatorial chip consiting of pillar and herring bone pieces that allow for modified streamlines towards the surfaces even in the laminar flow regime (Fig. 2-8f) [37]. For all of the above mentioned microfluidic devices, the sample is processed in two steps. The first step involves optimizing for the ideal fluid conditions to capture specific cells. The second step, consists of using a washing buffer to "wash away" all the loosely bound cells on the surface to increase purity of capture.

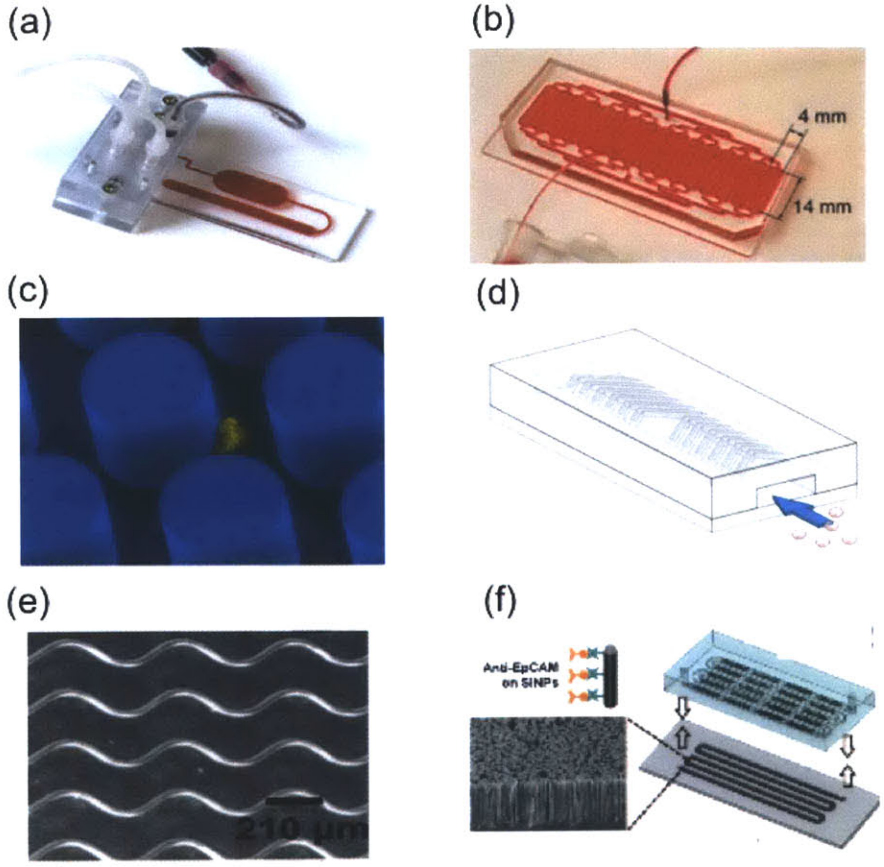

Fig. 2-8 **(a)** Schematic of a single straight rectangular microfuidic channel and fluid streamlines. **(b)** Multiple straight rectangular channels with blood in order to improve throughput **(c)** SEM of a cancer cell immobilized on an EpCAM coated micro-Silicon pillar **(d)** Schematic of "herring bone" indentations modifying fluid and particles streamlines to increase interaction with the

antibody coated surface **(e)** Narrow curved channels fabricated using fluidic forces to capture cells **(f)** Hi aspect ratio CNT forests ("tiny" pillars) developed in conjunction with the herring bone top to enhance specific cell capture.

2.5 Historical use of Porous Surfaces in Microfluidic Devices

Conventionally, solid materials such as glass, silicon, gold and polymers have been used in microfluidic devices. However, recent developments in rigid substrates such as carbon nanotubes as well as innovations in highly controlled porous membranes and monoliths have inspired construction of devices integrating porous surfaces. Incorporation of porous elements have found applications in cell culture, basic chemotaxis studies, microdialysis, tissue engineering and filtration [73]. In this section, we describe a broad class of porous used for cell separation.

Carbon Nanotubes: Carbon Nanotubes (CNT's) have been used in a wide range of biomedical applications because of their unique electrical, thermal and surface properties and biocompatibility with biological samples. Application in most of these areas make use of covalent [74] and non-covalent [75, 76] methods of functionalizing biomolecules to the CNT surface. For example, Chen et. al. modify fluid fields by patterned antibody functionalized CNT forests permeable to fluid, to increase "interception efficiency" and specific cell capture efficiency of various size bioparticles by 6 fold [7]. CNT forests provide an unprecedented increase in surface area while maintaining a high porosity (~99%) because of stable structure formations, even at high aspect ratio (Fig. 2-9 a,b,c). Additionally, CNT fibers exhibit unique semi-conductive properties and allow label free detection of charged biomolecules by acting as field effect transistors and creating gating effects [77, 78]. CNT's have also been explored as drug delivery vehicles. They possess the unique property of getting internalized by mammalian cells and have therefore been used for chemical and thermal destruction of cancerous cells [79, 80]. Despite its functional uses, CNT integration into microfluidic devices for specific bioparticle separation at high flow rates remains cumbersome and unreliable due to their brittle nature, involved growth and fabrication, and limited scalability.

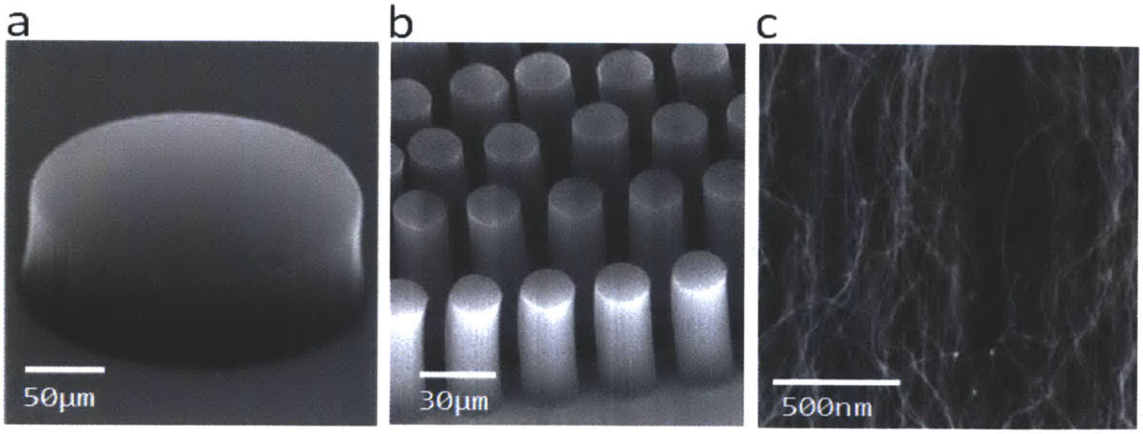

Fig. 2-9 Scanning electron micrographs (SEMs) of patterned VACNT elements **(a)** A 200μm diameter single post **(b)** An array of 20μm diameter posts **(c)** Nanostructure of a VACNT forest [7]

Monoliths: Porous monoliths have been traditionally fabricated inside microfluidic devices by injecting polymer solutions, which are then polymerized using free radicals and UV initiation. Monoliths with different porosities (30% - 70%) can be synthesized by varying the concentrations of organic solvents, monomers and free radical initiators [81]. Applications of porous monoliths, include size based filtration, efficient mixing, and antibody-based specific bioparticle capture, and are similar to the macro scale chromatography columns using solid supports (Fig. 2-10). Even though monoliths provide an easy method for forming random porous structures inside microfluidic devices, diversity in porosity and flow dynamics lead to considerable variability in specific cell capture from device to the other.

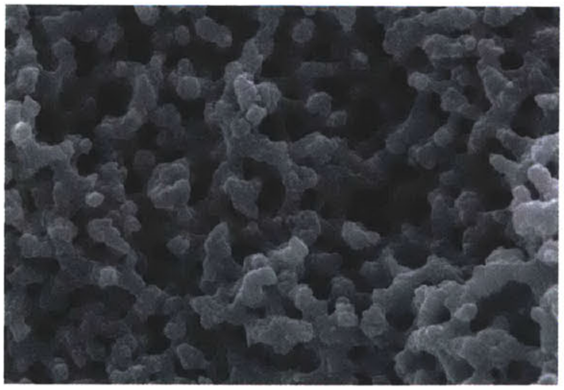

Fig. 2-10 Scanning electron micrograph of a porous monolith formed inside a microfluidic channel using UV initiation.

Porous membranes: Membranes are the most widely used porous surface in microfluidic devices due to ease of integration, scalability, low cost and a large range of selection of commercial "off the shelf" application specific surface chemistries. Briefly, two kinds of porous membranes are commercially available. Track etched membranes are formed when high energy ionic particles are bombarded through polymers like polycarbonate, Teflon etc and create through holes in the substrate (Fig. 2-11a).The second type of membranes are the mesh membranes with interwoven fibers. These membranes allow fluid to pass through normally as well as tangentially and are usually thicker than the track etched membranes (Fig. 2-11b). These porous surfaces allow passage of fluid normal to the surface through these holes. Successful incorporation of membranes in microfluidic devices requires leakage free integration. While most microfluidic devices use "glue, alignment and clamp" method [82], photochemical methods have also been developed to achieve constructs that can withstand pressures greater than 200 kPa without leaking or bursting [83]. De Jong et. al. provide a comprehensive review of how to select a membrane focusing on the material, structural type and integration techniques [73]. These integration techniques have opened possibilities for pre-concentration, purification, microdialysis, chemotaxis and vascularization studies over a long period of time using microfluidics [73]. Even with the advent of other exciting applications mentioned in previous sections, size based filtration of bioparticles remains the most common use of porous membranes in microfluidics. For example, Kim et al. [84] integrate different functions on a microfluidic device by removing of cells from blood, separating of HDL, and signal generation on a enzyme embedded membrane by using multiple membranes. However, like other size based separation methods described in section 2.5, the filtration achieved with porous membranes does not give specific particle selection.

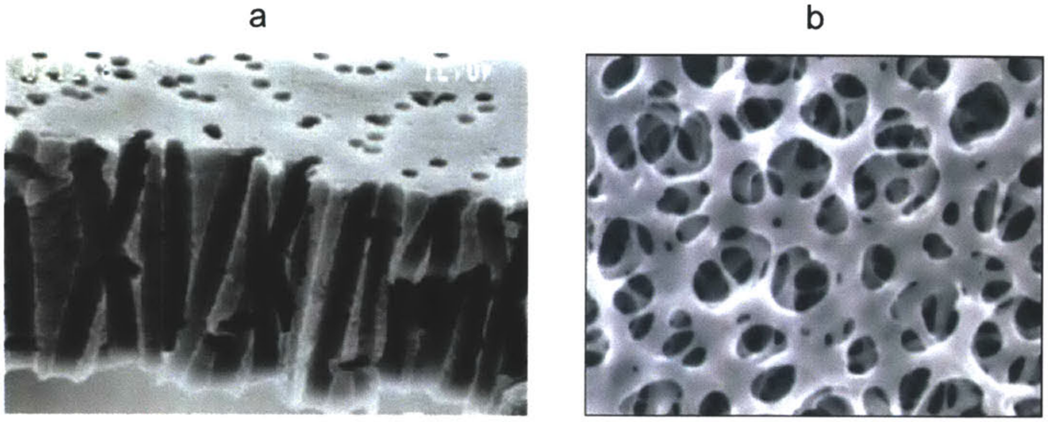

Fig. 2-11 (a) Scanning electron microscopy of a track etched polycarbonate membrane **(b)** SEM of a cellulose mesh type porous surface

2.6 Some Limitations of current microfluidic devices in cell sorting

Over the past decade, the field of microfluidics has revolutionized cell sorting. As discussed in sections 2.2, 2.4 and 2.5, microfluidics has provided scientists with the ability to cleverly control flow characteristics, use low sample volumes and automate assays. However, depending on the cells of interest, the number of rare target cells available for capture varies greatly in a milliliter of blood. For example 1 mL of blood on an average contains 10,000 dendritic cells, but only has ~ 20 circulating tumor cells and less than 5 fetal cells (Fig. 2-13). This necessitates large volume of sample to be processed in order to accumulate a useful number of cells, which requires high sample flow rates in the device. Sample processing at high flow rates poses three critical challenges: (1) Decreased transport of cells to the reactive surface (2) High shear stress and decreased interaction time of cells with the reactive surface (3) Formation of stagnant layers of non-specific cells on porous surface precluding optimal performance.

Mass Transport Limitation: The first limitation at flow rates arises because the transport of analytes to the surface may be too slow compared to the speed of transport through the microfluidic device. This is particularly problematic at high flow rates due to rapid advection of analytes through the device (analogous to high Peclet number), as well as poor mixing of viscous flows (low Reynolds number). These issues can be partially overcome by increasing the effective surface area [27, 30, 31], as well as using "herringbone" chaotic micromixers to disrupt fluidic streamlines through the microfluidic device [28, 29, 37]. In this thesis, we describe the use of porous surface to enhance mass transport towards the antibody functionalized reactive surface.

Receptor-Antibody Reaction Limitation: The second limitation subsequently arises if the reaction of analytes with the surface does have sufficient time to occur. This is particularly problematic for cells moving rapidly across the surface, since they require the formation of multiple adhesive bonds to be fully arrested [38]. Indeed, any bonds that do form between cellular receptors and surface-immobilized ligands are more likely to dissociate at high shear rates [39]. On the other hand, a certain threshold shear rate is necessary for adhesion-based capture to occur selectively [17], since weaker non-specific molecular bonds are pulled apart more easily. This mechanism has been used to select for certain subpopulations with differential expression levels using a precisely controlled shear rate [21, 22]. Another danger is that cell sedimentation may dominate at low flow rates, which would further decrease selectivity. Overall, the effectiveness of adhesion-based capture is limited at high flow rates both by transport of cells to the surface as well as the subsequent reaction of cells with the surface. In Chapter 4 we define an optimal regime where enhanced mass transport to the surface and adhesion-based capture of selective cells co-exist.

Stagnant Layer Formation on Porous Surfaces: When operating at high flow rates without being transport limited on porous surfaces, a different complication arises - excess build-up and fouling of cells, known as concentration polarization and "caking" [85]. This is a well known issue encountered during separation processes that completely remove all solid particles, such as those based on cross-flow filtration [86]. Indeed, a number of hydrodynamic mechanisms have been explored to suppress cake formation at high concentrations and throughput, including surface roughness, inertial lift, pulsatile (unsteady) flows, and Dean flows [87]. Unfortunately, these schemes cannot be easily applied to selective separation, since the enhanced local shear could also remove captured target cells. In this thesis, an in depth discussion on the machanisms responsible for stagnant layer formation, its impact on specific cell capture and modification of spatially modulated microflows that restore optimal functioning are discussed in this thesis.

2.6 Summary

In this chapter we discuss the importance of cell separation and its myriad applications in biomedical engineering and biology. We discuss various macro- and microtechnology tools currently available for separating out cells based on physical, electrical and biochemical properties and emphasize the advantages and disadvantages of each. Given the focus of this thesis and specificity of cell separation based on molecular recognition we dive deeper into the limitations of the current solid surfaces microfluidic devices that seek to leverage this property for cell separation. Broadly, solid surface microfluidic devices do not offer high sample processing throughput thereby limiting practical applications for applications where large volume of sample requires processing. Consequently, we introduce the previous use of porous surfaces in microfluidic devices and discuss the limitations, mostly attributed to the formation of stagnant layers which decrease device performance over a large period of time. Together, introduction to all these concepts set up the motivation for this thesis " *Nanoporous Surfaces Enable High Throughput Specific Cell Capture*".

Chapter 3

Integration and characterization of nanoporous membranes in microfluidic devices

In this chapter, we describe the integration and characterization methodology used for incorporating commercially available nano-porous surfaces into the micro-fluidic devices. Methods to sandwich porous surfaces in microfluidic devices have previously been described and since the primary objective of this thesis is to process samples at high flow rates, we optimize one of the existing fabrication strategies to insure device integrity in section 3.1. Additionally, in Section 3.2 we investigate different known functionalization strategies for porous surfaces. In section 3.3 we optimize the pore sizes needed to achieve enhanced mass transport and surface interactions of cells with the surface without physical trapping of cells within the pores. In section 3.4, we develop a lumped resistance model for the two-layered porous surface device which describes the use of high external resistances. Lastly, in section 3.5 we use the lumped resistor model developed in Section 3.6 to perform permeability experiments and measure fluid flux through the porous surface as a function of pressure. This model is the mainstay of replicating capture efficiency results, even in the presence of porous surface variations in commercially available membranes.

3.1 Integration of porous membranes in microfluidic devices

Integrating porous membranes in microfluidic devices has been of significant interest over the past decade due to the diversity of applications described in section 2.5. Many different approaches have been reported to integrate membranes in microfluidics. They can broadly be classified into four categories: (1) In-situ preparation of membranes [88, 89] (2) membrane preparation as a part of the chip fabrication process [90, 91] (3) Use of membrane properties of the bulk material [92] (4) Direct incorporation of the commercial membranes [82, 93, 94]. Due to the availability of a large number of specified parameters (pore size, membrane thickness) and range of membrane in commercial membranes, direct incorporation using clamping or gluing has become an attractive option.

The microfluidic channels are fabricated using soft lithography technique [95]. Briefly, the PDMS prepolymer (Sylgard 184, Dow Corning NY) was mixed with the curing agent in a weight ratio of 10 (pre-polymer):1 (curing agent). The mixture was cast onto a 4 in. silicon wafer with positive relief features with a height of 100μm and cured at 60°C. The cured PDMS was peeled from the silicon wafer and holes were punched at the inlets and outlets of the device (Fig. 3-1). Uncured PDMS mortar is used to bond the PDMS Channels and the membrane together. To create the PDMS mortar layers, PDMS and toluene were mixed at predetermined mass ratios and the mixture was de-gassed in a vacuum chamber to remove any bubbles. The toluene-diluted PDMS mortar was spun onto the glass cover slides at 1500 rpm for 1 min. The PDMS devices channels were stamped onto the spun uncured PDMS mortar and pressed gently for 2 min. The membranes (GE-Whatman, CT) were cut to the desired dimensions, placed gently over the bottom microfluidic channel and straightened out carefully using tweezers. Because the dimesion of the porous surface area is defined by the overlap of the top channel and the bottom channel, the top channel is carefully aligned under a microscope for precise alignment. The construct is left overnight in the oven at 70°C.

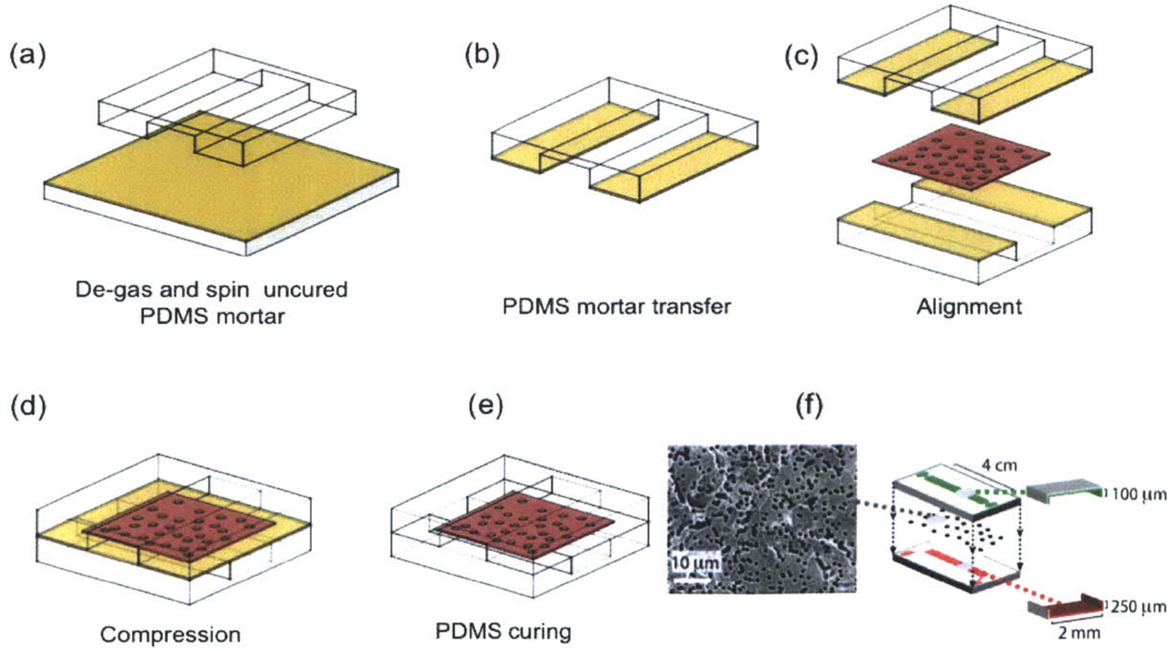

Fig. 3-1 (a) Negative photoresist (SU-8, MicroChem) was photolithographically patterned on silicon wafers to create masters. The masters were then used as molds, on which polydimethylsiloxane (PDMS) prepolymer mixed with its crosslinker at 10 : 1 weight ratio was poured, degassed, and allowed to cure in a conventional oven at 65 °C for 24 h before removal from the molds. Next, a thin layer of uncured PDMS diluted in toluene (50% v/v) was spun 1800 rpm for 1 min onto a glass slide using a high-speed spinner. **(b)** The thin layer of PDMS was transferred onto the channel surfaces by gently stamping the PDMS channel onto the uncured PDMS. **(c)** The polycarbonate membrane was gently placed over the bottom channel first and then the top channel was carefully aligned over it. **(d)** Gentle compression applied using a clamp **(e)** The device constructs was allowed to sit at room temperature overnight to cure at 70°C. **(f)** Exploded view of the porous surface device with dimensions

3.1.1 Uncured PDMS binding mortar thickness optimization

For successful integration of the membrane and sealing of the construct that can withstand large pressures, it is important to optimize the thickness of the uncured bonding PDMS mortar transferred to the surface of the PDMS channels in. Unless care is taken, air pockets can form at the edges of the membrane when the membrane is sandwiched between the two PDMS pieces and compromise the pressure that the device can withstand. Specifically, the combined PDMS mortar thickness on the upper and lower PDMS pieces should be sufficient to penetrate through the pores and form a stable bond, yet not too thick to flow into the channels. Additionally, it is important that the mortar thickness transferred to each of the cured PDMS channels should be at least the height of the membrane (~ 10 μm). The thickness of the mortar transferred can be changed by varying the spin speed. As seen in Fig. 3-2, for a given spin speed, the thickness of the mortar transferred decreases as the spin speed increases and saturates at ~ 3 μm above 2500 rpm for PDMS : Toluene ratio of 1:1 by mass. This saturation thickness is reached earlier (~1500 rpm) for PDMS : Toluene ratio of 1:2. Thickness of the PDMS mortar transferred was measured by making a cut was through the cured PDMS mortar and the original PDMS channel slab. This construct was then visualized under an inverted microscope with a 40 X objective (Nikon TIE). The measurements were calibrated by using a reference of a known thickness.

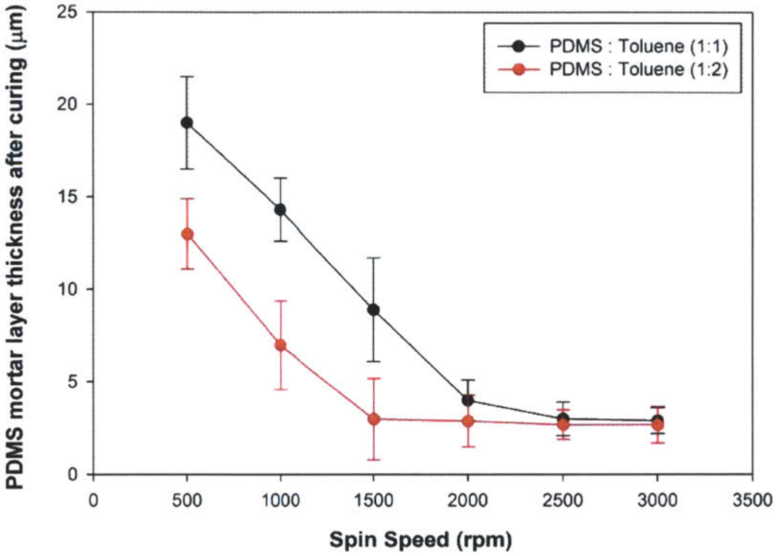

Fig. 3-2 PDMS mortar thickness transferred to the PDMS slabs as a function of spin speed

3.1.2 Device strength characterization

To measure the burst strength of different mortar thicknesses, the channels were filled with Fluroscien Isothiocynate (FITC) dye and the top channel outlet and the bottom channel inlet were clamped. The dye solution was introduced into the top channel though the top inlet using a constant pressure pump and was allowed to pass through the membrane and exit through the bottom outlet. For each mortar thickness, the input pressure was increased in steps and the channel was viewed under the microscope till FITC starting leaking out of the boundaries defined by the top and bottom channels. The burst pressure increases with the increase in uncured mortar thickness transferred (Fig. 3-3), due to more stable bond formation across the membrane, and saturates at mortar transfer ~ 15 µm (burst strength ~ 350 Kpa). The saturation pressure is reached due to the physical limit of cured PDMS bond strength [96].

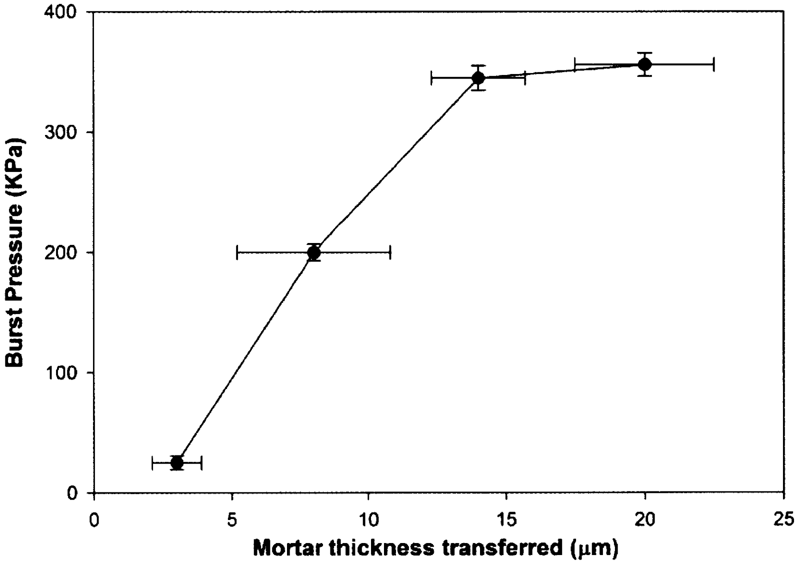

Fig. 3-3 Pressure at which the porous surface sandwiched device leaks as a function of the mortar thickness transferred.

3.2 In-situ functionalization of nanoporous membranes incorporated in microfluidic devices for specific biorecognition

Functionalization of porous surfaces such as carbon nonotube forests, monoliths and commercially available membranes for specific bio-particle recognition has been investigated widely in the past (see section 2.2). Due to the commercial availability and ease of integration of nanoporous membranes, we focus on the covalent and non-covalent functionalization strategies developed for nonoporous membranes. Our goal in this section was to select an effective on chip specific functionalization strategy that does not compromise the device integrity while blocking non-specific binding on nanoporous membranes.

The most common non-covalent functionalization strategy involves physical adsorption of the proteins onto the nanoporous surface through hydrophobic interactions. Surface coverage of proteins on the hydrophobic surfaces has been characterized using atomic force microscopy. Covalent attachment of proteins onto any surface, on the other hand, requires formation of functional groups, which is conjugated to the desired protein via a linker. Such covalent attachment is a function of a chemical bond between the surface and protein which prevents desorption from the surface even under shear from the fluid. Polycarbonate membranes can either be activated using ionic plasma [97, 98] or chemical methods. However, once integrated into the microfluidic device, ionic plasma does not effectively penetrate into the microfluidic channel to activate the porous polycarbonate surface. Additionally, if the polycarbonate membrane is plasma activated before integrating into the device, extreme caution is required to not contaminate the surface. Instead, chemical methods provide a comfortable and reliable way for in-situ activation and functionalization. Previously, amino-containing ligands have been bound to the activated carbonates on the hydroxyl groups of the polysaccharide support such as agar and dextran for affinity chromatography [99]. A similar approach for polycarbonate membranes is to couple poly-(L-lysine) to polycarbonate membrane on the activated carbonate groups of the polycarbonate membrane and activate the other amino groups of poly-(L-lysine) by addition of glutaraldehyde [100]. This is followed by incubation of the protein of interest which attaches to the the aine groups. Schematic of the different reactions during these steps are shown in Fig. 3-4a. Specifically, after integrating the membrane into the microfluidic device (see section 3.1), a 20 mg of poly-(L-lysine) was dissolved in 1.0 mL of 50 mM sodium carbonate solution was prepared and was flown into the microfluidic device at 5 μl/min and kept at 4°C for 24 h. The membrane was then thoroughly washed with distilled water. In order to immobilize protein, the polycarbonate membrane immobilized with poly-(L-lysine) was soaked in 50 mM phosphate buffer, pH 7.0, containing glutaraldehyde (1.0% v/v) for 2h at 4°C. Then the membrane was washed several times with distilled water and phosphate buffer. Avidin (50μg/mL) was then flown into the microfluidic chamber and was allowed to sit for 24 hr. In order to reduce the non-specific binding, Tween-20, an ampiphyllic molecule was added which covered the uncoated regions of the polycarbonate membranes. Hydrophobic interactions between tween and the polycarbonate lead to non-covalent coverage between the covalent linkages of polycarbonate membrane and the protein.

In order to measure the effectiveness of the covalent method of functionalization over the non-covalent adsorption, avidin protein surface functionalization was tested by using complementary fluorescent biotin for specific binding and using fluorescent bovine serum albumin for non specific binding. Fluorescence measurements across the channel width showed a two-fold increase in avidin functionalization using covalent lysine activation of the polycarbonate membrane compared to the adsorption (Fig. 3-4b). A 2.5 fold increase in the fluorescent biotin signal was seen for functionalization of the polycarbonate microporous surfaces for the lysine activation method over the regular physic-sorption (Fig. 3-4 b,c,d)

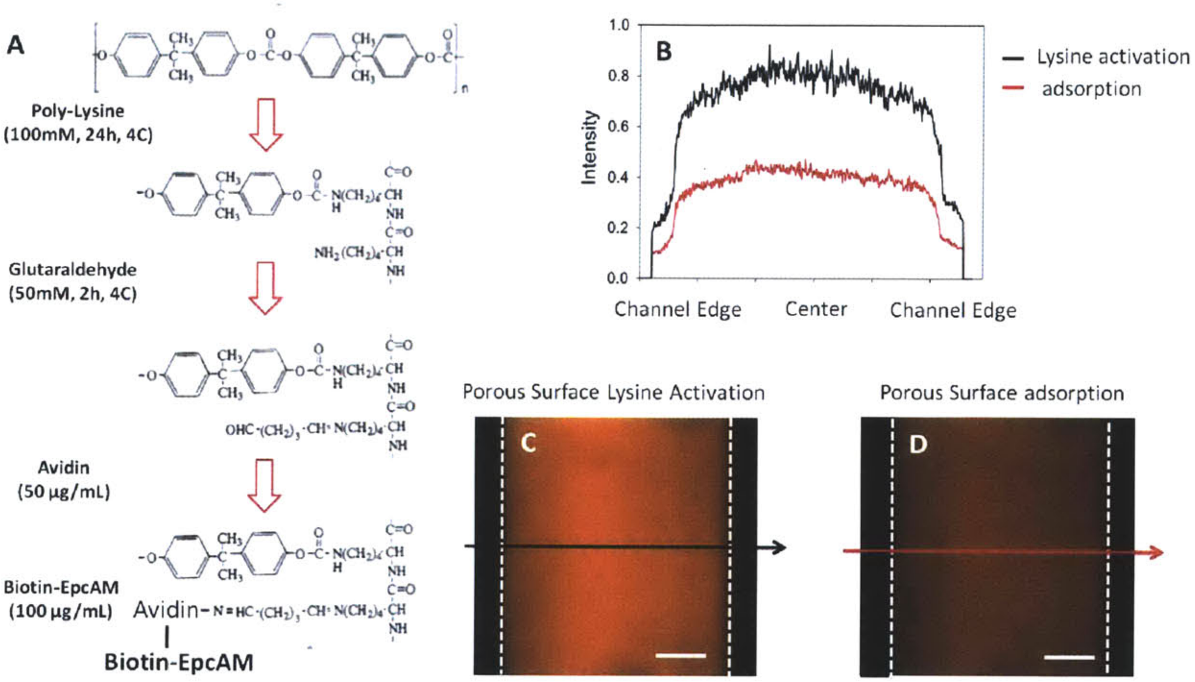

Fig. 3-4 (A) Poly-(L-lysine) functionalization protocol **(B)** Intensity measurement across the channel for Lysine activated avidin functionalization and adsorption based functionalization **(C)** representative image for the lysine activated channel **(D)** representative image for the adsorption channel

3.3 Lumped resistor model

The microfluidic device fabricated in section 3.2 can be represented as shown in Fig. 3-5. The figure shows the important independent and dependent parameters of consideration that define the system completely. The independent variables include the geometrical parameters of the top and bottom channel (L = length of the channel, w = width of the channel, h_1 = height of the top channel, h_2 = height of the bottom channel), the membrane (porosity as function of pore diameter (d_p) and pore frequency (f_p)) and the set pressure at the inlet (P_{set}) and the outlet (P_o). These independent variables are responsible for driving dependent variables such as the fluid flux through the top (Q_t) and the bottom channel (Q_b), which are of critical interest for the remainder of this work. As shown in Fig. 3-5, several independent variables dictate the fluid flux and changing either of these can change the fluid dynamics of the entire system, making it hard to predict the flux components. Instead, another way to describe the model would be to lump the geometrical components into their corresponding elemental resistances. The corresponding elemental resistances and the model are shown in Fig. 3-6a.

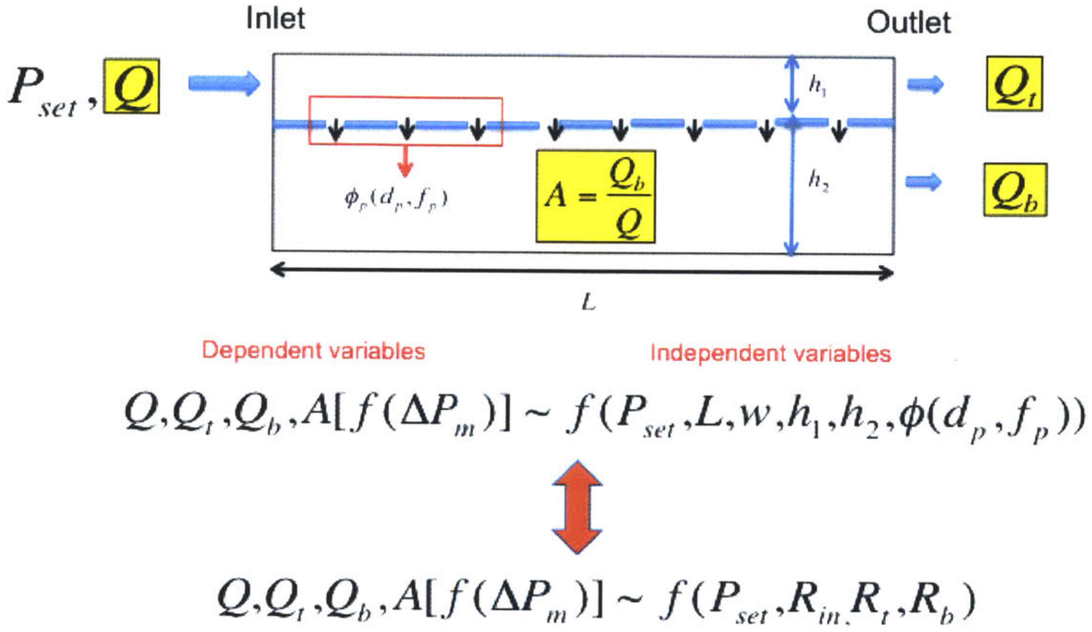

$$Q, Q_t, Q_b, A[f(\Delta P_m)] \sim f(P_{set}, L, w, h_1, h_2, \phi(d_p, f_p))$$

$$Q, Q_t, Q_b, A[f(\Delta P_m)] \sim f(P_{set}, R_{in}, R_t, R_b)$$

Fig. 3-5 Schematic showing the independent and dependent variables in the integrated nanoporous surface device

A consequence of the lumped resistance model is that the fluid flux through the top and the bottom outlets of the device remain same as long as the components resistances of the device match. This allows fabrication of equivalent devices with different dimensions and geometries. The lumped resistor model also allows us to overcome the variability in the commercial membrane porosities and membrane resistances. By adding large resistive tubings at the top and bottom outlets, we can "short" or remove the dependence on the variable commerical membrane resistance (Fig. 3-6b). Eqn. 3.8 describes the criterion under which this "shorting" condition would take place.

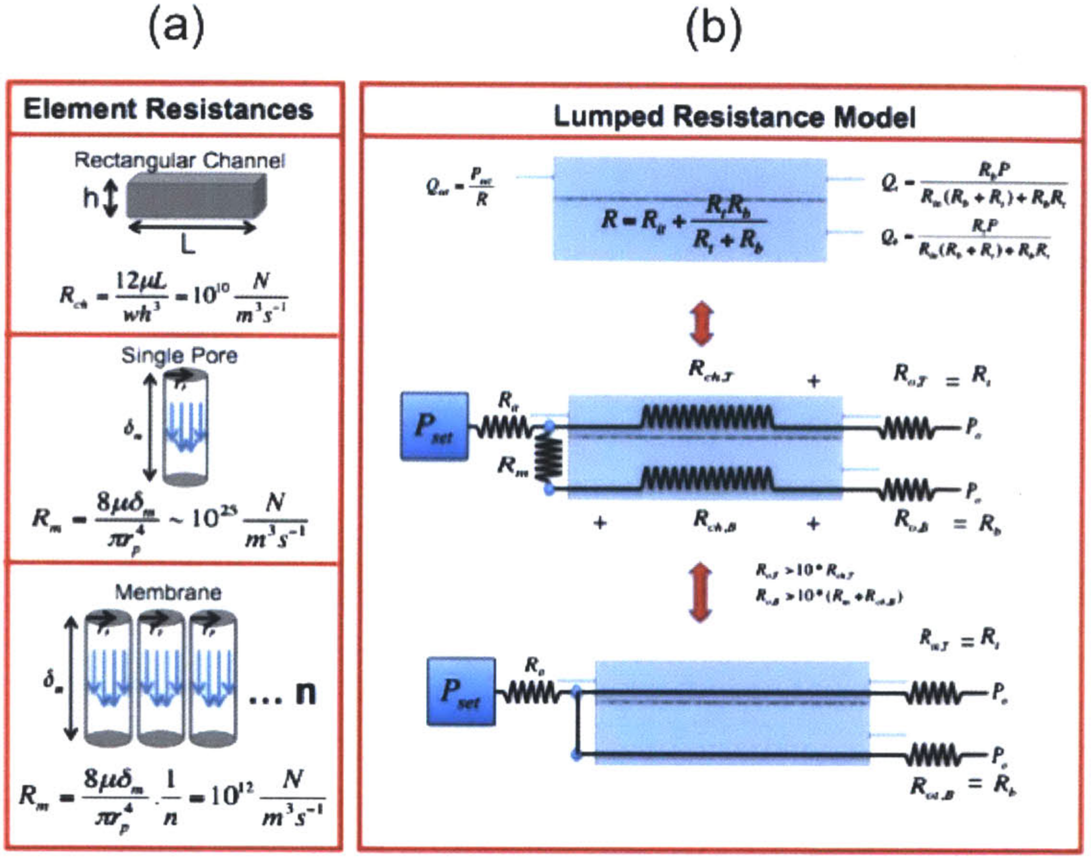

Fig. 3-6 Lumped resistance model **(a)** Element resistances **(b)** Lumped resistor model

Fig. 3-6b shows the lumped resister model for the sandwiched nanoporous membrane device. Using high resistive elements at the end ($R_{o,T}$ and $R_{o,B}$) percentage permeation flux (A) variations can be reduced. These output resistive elements can either be fabricated on the microfluidic chip as channels or can be externally added in the form of tubings. Large resistive tubings (tubing radius, r_t=50 μm) at the top and bottom channels helped "short" out any inherent variations in the commercially available membranes and insure constant permeation flux along the length of the membrane. The ratio of the resistances of the top and bottom tubings determine the fluid split, whereas the actual resistances of the tubings determine the sample flow rate through the top and bottom outlets of the channels. The different component fluidic resistances of the device are shown in Table 3.1. The channel resistances (R_{ch}) were calculated using Eqn. 3.1

$$R_{ch} = \frac{12\mu L_{ch}}{wh^3} \tag{3.1}$$

The tubing resistances (R_{tubing}) were calculated using Eqn. 3.2

$$R_{tubing} = \frac{8\mu L_t}{\pi r_t^4} \tag{3.2}$$

The membrane resistances (R_m) were calculated using Eqn. 3.3

$$R_m = \frac{8\mu L_p}{\pi r_p^4} \cdot \frac{1}{n} \tag{3.3}$$

Based on the above resistances, the theoretical flow rates in the top channel (Q_t) and through the membrane and out of the bottom outlet (Q_b) are given by

$$Q_t = \frac{R_b P}{(R_{in}(R_b + R_t) + R_b R_t)} \tag{3.4}$$

$$Q_b = \frac{R_b P}{(R_{in}(R_b + R_t) + R_b R_t)} \tag{3.5}$$

Where,

The resistance of the top arm of the device is given by

$$R_t = R_{ch,T} + R_{o,T} \tag{3.6}$$

and, the resistance of the bottom arm is given by

$$R_b = R_m + R_{ch,B} + R_{o,B} \tag{3.7}$$

If,

$$\begin{aligned} R_{o,T} &> 10 * R_{ch,T} \\ R_{o,B} &> 10 * (R_m + R_{ch,B}) \end{aligned} \tag{3.8}$$

Then, the resistance in the top arm (R_t) is dictated solely by the external top outlet resistance ($R_{o,T}$)

$$R_t = R_{o,T} \tag{3.9}$$

and the resistance in the bottom arm (R_b) is dictated by the external bottom outlet resistance ($R_{o,B}$)

$$R_b = R_{o,B} \tag{3.10}$$

Combining 3.4,3.5,3.9 and 3.10, we find that the fractional permeation flux through the membrane (A) is given by 3.11 and is also dependent on externally controllable resistances.

$$A = \frac{Q_b}{Q_t + Q_b} = \frac{R_t}{R_t + R_b} \tag{3.11}$$

The resistance values in Table 3.1 show that the output tubings have resistance much greater (~10 times) than the fluidic resistance of the channel or the membrane. Under this condition, the resistance model can be simplified as shown in Fig. 3-6b. The effect of the simplified model is to maintain a constant pressure difference along the length of the membrane. Since pressure difference drives fluid flow, a constant uniform velocity of fluid flux at the wall is expected. In contrast the previous models described have a diminishing wall velocity do to a decrease in pressure towards the end of the channel.

From Eqn. 3.11 we see that addition of high resistances at the end of the channel leads to the dependence of the fraction permeation flux, A, completely on the lengths of the resistive elements at the outlets. Additionally, the simplified model allows prediction of the fluid split and flow rates based on the lengths and therefore the resistances of the outlet tubings. Eqn. 3.6-3.11, define sample fluid flow rate through the top channel and the membrane depends on the absolute values of the top and bottom output tubing resistances, but the split depends on the ratios of the two.

	Inlet tubing (Length= 50 cm)	Top Channel	Top Outlet tubing (Length = 266 cm)	Bottom Channel	Bottom outlet tubing (Length = 114 cm)	Membrane (Average porosity ~ 10%, r_p = 100 nm)
Fluidic Resistance	$4.9\text{x}10^{12}$	$1.24\text{x}10^{11}$	$2.6\ \text{x}10^{13}$	$1.5\text{x}10^{10}$	$1.1\text{x}10^{13}$	10^{12}

Table 3-1 Component resistances of the device. The tubing resistances are kept at a much higher resistance that the channel and the membrane resistances.

3.5 Fluid flux measurements

In order to measure the fluid flux through the top channel and the bottom channel, we used a constant pressure source and control the outlet resistances ($R_{o,T}$ and $R_{o,B}$) by externally changing the lengths of the tubing's. The resistances of the tubing's were calculated using Eqn. 3.2. The fluid was collected into eppendorf tubes out of the top and bottom inlets at each pressure value and the collected volumes were measured. These experimentally measured volumes were compared against the theoretical values using Eqn. 3.4, Eqn. 3.5, Eqn. 3.9 and Eqn. 3.10 of the lumped resistor model (See section 3.4). We find that there is precise agreement between the theoretical and experimental results as the flow rates through top and bottom channels scale linearly with applied pressure difference (Fig. 3-7a). Moreover, the ratio of flow rates in the top and bottom channels is constant, governed by the high resistance outputs. The model was able to accurately predict the fluid split between the top and the bottom channels as a function of the sample input pressure when the tubing resistances were approximately ten times the fluidic resistance of the membrane and the channels in a sample with dilute suspension of particles ($\phi_o <$ 0.1). In the event when the outlet tubings are short in length and the criterion of Eqn. 3.8 is not met, the flux through the top and the bottom channels varies greatly. A mean standard deviation of 0.42 ml/hr permeation flux through the membranes was measured due to porosity differences in the polycarbonate membranes (Fig. 3-7b).

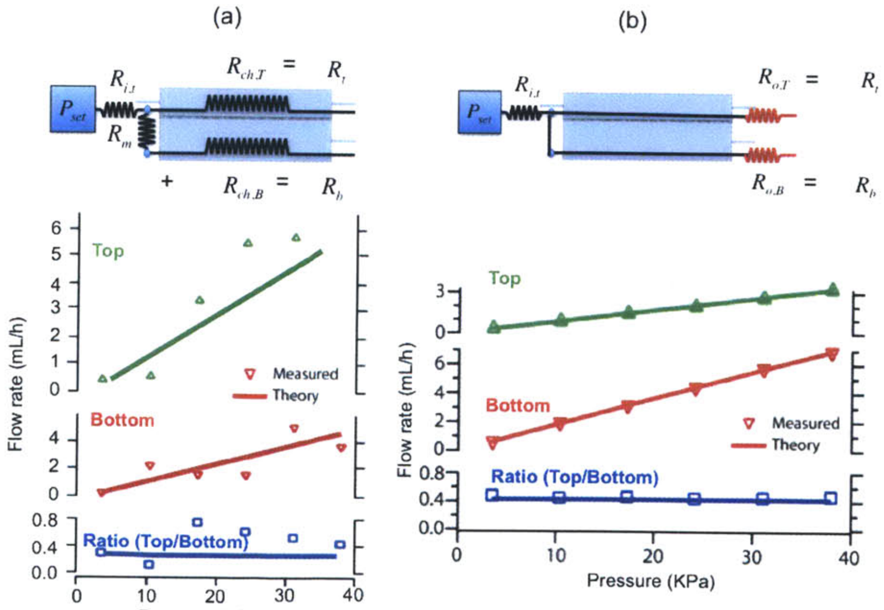

Fluid flux measurements without external resistors

Fluid flux measurements with external resistors

Fig. 3-7 (a) Experimental and theoretical flow rates through the top and bottom outlets of the device and the ratio of the top flow rate to bottom flow rate as a function of pressure with no external resistances **(b)** Experimental and theoretical flow rates through the top and bottom outlets of the device and the ratio of the top flow rate to bottom flow rate as a function of pressure with external resistances

3.6 Summary

In this chapter, we described and optimized the integration and characterization methodology used for incorporating commercially available nano-porous surfaces into the micro-fluidic devices. Additionally, using fluorescence as the read out we showed that covalent functionalization of proteins on polycarbonate surface is more effective compared to physic-sorption. Further, in the section we develop lumped resistor model which helped us reproducibly control the fluid flux through the top and bottom channels by appropriate selection of large resistances at the outlet. This model remains the mainstay for the rest of the thesis as it is critical to precisely control the fluid fluxes through the top and bottom channels. Finally, we demonstrated agreement between the expected permeation flux and flow rates through the porous surface using the lumped resistor model and the experimental results

Chapter 4

Antibody-Functionalized Fluid-Permeable Nano-Porous Surfaces for Rolling Cell Capture at High Flow Rates

Introduction

In this chapter we describe the use of fluid permeable nano-porous membranous surface microfluidic device towards capturing specific target cells (PC3, PC3-9 and H1650) at high flow rates. In section 4.1 we describe cell sample preparation, device operation and cell quantitation methods used in every experiment. Section 4.2 elucidates the role of fluid permeable surfaces to enhance mass transport from the lumen of the microfluidic device to the antibody covered reactive porous surface. In this section we model fluid and cell streamlines and compare the results quantitatively to the cell trajectories observed in a solid surface and a porous surface microfluidic device. Additionally, using fluoresce microscopy we measure the fraction of the total cells that convect to porous surface as a function of the permeation flux (A). Once the cells are on the surface, we study the rolling motion of cells in section 4.3. Section 4.4 explores the effect on the cell surface average velocity along the channel length and compares it with the hydrodynamic model developed for the solid surface in section 4.5. In section 4.6, we look at the cell motion in more detail by evaluating the motion of individual cells on the porous surface as a function of time. Studies in section 4.4 and 4.6 are used as inputs to model the probability of cell capture at a function of cell surface velocity in section 4.7. Section 4.8 describes the amount of force associated with breaking a single EpCAM antigen/anti-EpCAM bond and extrapolation into dislodging non-specific cells, while retaining specific cells. In section 4.9 we look at the cell capture efficiency of low expressing prostate cancer (PC3-9 cells), and high expressing prostate cancer (PC3) and lung cancer (H1650) cell lines as a function of flow rate on a porous and solid surfaces, covered with specific anti-EpCAM antibodies and non-specific IgG antibodies. We summarize the findings in section 4.10.

4.1 Methods

In this section we describe the methods used for cell sample preparation, device operation and target cell enumeration. These methods are followed for all the experiments performed in chapter 4 and chapter 5.

4.1.1 Cell sample preparation

Leukocytes ("buffy coat") used in the experiments in chapters 4 and 5 were isolated from whole blood using deterministic lateral displacement [101] and resuspended to the relevant concentration. The sample concentration (C_{cells}) of 500,000 cells/mL corresponded to a volume particle fraction (ϕ_o~0.01). Subsequently, C_{cells}~1.5x106 cells/mL correspond to ϕ_o~0.03 and C_{cells}~2.5x106 cells/mL correspond to ϕ_o~0.05. These cells were fluorescently labeled (Cell Tracker Calcein green, Invitrogen, Carlsbad, CA) following the manufacturer protocol. PC3 human prostate cancer cells (ATCC), PC3-9 and H1650 cancer cells lines used were cultured at 37°C and 5% CO2 in F-12K growth media containing 1.5 mM L-glutamine supplemented with 10% FBS and 1% Penicillin/Streptomycin, with media changes every 2–3 days. These cells were labeled with a different fluorescent dye (Cell Tracker Orange, Invitrogen, Carlsbad, CA) and spiked into the sample at a ratio of 1:250 (2000/mL). The PC3, PC3-9 and H1650 cell spike count was verified immediately before addition to the buffy coat population as well as before loading the sample into the device. These readings were consistent within 5%.

4.1.2 Device Operation

As mentioned in section 2.4, immuno-chromatography based cell separation have two steps. First step is the capture phase, in which the sample is flown through the device as a desired flow rate that allows specific cell capture. In the second step or the wash phase, buffer solution is flown through the device to remove non-specifically bound cells to surface. During the wash phase, shear force differential between the specific cells and non specific cells be optimized such that only the non-specific cells get pulled off from the surface during the wash step.

In case of nano-porous surface integrated device the capture phase requires injection of the sample through the top inlet, keeping the top outlet and bottom outlet open (Fig. 4-1a1). In this configuration the streamlines get biased towards the nano-porous surface due to fluid permeation through it. As the size of the pores is in the nanometer range (radius = 100 nm) cells in the input sample do not pass through the pores but follow the streamline and come in contact with the reactive surface. One at the surface, the shear in the microfluidic device leads to cell rolling and allows interaction between the complentary receptor-ligand (fig. 4-1a2). The forces that dictate this configuration are described in more detail in section's 4.4 and 4.5. During the wash step, the bottom outlet is closed by clamping the tubing and the top outlet is kept open and buffer is injected into the microfluidic device. In this configuration, no fluid permeates through the nano-porous membrane and the device has similar fluid dynamics to a regular solid surface channel (Fig. 4-1b).

Experimentally, samples were loaded into a 60 mL syringe and a constant pressure syringe pump was used to apply a constant flow through the top inlet, while the bottom inlet was closed. The top and bottom outlets were both open, and the ratio of transverse membrane flux and axial channel flux was regulated using relative resistances of the outlet tubing (see section 3.3). After the sample had been processed, the bottom outlet was closed and PBS was flowed through the top channel to remove nonspecifically bound cells.

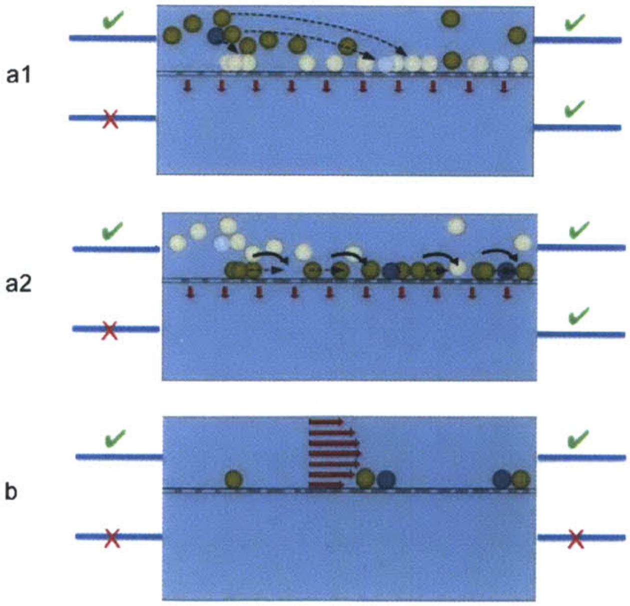

Fig. 4-1 (a1) Cell capture mode with the top outlet and the bottom outlet open. In this stage the cells get convected to the surface **(a2)** The top and the bottom outlet remain open, however, this phase focuses on the translational motion of cells along the cell surface. **(b)** The top outlet remains open, but the bottom outlet is closed and buffer is flow throw the top to wash the non specific cells.

4.1.3 Imaging and quantitation of specific cell capture

Cell capture was visualized using an upright epifluorescence microscope (Nikon Eclipse 90i) using a 4X (Nikon Plan Fluor, NA=0.13) or 10X objective (Nikon CFI Plan Apo, NA=0.45) at 10 frames per second with a CCD camera (QImaging Retiga 2000R). Overall cell capture in the device (N_c) and waste collection (N_{out}) were enumerated using three different emission spectra to identify cells (DAPI) as well as distinguish spiked PC3 cells (CTO) and background leukocytes (FITC). The capture efficiency was calculated as the captured cells divided by the total cells flowed through the device, i.e. $N_c/(N_c+N_{out})$ averaged over three experiments. Mass balance on the number of PC3 cells spiked into the cells was performed by counting the number of cells injected into the device, the number of cells captured on the porous membrane and the PC3 cells that exited the device into the collection well. There was a ~4% difference between the intended number of cells injected into the device and the number of cells that was accounted for using mass balance.

4.2 Cell Transport to Surface is Enhanced by Diverting Streamlines

As discussed previously, the effectiveness of conventional adhesion-based assays is strongly diminished at high flow rates since most cells do not reach the surface. To overcome this limitation and enhance cell-surface interaction, in this thesis we develop a two-chamber microfluidic device was developed, with a porous capture surface sandwiched in between (Fig. 3-1). These surfaces consisted of commercially available polycarbonate membranes with an overall porosity of 10% and average pore diameter of ~200 nm, which allow fluid permeation but are small enough to prevent the ~10 μm cells from entering or becoming trapped. This device geometry allows a controlled fraction of the incoming fluid flow to be diverted into the porous membrane, while the remainder continues to the outlet. These fluid flow conditions were calibrated and in good agreement with the expected values based on the applied pressure difference (Fig. 3-7b).

4.2.1 Fluid streamlines in a porous surface device

The limiting case of no fluid flux through the membrane is essentially equivalent to flow past a solid surface, since all the fluid flux is exiting through the top outlet. The cell trajectories in this scenario are well described by pressure-driven Poiseulle flow in the axial direction, as well as a constant sedimentation velocity due to the density difference of the cells [102]. The non-dimensionalized axial and transverse fluid velocity field components U_x, U_y as a function of (non-dimensionalized) coordinate system ($X = x/h$, $Y = y/h$), are given by:

$$U_x (X, Y)= 6 (Y - Y^2); \quad U_y (X, Y)= 0 \tag{4.1}$$

In order to derive, fluid streamlines from the existing velocity fields for a solid channel, we use non-dimensionalized coordinates for coordinates x,y; pressure p, velocity u_x and ratio of permeation flux to total flux A

$$X=\frac{x}{h}, Y=\frac{y}{h}, <P>=\frac{<p>-p_o}{p_o}, <U_x>=\frac{<u_x>}{<u_o>}, A=\frac{v_w}{<u_o>} \tag{4.2}$$

Further, since the channel has a small height compared to its length and Reynolds number is low (Re << 1), lubrication approximation holds

$$\frac{\partial^2 u_x}{\partial Y^2}=\frac{h}{\mu}\frac{dP}{dX}, \qquad \text{BC's: } u_X(X,0)=u_X(X,1)=0 \tag{4.3}$$

Considering an elemental section in a microfluidic device with a porous bottom surface, the fluid balance is given by relating the average fluid velocity along the length of the channel to the fluid permeating through the membrane,

$$\frac{d<u_X>}{dX}=-\frac{v_w}{h} \tag{4.4}$$

Integrating along the length of the channel,

$$<u_X>=u_o(1-v_w X) \tag{4.5}$$

Therefore,

$$u_X(X,Y)=6u_o(1-v_w X)(Y-Y^2) \tag{4.6}$$

In its non-dimensional form,

$$U_X(X,Y) = 6(1 - AX)(Y - Y^2) \tag{4.7}$$

The transverse fluid velocity field $u_Y(X,Y)$, can be obtained from the continuity equation

$$\frac{\partial u_X}{\partial X} + \frac{\partial u_Y}{\partial Y} = 0 \tag{4.8}$$

Integrating Eqn. 4.18,

$$u_Y(X,Y) = \int_Y^1 \frac{\partial u_X}{\partial X}(X,S)dS, \qquad \text{BC: } u_Y(X,1) = 0 \tag{4.9}$$

$$u_Y(X,Y) = -v_w(2Y^3 - 3Y^2) \tag{4.10}$$

Where v_w is the superficial wall velocity at the porous surface,

$$v_w = \frac{Q}{A_{mem}} = \frac{\Delta P}{A_m(R_m + R_{o,b})} = \frac{\Delta P}{(w * L)(R_m + R_{o,b})} \tag{4.11}$$

In non-dimensionalized form,

$$U_Y(X,Y) = -A(2Y^3 - 3Y^2) \tag{4.12}$$

The y-component of the fluid field is responsible for rapid advection of cells traveling along streamlines to the capture surface. Therefore, for the fractional permeation flux through the membrane A, the non-dimensionalized velocity field components are given by:

$$U_x\,(X,Y) = 6(1 - AX)(Y - Y^2);\; U_y\,(X,Y) = -A(2Y^3 - 3Y^2) \tag{4.13}$$

The corresponding fluid streamlines in the rectangular channel with a porous bottom is therefore given by,

$$3Y^2 - 2Y^3 = \frac{3Y_o^2 - 2Y_o^3}{1 + AX} \tag{4.14}$$

Since the no permeation case is similar to a solid surface case and is a limiting case of the permeation fluid fields derived in Eqn. 4.13, we should be able to retrieve results for the solid surface fluid fields by inserting $v_w \sim 0$ in Eqn. 4.13.

4.2.2 Cell trajectories in a dilute suspension

Even in a solid surface microfluidic device, the constant cell sedimentation perturbs the cell trajectories slightly from the fluid streamlines due to the density difference between the cell and the surrounding mediaThe corresponding cell velocities in the x- and the y- directions are given by

$$U_x(X, Y) = 6\,(Y - Y^2); \quad U_y(X, Y) = -B \tag{4.15}$$

where $B = 2R_c^2 g\Delta\rho/9\mu_0 \sim 2$ μm/s, is a constant sedimentation velocity for a particle of radius $R_c = 5$ μm and density difference $\Delta\rho \sim 0.030$ g/cm^3 (with respect to the solution).

To calculate the cell velocities in the porous surface device we use Faxen's law, which provides a general relationship between force on a spherical cell (F), its velocity (u_p) and the unperturbed fluid velocity (u_o) field far from the particle center. To determine how the cell trajectory is affected by the fluid streamlines, the x- and y- component of Faxen's first law for a non-buoyant cell (density difference $\Delta\rho$=0.030 g/cm^3) were calculated:

$$F_{ext,x} \sim F_x \sim 0 = 6\pi\mu R_c\{(u)_x - (u_p)_x + \frac{R_c^2}{6}(\nabla^2(u)_x)\} \tag{4.16}$$

$$F_{ext,y} \sim F_y \sim \frac{4\pi R_c^3\Delta\rho}{3} = 6\pi\mu R_c\{(u)_y - (u_p)_y + \frac{R_c^2}{6}(\nabla^2(u)_y)\} \tag{4.17}$$

where R_c = radius of the cell (5 μm). The effect of cell radius on streamline trajectory is negligible for R_c< 20μm. Therefore higher order R_c terms in Eqn. 4-15 and Eqn. 4.16 can be neglected and the Faxen's first law can be re-written as:

$$F_x \sim 0 = 6\pi\mu R_c\{(u)_x - (u_p)_x\} \tag{4.18}$$

$$F_y \sim \frac{4\pi R_c^3\Delta\rho}{3} = 6\pi\mu R_c\{(u)_y - (u_p)_y\} \tag{4.19}$$

The particle trajectory is thus given by,

$$\frac{dy}{dx} = \frac{v_w(3Y^2 - 2Y^3) - B}{6 < u_o > (1 - v_w X)(Y - Y^2)} \tag{4.20}$$

The cell trajectory in the solid surface microfluidic channel can be obtained by setting $v_w \sim 0$ in Eqn. 4.20

A representative case is shown in Fig. 4-2a for a cell sedimentation velocity of 2 μm/s and an average flow velocity of $<U_x>$ = 10,000 μm/s, corresponding to a flow rate Q_{in} = 6 mL/hr and cell radius R_c = 5 μm. At these high flow rates, cells are advected through the device so rapidly that they have very little time to sediment. Based on the calculated cell trajectories for these conditions, only those cells that are initially near the bottom of the channel (y < 10 μm) can reach the capture surface. Assuming that cells are uniformly distributed at the 100 μm high entrance, this corresponds to ~10% of cells reaching the surface, while the remaining ~90% have no opportunity to interact with the surface and get captured. These calculations are consistent with experimental measurements of the cell trajectories under these flow conditions using fluorescence microscopy, which show cells moving rapidly with constant axial velocity throughout the 3,000 μm field of view (Fig. 4-2c).

As the fluid permeation flux through the membrane is increased, more and more of the streamlines are diverted from the top outlet to the porous membrane (Fig. 4-2b). The calculated cell trajectories for this scenario are illustrated for a representative case of 70% permeation flux through the membrane, but the same flow rate as the previous example (Q_{in} = 6 mL/hr). In this case, the calculated cell trajectories do not deviate significantly from the streamlines (<1%), since advection (~10,000 μm/s) dominates over sedimentation (~2 μm/s) and hydrodynamic effects. These calculations are corroborated by experimental measurements of the cell trajectories (Fig.4-2d), showing that the axial velocity U_x rapidly decreases from an initial value of 2000 μm/s at x = 2.4 cm to ~200 um/s at x = 2.7 cm as the cell is transported to the surface and the transverse velocity U_y becomes more significant. Due to the device geometry and the rapid axial velocity of the cell, it is difficult to directly measure the height of the cell during its trajectory. However, a qualitative comparison of the calculated cell trajectories (Fig. 4-2b) with the experimentally measured cell axial velocities (Fig. 4-2d) suggest that these cells entered the device at a height roughly halfway between the bottom and top. Based on the calculated streamlines, all cells that enter the channel within 70 μm of the bottom surface should be captured (~70%), whereas the remaining 30% of cells exit the device at the top outlet.

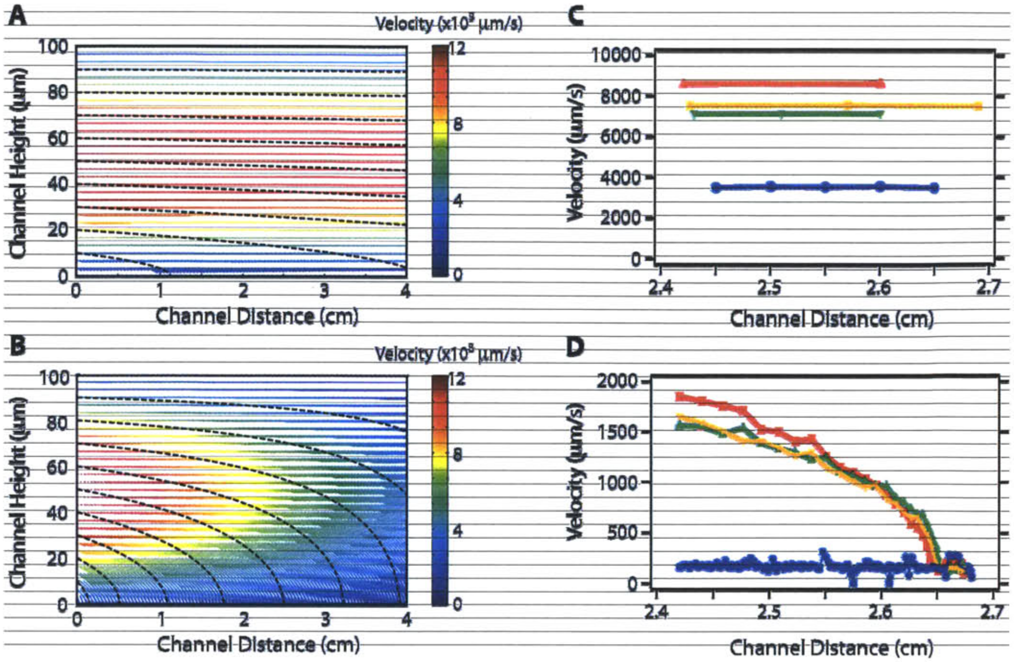

Fig. 4-2 Theoretical particle trajectories (dashed black lines) and fluid velocity field vectors (color) in channels with **(A)** solid surface (A = 0%) **(B)** fluid-permeable surface (A = 70%). Color bar corresponds to the magnitude of fluid velocity vectors. Experimentally measured particle velocities tracked in channels with **(C)** solid surface (A = 0%) and **(D)** fluid-permeable surface (A = 70%).

Streamline analysis predicts that if cells are uniformly distributed at the channel entrance the percentage cells convected to the porous surface from the bulk at high flow rates should be the same as the percentage of fluid permeating the porous surface. This was corroborated experimentally by visualizing fluorescently labeled cells under a microscope. The microscope was focused at the porous surface at the end of the channel and videos for each permeation flux condition were recorded. Cells "rolling" on the surface were focused and had round morphology, compared to the cells in the bulk which appeared as streaks. The length of the streak was a function of the velocity of the cell in the channel and the exposure time through the fluorescence shutter. Enumeration of the cells showed that the total fraction of cells transported to the porous capture surface scales linearly with the percentage of the fluid flux into the membrane (Fig. 4-3).

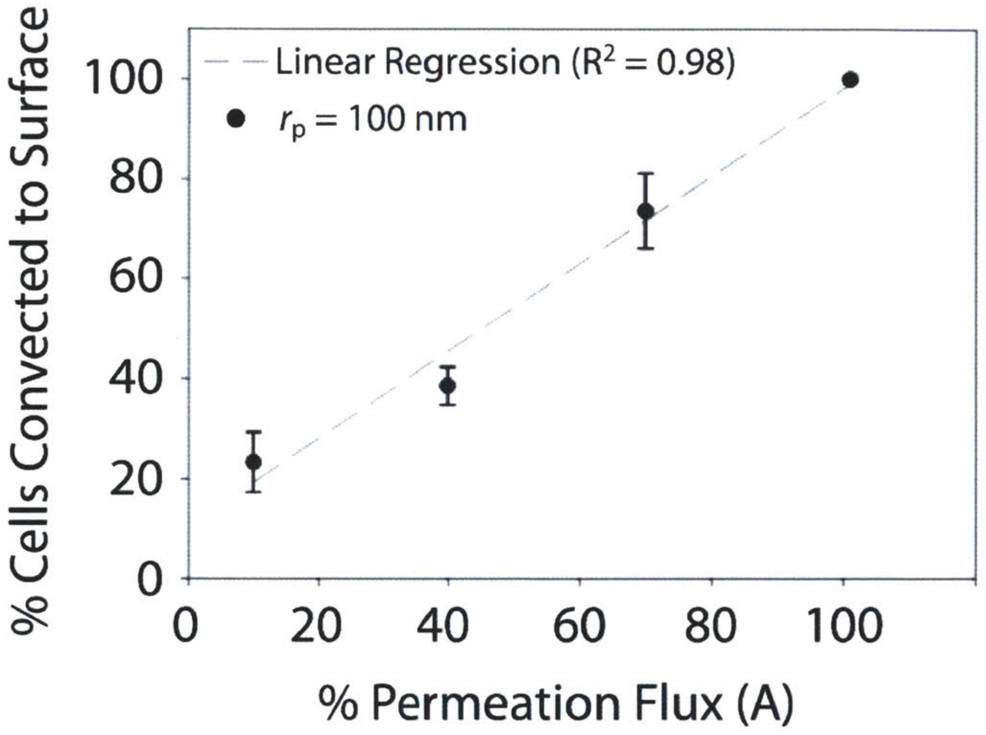

Fig. 4-3 Percentage cells convected to a porous capture surface scales linearly with the percentage permeation flux. Each data point corresponds to measurements on 5 independent devices, with pore size r_p=100 nm.

4.3 Cell convected to the porous surface portray a rolling motion

In order to discern the motion of cells convected to the surface, we used asymmetrically fluorescent Janus particles and viewed the particles under high magnification (40X). The Janus particles were partially sputtered with gold which blocked the fluorescence from the particle. Under the microscope we were able to see the sequential change in fluorescence position as the particles moved along the length of the channel indicating rolling motion.

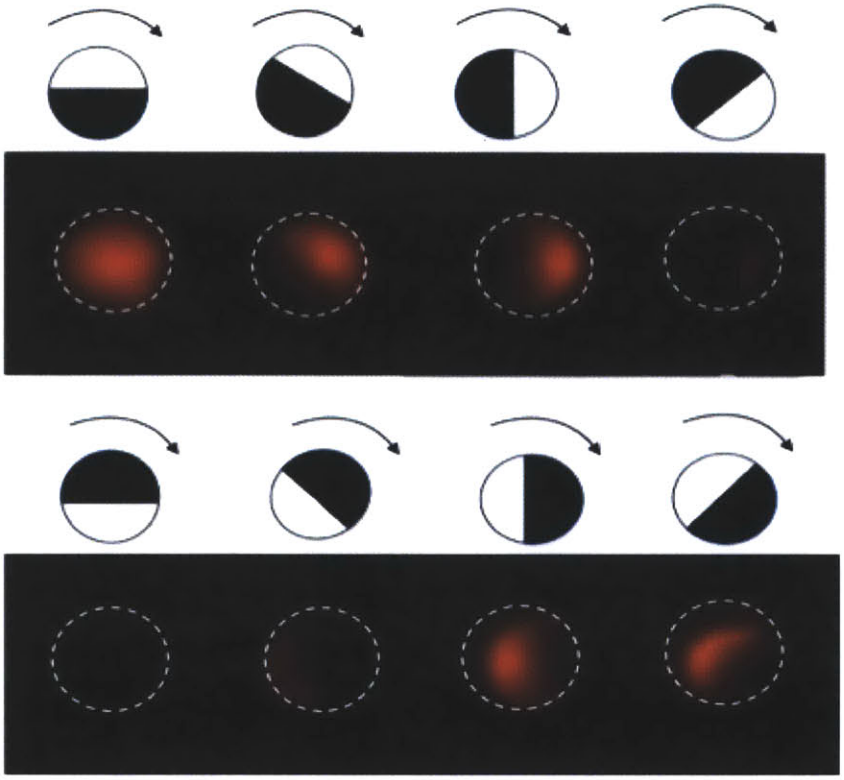

Fig. 4.4 Sequential images of gold coated Janus particles indicating rolling motion on the surface.

4.4 Nano-porous fluid permeable surfaces decrease surface rolling velocity

An important implication of the streamline calculation is that when permeation occurs, the axial fluid velocity U_x decreases linearly along the length of the device. At each position, x, along the length of the channel, a certain fraction of fluid permeated through the surface. As a result, the shear rate near the surface is also expected to decrease with increasing distance x, reaching a minimum at the end of the porous surface. Since the shear in the bulk is responsible for translation motion of the cell along the porous surface, we expected a decrease in the cell surface velocity. To verify this trend, the cell surface velocity $u_c(x)$ was experimentally measured at three locations (beginning, middle and end) along the length of the device for various values of A at a constant flow rate (Q_{in} = 6 mL/hr) and fit using linear regression (Fig. 4-5). The cell velocity decrease over the length of the channel is linear. This is owed to the presence of large external resistances at the channel outlets that maintain a constant permeation flux throughout the length of the channel. As a result the decrease in the shear and hence the velocity per unit length is constant. To understand the effect of the magnitude of fluid permeable nano-porous surface on cell velocity, these measurements were compared to the limiting case of cell motion along a solid surface at the same bulk shear using the hydrodynamic model proposed by Goldman *et al.* for a particle moving near a solid surface due to a shear field [103]. Experimentally using the following scaling for cell surface velocity:

$$u_c(x) \sim u_{c,0}(1 - Ax / L) \tag{4-21}$$

where $u_{c,0}$ is the cell surface velocity at the entrance and L is the channel length. The measured velocities and Goldman model show good agreement for $A = 50\%$ (Fig. 4-5). However, at larger permeation fluxes, the experimental cell surface velocities are consistently slower than the expected values by several hundred microns per second.

4.5 Comparison of measured cell surface velocity on the porous surface with hydrodynamic Model

The hydrodynamics of a particle moving near a solid surface due to a shear field were previously treated theoretically by Goldman et al. [104]. Based on the total flow rate of 6 mL/h in a channel with dimensions with L=4cm, w=2mm and h=100 μm through the channels, there should be a shear stress of 5 dyn/cm^2 at the entrance. Assuming a particle-surface separation of 50 nm [105], the initial cell surface velocity is expected to be $u_{c,0} = 1000$ μm/s. This value is incorporated into a phenomenological equation based on Eqn. 4-20: $u_c(x) \sim u_{c,0}(1 - Ax / L)$. As shown in Fig. 4-4, the measured velocities are consistent with the hydrodynamic model at A = 50%. However, the measured values are significantly slower than those predicted from the model and increasingly deviate at higher permeation rates. This discrepancy arises from the porosity of the surface, which is not accounted for in the Goldman model. The slowdown accounts from an additional "suction" force that causes temporary pauses in cell motion. This suggests that the cell surface velocity is not solely dictated by the local shear field, but may have additional inhibitory interactions with a porous surface that do not occur on a solid surface. These cell-surface interactions pauses are examined in more detail in the subsequent section.

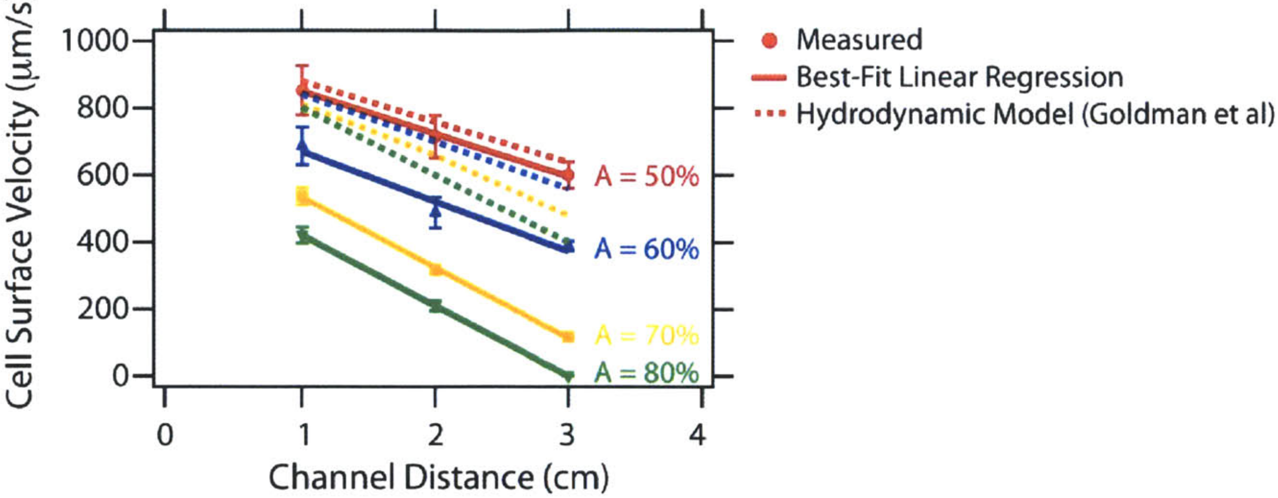

Fig. 4-5 Comparison of measured cell surface velocity (markers), best-fit linear regression (solid lines) and hydrodynamic model of Goldman et al (dotted lines). Measured values are in agreement with model for A = 50%, but are consistently slower at larger permeation.

4.6 Cell-surface interactions are promoted by a fluid permeable surface

In the previous sections we have quantified cell convection to the reactive porous surface and the characteristics of cell rolling on it. The effectiveness of cell capture assays also depends on the arrest of cell motion on the surface, which occurs through the competition of specific biomolecular bond formation and local shearing forces. A mathematical model built elucidates this in more detail in section 4.7 and section 4.8. Near a surface, cells have been previously observed to "roll" at constant velocity due to hydrodynamic interactions, which is essential for selective capture both *in vitro* and *in vivo*. Representative individual cell trajectories were examined near a porous surface functionalized with non-complementary IgG antibodies (Fig. 4-6a). Up until time $t = 1$ s, the measured axial velocity U_x rapidly decreases as the cell approaches the surface, after which it maintains a reduced, constant velocity (Fig. 4-6b). Since the IgG antibodies cannot form strong specific biomolecular bonds with the cellular receptors, motion is never completely arrested on the surface. However, the velocity shows surprising fluctuations where the cell appears to temporarily "pause" its motion on the surface (Fig. 4-6a, inset). The magnitude of this fluctuation ($\Delta u_c \sim 350$ μm/s) is considerably larger than the standard deviation of the velocity before and after this event ($\sigma_u \sim 40$ μm/s). These fluctuations may occur because of local differences in surface porosity, which apply slightly stronger suction forces to the cell to slow down its motion. This mechanism is clearly insufficient to permanently capture cells, but it is likely to influence the binding kinetics in a way that cannot occur on a solid surface.

These velocity fluctuations increase in frequency and duration on porous surfaces that have been functionalized with anti-EpCAM antibodies ($\sigma_u \sim 130$ μm/s) (Fig. 4-6c), which are complimentary to cancer cells of epithelial origin but not leukocytes [106]. In these representative trajectories, cells again reach the porous surface around time $t = 1$ s and show a similar decrease in axial velocity, indicating they are being advected to the surface. However, rather than continuing at a constant diminished velocity (Fig. 4-6b), these cells continue to decelerate and are completely arrested within a few seconds (Fig. 4-6d). The permeation flux through a porous surface thus appears to promote the kinetics of strong, specific biomolecular bond formation by slowing down cell rolling across the surface. As evidenced by the previous example with non-complimentary anti-IgG, this mechanism is not strong enough to irreversibly stabilize cell motion against the local shear field. However, in the presence of complimentary anti-EpCAM, this enhanced cell-surface interaction allows specific cell capture to continue to occur even at fast total flow rates. Essentially, these conditions of highly reduced shear and an additional "braking" suction mechanism near a permeable surface lead to conditions comparable to those at a solid surface at dramatically lower flow rates and shear.

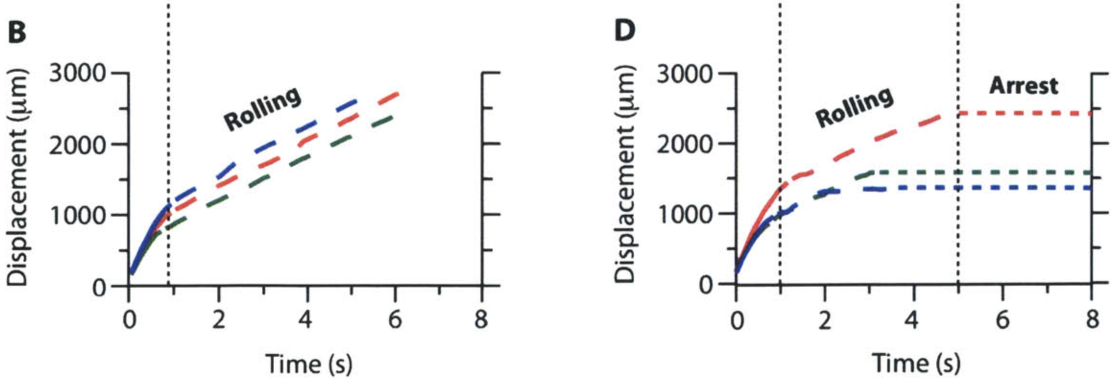

Fig. 4-6 Instantaneous velocity and displacement trajectories for PC3 cancer cells transported to **(A, B)** non-complimentary anti-IgG, exhibiting rolling motion at constant speed and **(C, D)** anti-EpCAM fluid-permeable surfaces at $x = 3$ cm with $A = 70\%$, exhibiting rolling prior to complete arrest.

4.7 Model describing arrest of specific cells based on relative velocity

In the previous section we quantitatively decribed the motion of cells on a porous surface subjected to tangential shear as well as normal suction forces. It was also observed that compared to a solid surface the cell surface velocity on a nano-porous permeable surface is much lower and demonstrates a characteristic stop and go motion under tangential and normal fluidic forces. Fig. 4-7a shows multiple individual cell velocities as a function of time for the specific case of A = 70% and $\tau = 5$ dyn/cm^2. The variation in the stoppage times, Δt_s for the same combination of shear and permeation flux arose due to variation in the local porosities of the commercial membranes. The quantification of the stoppage times of multiple cells as a function of permeation flux is shown in Fig. 4-7b. It was seen that the stoppage time increases with permeation flux. However since it was desirable to have intermittent stops on the unfunctionalized surface and not a complete stop, we chose a combination of shear = 5 dyn/cm^2 and A = 70%.

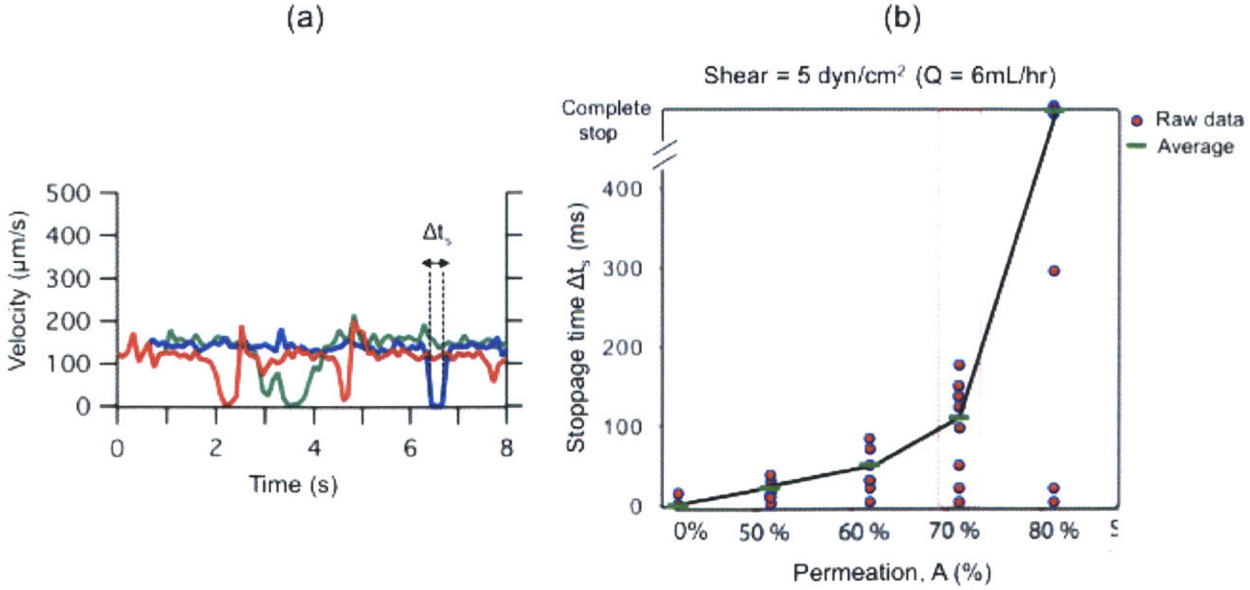

Fig. 4-7 (a) Instantaneous cell velocities on the porous surface elucidating the characteristic stop and go motion **(b)** Quantification of stoppage time as a function of permeation flux at a shear of 5 dyn/cm^2 (Q = 100 μl/min) (green bar represents average stoppage time).

Since the purpose of this thesis is to isolate specific cells from a mixture through molecular interactions between the antigens on the cells and their complimentary antibodies, we modeled the effect of relative cell velocity and the effect of stop and go motion on these surfaces. Therefore in this section we also theoretically understand the importance of reduced cell velocity on porous surface. Arrest of a cell bearing complimentary antigens to the antibodies covering the surface depends on the cell velocity, biochemical properties of the antigen/antibody pair and their concentrations on the cell and surface respectively. The cell rolling and arrest has previously been modeled as a two step process. [107]

$$[\mathbf{R}] + [\mathbf{L}] \leftrightarrow [\mathbf{R}\cdot\cdot\mathbf{L}]$$

$$[\mathbf{R}\cdot\cdot\mathbf{L}] \leftrightarrow [\mathbf{RL}]$$

The first step is responsible for describing the interaction of the antigens (EpCAM in our case) on the cells to the antibody (anti-EpCAM) bearing porous surface and can be characterized by the encounter rate (k_o). The second step describes the probability of bond formation when the complimentary antigen/antibody pair are in close proximity (P). Consequently, these two convection of the cells across the porous surface and the rate of chemical bond formation dictate the arrest the arrest of cells and is conveniently described using the non-dimensionalized Peclet number. These competitive forces can be incorporated into a single parameter that defines the probability of cell arrest (P)

$$P = \frac{\Lambda\delta}{1+\Lambda\delta} \tag{4-22}$$

And δ is the Dahmkohler number ($\delta = a^2K_{in} / D$; a = radius of circle of contact, K_{in} = intrinsic EpCAM: anti-EpCAM reaction rate and D is the cell diffusion coefficient) and Λ is the dimensionless encounter time between the cell antigen and the surface. This encounter time is given by

$$\Lambda = \frac{\tau}{a^2 / D} \qquad (4\text{-}23)$$
$$\tau = \frac{8a}{3U\pi}$$

As seen from Eqn. 4-23, the non-dimensionalized encounter time can be completely described by the cell dimensions (a, D) and the relative velocity between the cell and the surface (U). As seen from Fig. 4-8, with the increase in cell surface linear velocity, there is a decrease in probability of bond formation. At a cell velocity of over 400 µm/s the probability of bond formation and cell capture falls to 50%. Therefore we optimize the flow rate and permeation flux at a point where the velocity of the rolling cells is low enough to capture. From Fig. 4-5 we see that for a input flow rate of 6 mL/h and permeation of A=70%, the cell translational velocity is ~ 150 µm/s at at a distance of 2.5 cm from the inlet. This cell velocity corresponds to a theoretical bond formation and cell capture of 80% (Fig. 4-8). Additionally, we see the effect of the instantaneous stop and go motion on probability of capture. Even if the average cell velocity is high (~2000 µm/s), the probability of capture on the porous surface is still close tone owing to the characteristic stop and go motion where the instantaneously the cell velocity reaches zero and the complimentary antigen and antibodies have a large interaction time.

The modified Chang and Hammer model used above is a local model that addresses the microscopic interaction of the antigen and antibody in an external flow field. Even though our device introduces a transverse component of the velocity field compared to the one described initially in the Hammer model, the model remains valid as the external forces are accounted in the absolute cell translational velocity.

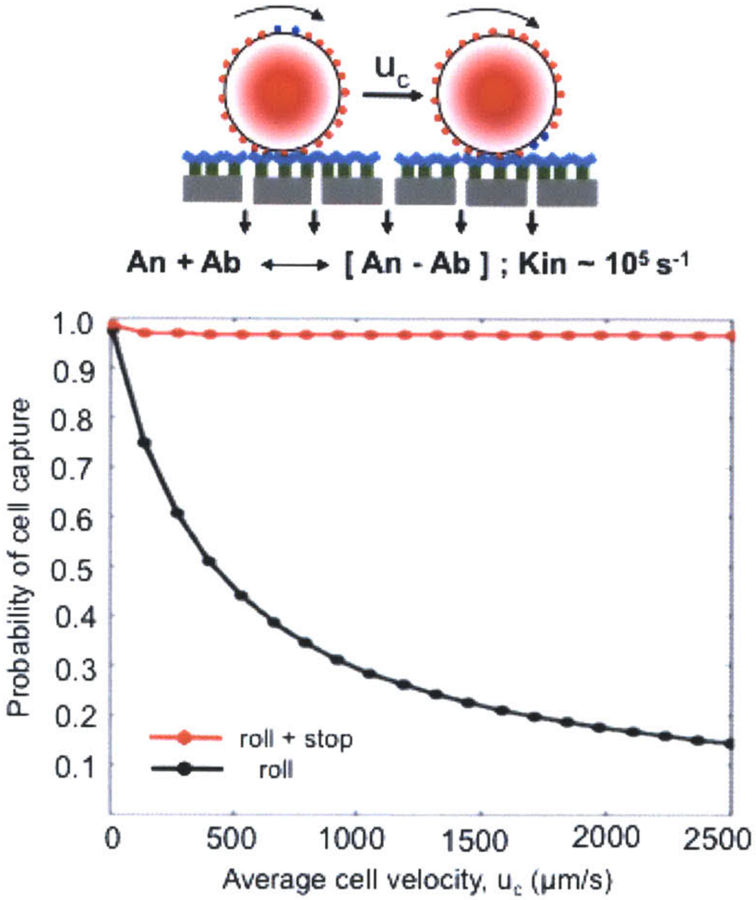

Fig. 4-8 Plot representing probability (P) of EpCAM antigen-Anti-EpCAM antibody as a function of cell surface velocity (black circles for solid surface and red circles on a porous surface)

4.8 Effect of shear on cell removal

Once the capture phase is complete and the specific cells have been immobilized on the porous surface, the bottom oulet is clamped and buffer flows through the top channel without any permeation through the nano-porous surface (section 4.1.2). The objective of this step is to increase the specificity of the device by dislodging the non-specific cells, while maintaining retaining the specific target cells. To ensure the attached specific PC3 cells do not detach with the washing buffer, it is imperative to calculate the shear experienced by the cells by the buffer. In general, the cells remain adherent if the total shear imparted on the cells (Fs) is less than the total adhesion force between the cell and the antibody covered porous surface (Fa), or,

$$Fs < Fa \tag{4-24}$$

The total adhesion force on a captured PC3 cell is evaluated by using the Bell model [108, 109] and is given by

$$Fa = f_c\, A_c\, C_s \tag{4-25}$$

Where f_c is the adhesion force for a single EpCAM/anti-EpCAM bond ($f_c = kT/r_0\alpha_c$) ~ 6.6 x10^{-6}dynes, A_c is the contact area of the non-deformed cell with the surface ($A_c = \pi r^2 \sin(\cos^{-1}(r-h' + h/r))$ ~ 315μm^2 and C_s is the cell surface antigen density (~125μm^{-2}) (descriptions and values of the parameters listed in Table 4-1). Consequently, the force required to dislodge a specific cell after capture is Fa ~ 0.25 dynes. On the other hand, the cell dislodging shear force on the cell surface during the wash step is given by

$$F_s = \frac{6\mu Q}{h^2 w} A_c \tag{4-26}$$

Using the values from Table 4-1, the shear force F_s ~ 1.7x10^{-6} dynes. Since the force require;d to break a single EpCAM/anti-EpCAM bond is greater than the shear force on the surface at 6 mL/h a channel with h=100 μm, w= 2mm this implies that even a single bond formed between the EpCAM antigen/anti-EpCAM is enough to overcome the shear force imparted by the fluid. In reality hundreds of bonds are formed between the cell and the surface. Therefore once a specific cell arrests in flow, the washing step is unlikely to remove it due to shearing at high flow rates. We found that a flow rate of 12 mL/h provides excellent capability to remove non-specific leukocytes, but not target cancer cells.

Parameter symbol (units)	**Parameter description**	**Value**	**Reference**
Kin	Forward rate constant for EpCAM/Anti-EpCAM binding	10^5 s^{-1}	[110]
r	Cell radius	6 μm	

r_o	Separation distance between receptors at min breaking force	0.5 nm	[111]
K	EpCAM/Anti-EpCAM equilibrium constant	3.3x10^{8} M^{-1}	[111]
D	PC3 diffusion constant	10^{-10} cm^{2}s^{-1}	
k	Boltzman constant	1.38 x 10^{-23} m^{2}kgs^{-2}K^{-1}	
a	Encounter radius	5 nm	[111]
h, h’	Cell-surface separation	10 nm, 50 nm	[108]

Table 4-1. Table listing the parameters and the associated values for calculation of probability of cancer cell capture and shear force required to break an EpCAM/anti-EpCAM bond.

4.9 Cell Capture on Fluid-Permeable Surfaces Exceeds Solid Surfaces at Increased Flow Rates

The capture efficiency of PC3’s on both porous and solid surfaces functionalized with either non-complementary anti-IgG or complementary anti-EpCAM are plotted as a function of total flow rate in Fig. 4-8a. Using a mixture of PC3’s and leukocytes at a ratio of 1:250, non-specific capture of PC3’s is minimal (~10%) on a solid anti-IgG surface due to the lack of complementary bonds and decreases rapidly with increasing flow rates. For a porous anti-IgG surface (A = 70%), the cell capture rate is slightly higher (~20%) and decreases more gradually with increasing flow rate, reflecting non-specific adsorption due to the enhanced transport to the surface as well as suction effects. For the solid anti-EpCAM surface, the capture efficiency achieves a maximum value of ~60% only at low flow rates (Q_{in} < 0.3 mL/hr). The capture efficiency drops off rapidly with increasing flow rate, becoming negligible by Q_{in} = 1.5 mL/hr. In comparison, the porous anti-EpCAM surface (A = 70%) achieves the optimal capture efficiency of 70 ± 3% up to relatively high flow rates of Q_{in} = 6 mL/hr (Fig. 4-9a). This is consistent with the theoretical maximum of 70% based on the fraction of streamlines that are expected to reach the surface. In comparison, no cells are captured on the flat surface for both anti-EpCAM and anti-IgG and only a few cells are nonspecifically adsorbed on the anti-IgG porous surface (Fig. 4-9c-f). As the flow rates are increased further on the anti-EpCAM porous surface, cell capture efficiency decreases to 15% at Q_{in} = 30 mL/hr. Nevertheless, the maximum effective flow rate of the porous anti-EpCAM surface is 20-fold higher than that on the solid anti-EpCAM surface, enabling a potentially transformative enhancement in processing throughput.

The shear-dependent capture of cells is illustrated by the concentration profile along the length of the channel (Fig. 4-9b). A stitched image of the entire length of the device at representative flow conditions (A = 70%, Q_{in} = 6 mL/hr) shows that cell capture increases cumulatively with distance, reaching ~70% at x = 4 cm as the shear field linearly decreases.

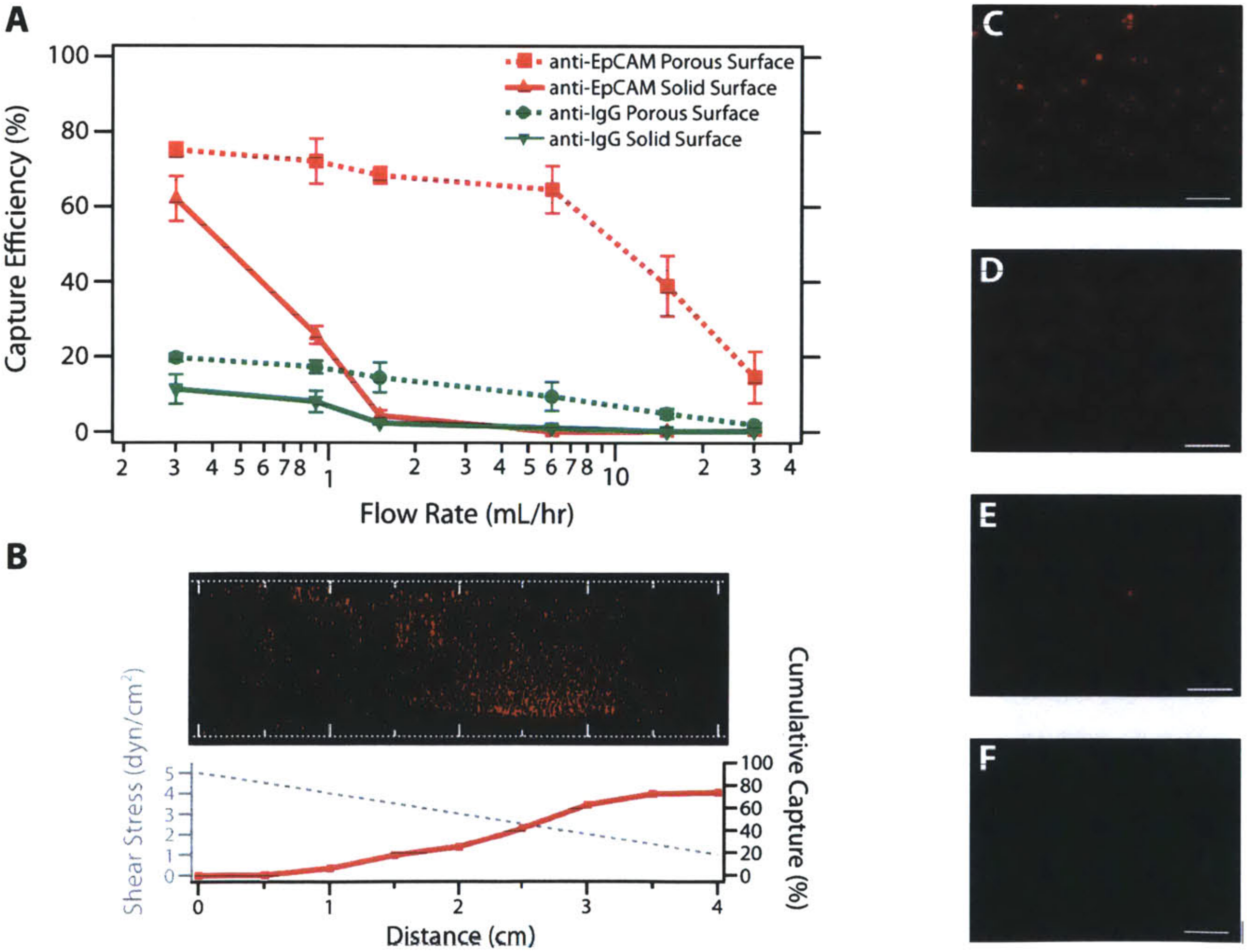

Fig. 4-9 (A) Capture efficiency of PC3 cancer cells at increasing flow rates on complimentary anti-EpCAM porous surfaces (red squares), anti-EpCAM solid surfaces (red triangles), non-complimentary anti-IgG porous surfaces (green circles) and anti-IgG solid surfaces (green triangles). Each marker and error bar is the average and standard deviation of 3 experiments. **(B)** Capture profile varies along the channel length on an anti-EpCAM porous capture surface at Q_{in}=6 mL/hr and A = 70%. The transverse wall velocity v_{w0} = 141 μm/s. Representative fluorescence micrograph of captured PC3 cells at x = 3 cm for **(C)** anti-EpCAM porous surface, **(D)** anti-IgG porous surface, **(E)** anti-EpCAM solid surface and **(F)** anti-IgG solid surface. Scale bar is 100 μm.

An additional insight from calculations in section 4.8 is the possibility of capture of cells with low expression of antigens on the cell surface. Since only a few bonds between the EpCAM/anti-EpCAM surface are required to stably arrest the cell, it is found that the capture efficiency of lower EpCAM antigen expressing PC3-9 cells (5000/cell) was comparable (45% ± 4%) to the higher EpCAM antigen expressing H1650 cells (500,000/cell) (58%±3%) (Fig.4-10).

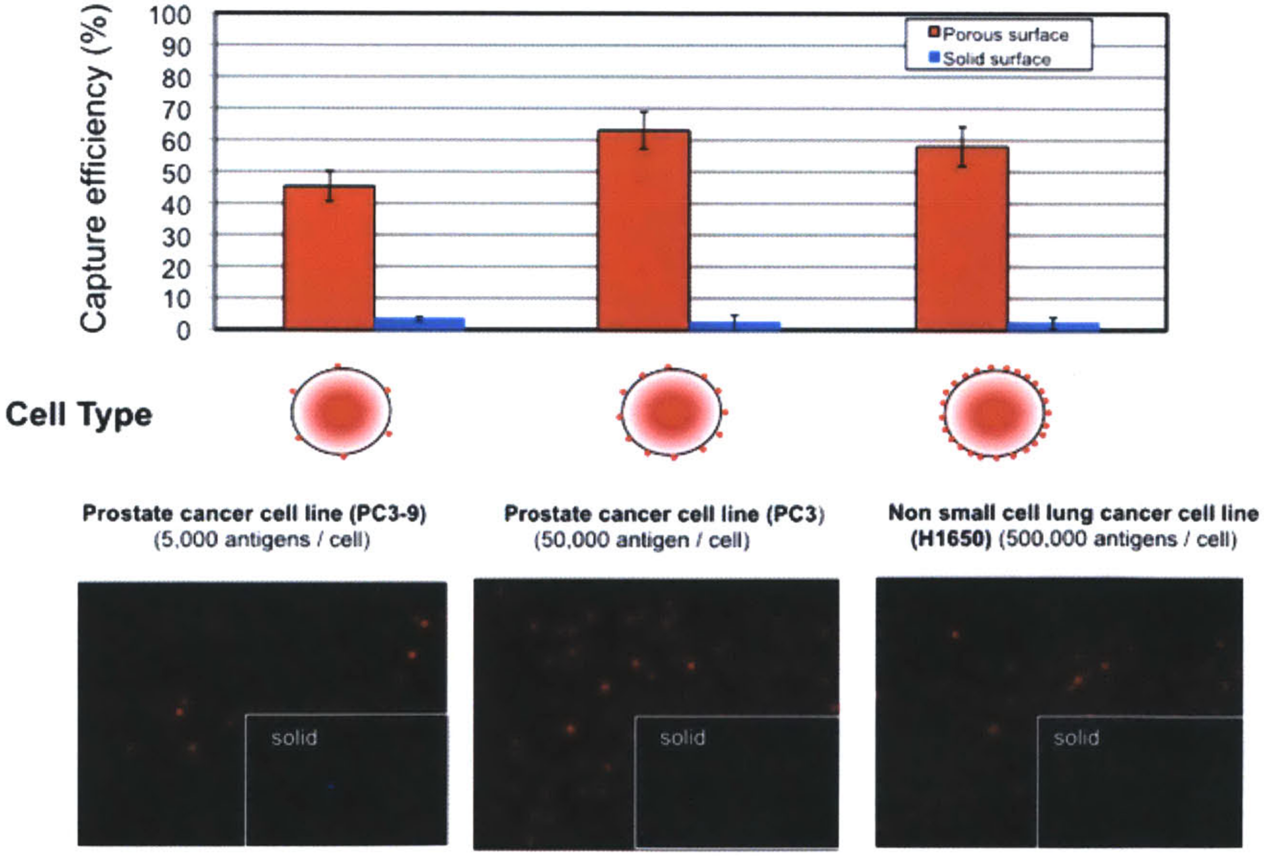

Fig. 4-10 Capture efficiency of PC3-9, PC3 and H1650 cancer cells on complimentary anti-EpCAM porous surfaces. Each marker and error bar is the average and standard deviation of 3 experiments. The blue (DAPI) images represent nuclear staining of all the cells, red (CTO) images represent the specific cancer cell type.

4.10 Summary

In this chapter we demonstrate the superiority of antibody functionalized porous surfaces for capturing cells at high flow rates, compared to its solid counterparts. We demonstrate that fluid permeable nano-porous surface enhance mass transport of cells from the channel lumen to the reactive porous surface that bare the complimentary antibodies for specific cell capture. We found that in a well mixed sample entering the channel, where the cells can be assumed to uniformly distributed, the percentage cells convected to the surface is proportional to the permeation flux through the surface. Additionally, we demonstrate that on a fluid permeable surface, once the cells convect to the surface, the momentum transfer from the axial fluid flow shears cells along the surface inducing cell rolling. Further, since fluid permeates through the porous surface along the shear and hence the cell velocity decreases close to 150 μm/s towards the channel end. A model of probability of capture of a target cell rolling on a reactive surface shows that probability of capture is 80% when the cell velocity is 150 μm/s and decreases precipitously at the cell velocity increases. Finally, we demonstrate that cell capture efficiency of of prostate cancer cells (PC3) as a function of flow rate and show that there is a 20 fold increase in throughput over solid surfaces. Further we quantify the capture efficiency of low expressing prostate cancer (PC3-9 cells), 45±4%, and high expressing prostate cancer (PC3) and lung cancer (H1650) cell lines, 60±3% and 58±3% respectively. The above-mentioned studies have resulted in improving the capture efficiency of specific cells on antibody functionalized fluid permeable porous surfaces at a flow rate that is 30 fold higher than the solid counterpart microfluidic device of same dimensions (Fig. 4-10).

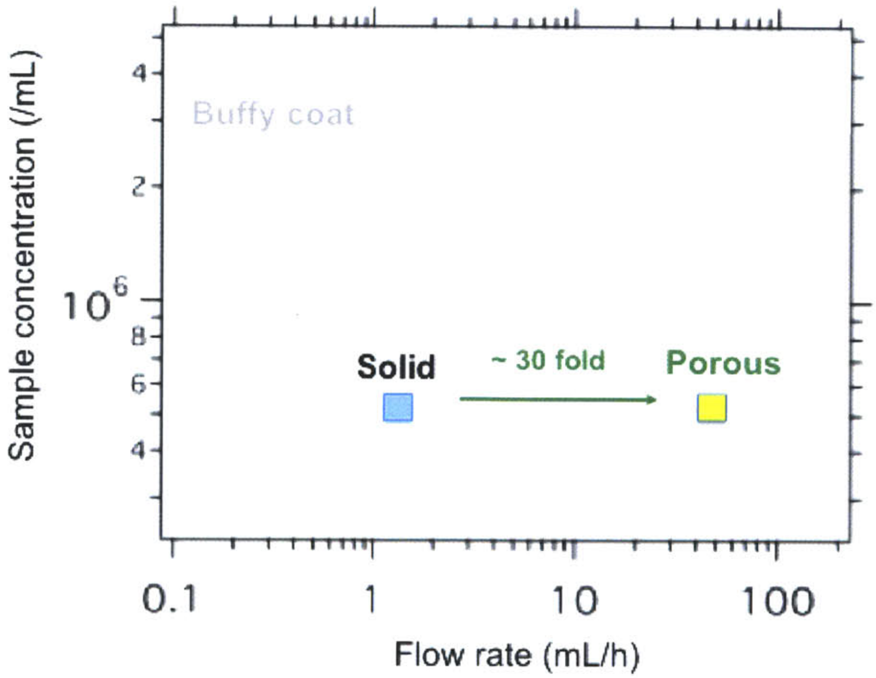

Fig. 4-11 Schematic showing a 20 fold improvement in flow rate while maintaining target cell capture efficiency (PC3) at a given concentration of background white blood cells (500,000 cells/mL)

Chapter 5

Partly-Porous Surfaces Enable Enhanced Cell Capture at High Flow Rates while Suppressing Surface Fouling

Introduction

One consideration unique to this device architecture is that cells may be advected downward so rapidly that they overwhelm the capture surface. This would suppress the effectiveness of the device, since layers of accumulated cells would block access to the capture surface ("caking" or stagnant bioparticle layer formation) and ultimately impede transverse fluid flow through the surface.

In this chapter, we consider the effect of large number of general population cells on capture efficiency on a porous surface device and develop a device that alleviates formation of stagnant leukocyte layer of cells at a maximal input sample concentration, in order to truly make the device high throughput. In section 5.1, we qualitatively understand the operating conditions under which stagnant leukocyte layer form. In section 5.2, we quantify the effect of stagnant leukocyte layer on specific cell capture efficiency for low antigen expressing and high antigen expressing cells. Based on previous literature, we introduce basic concepts that need understanding during stagnant layer formation of colloids on porous surfaces and define critical parameters that prevent formation of stagnant layers in section 5.3. Further, in section 5.4 we experimentally understand whether the formation of these stagnant layers of leukocytes is a short term or a long term phenomenon. During this study, we try to dig deeper to understand reasons for stagnant layer formation on the channel edges, even in dilute suspensions and analytically derive velocity and shear profiles for channels with low aspect ratios in section 5.5. In section 5.6 we extrapolate these derivations for a porous surface and a spatially modified microfluidic device intended to alleviate the stagnant layer formation problem in thin channels. Finally, in section 5.8, we implement the concept of partly-porous surface for a multiplexed 8 channel device with the capability of processing samples at a flow rate of 48 mL/h.

5.1 Qualitative observations on stagnant layer formation and effect on capture efficiency of target cells

Fluid permeable porous surfaces enhance mass transport to the surface and therefore allow interaction of specific cells with the reactive porous surface. In the previous chapter we demonstrated a microfluidic device based on fluid-permeable, antibody-functionalized membranes that can capture specific cells at high flow rates using two unique physical mechanisms [112]. First, streamlines are diverted from the device outlet to the membrane, allowing cells to be transported directly to the capture surface. Second, the diminished flow parallel to the surface results in reduced shear, promoting increased cell-surface interactions for selective capture of target cells and the removal of non-specific background cells. This approach overcomes the limitations on selective capture associated with "transport" and "reaction" due to interfacial effects and low Reynolds numbers [35, 36]. The permeation flux and hence the porous surface wall velocity were determined using modified Darcy's law.

However, when operating at high flow rates without being transport limited, a different complication arises - excess build-up and fouling of cells, known as concentration polarization and "caking" [85]. We observed formation of stagnant cell layers on the porous surface at cell concentrations above $1.5\text{x}10^6$ /mL (or cell volume fraction of $\phi_o \sim 0.03$) (Fig. 5-1) and flow rates of 6 mL/hr and permeation flux of 70%. The combination of flow rate and permeation was chosen based on section 4-8 where we showed the specific cell capture efficiency to be maximum at Q=6mL/hr and A=70%. Keeping the shear due to fluid flow and permeation constant, we observed that the stagnant layer formation is a function of inlet sample cell concentration. In order to demonstrate this we used leukocytes ("buffy coat") isolated from whole blood using deterministic lateral displacement [101] and resuspended to different concentrations to understand the effect of concentration on caking. These cells were fluorescently labeled (CellTracker calcein green, Invitrogen, Carlsbad, CA) following the manufacturer protocol. For each condition the entire channel was imaged using a 4X objective and a 10 X objective. For solid surfaces no buildup of leukocytes was found on the surface.

However, for porous surface, 15% of the total channel area was covered with leukocyted at inlet cell volume fraction at ϕ_o~0.01 (500,00 cells/mL) and 90% was covered at ϕ_o~0.03 ($1.5\text{x}10^6$ cells/mL) (Fig. 5-1)

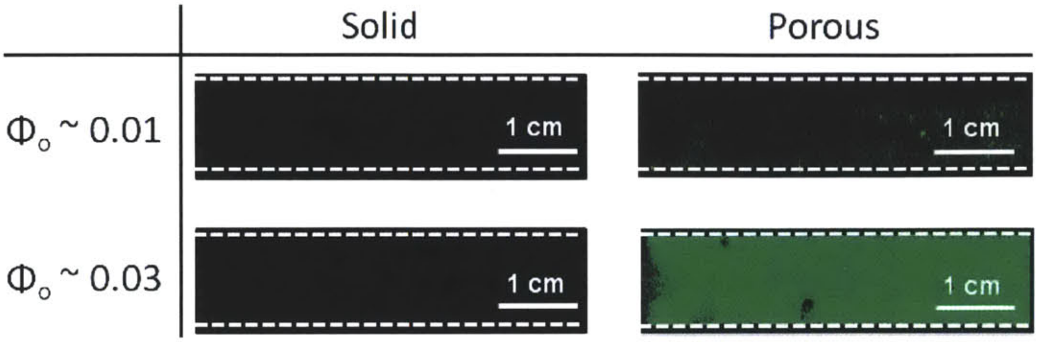

Fig. 5-1 (Left) No deposition of leukocytes from buffy coat on solid surface (Right) enhanced mass transport of the porous surface at A=70% causes ~ 15% area coverage due to stagnant layer formation at ϕ_o~0.01 ($0.5\text{x}10^6$ cells/mL) and ~90% area coverage at ϕ_o~0.03 ($1.5\text{x}10^6$ cells/mL).

5.2 Effect of stagnant layers on specific cell capture

In this section we explore the effects of stagnant layer formation on specific cell capture. Previously, in literature formation of stagnant cell layer of the general background cell population has been associated with the waning performance of porous surfaces during filtration [113]. Formation of stagnant layer on porous surfaces poses two problems. Firstly, formation of a stagnant layer physically cuts off access to the anti-EpCAM antibodies immobilized on the porous surface. As a result, the EpCAM antigens on the cells cannot interact with the anti-EpCAM on the surface and therefore cannot be arrested. Secondly, formation of stagnant 'cake' layer reduce permeation flux responsible for enhanced mass transport at high flow rates if the resistance offered by the stagnant layer is comparable to other elements of the device. The decreased permeable flux is due to addition of a resistive component to the bottom arm of the lumped resistive model (R_c). The resistance offered by this cake layer can be described using the Carman-Kozeny equation.

$$R_c \sim \frac{180(1-\varepsilon)^2\delta_c}{d_p^2\varepsilon^3} \tag{5-1}$$

Where, $\varepsilon \sim$ porosity of the cake layer and the value lies between 0 and 1, δ_c is the cake thickness, d_p is the cell diameter. Assuming cells are sphereical, a monolayer ($\varepsilon \sim 0.6$) of 10 μm cells has $R_c \sim 10^{12}$.

However, in our device we see that the nano-porous surface with a pore diameter of 200 nm and porosity of 10% has resistance on the same order as resistance due to a monolayer of cells (Table 3-1). In this scenario the cake layer resistance and the membrane resistance is overwhelmed by the addition of the external resistances to the top and bottom outlets ($\sim 10^{13}$) which continue to allow permeation flux through the nano-porous surface and deposition of multiple background cell layers. In order to understand effect of stagnant cell layers on specific cell capture on the anti-EpCAM coated porous surface, we pre-conditioned the device by forming stagnant layers of leukocytes on the surface. These stagnant cell 'cake' layers were quantified by scanning the entire channel using a 4x objective and was normalized against the total channel area (Section 5.4.1). Prostate cancer cell line PC3 were spiked into the buffer solution at 1000 cells/mL and 1 mL solution was processed through the chip at 6 mL/hr, A=70% permeation. During these experiments, we measured the permeation fluxes through the porous surface for the duration of the experiment for each condition and found that it remained unchanged and consistent at 70%.

Additionally, we observed that the capture efficiency of larger number of EpCAM antigen expression of PC3 cells (50,000 /cell) remained constant at ~ 70% until the cake area coverage was ~ 60%. However, the capture efficiency reduced significantly (~ 50%) past cake area coverage of 78%. For the lower antigen expressing PC3-9 cells (5000/cell) the effect of cake area coverage was more significant. The capture efficiency decreased from 50% ± 4% at stagnant bioparticle coverage of 18%±3% to capture efficiency of 25 % ± 4% at a stagnant bioparticle coverage of 58% ± 4% (Fig 5-2). Based on these results, we believe that porous surface coverage with background leukocytes in the sample screen the target cells from interacting with the specific antibodies. In the following sections we dive deeper into the theory of stagnant layer formation to understand the forces and mechanisms that are responsible for caking and alleviate the phenomenon, restoring the optimal operation of porous surface microfluidic devices in concentrated samples.

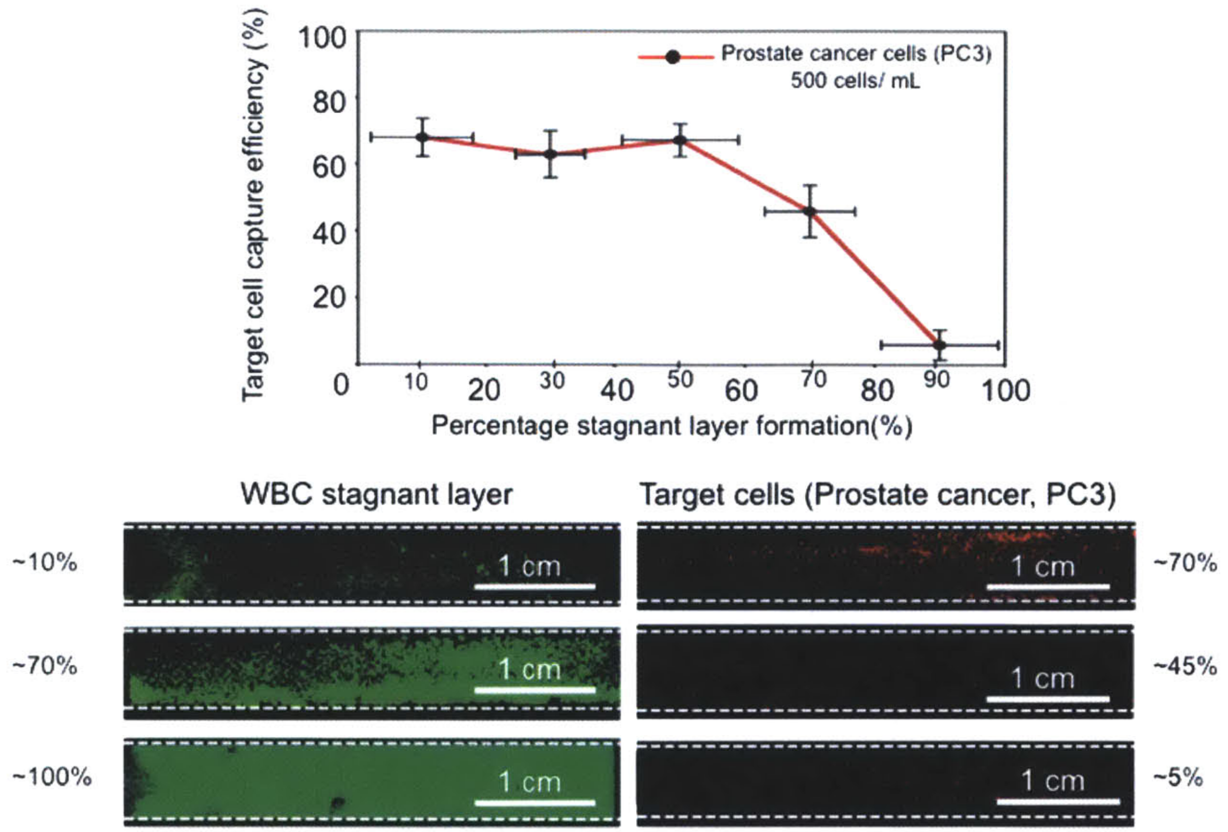

Fig. 5-2 Capture efficiency of specific prostate cancer cells (PC3) as a function of cake area coverage.

5.3 Theoretical background on stagnant layer formation

Buildup of stagnant layer of large particles such as cells, much larger in size than the nanopores on the surface, is a result of very high convective drag that enhances mass transport of cells to the nanoporous surface relative to the shear forces that translate the cells and the suggested back transport mechanisms (lift forces, stokes-enstein diffusion diffusion) in the system [113]. Since, our system operates in laminar regime ($Re \ll 1$), inertial forces are negligible. Additionally, for a 10 μm cell diameter the Stokes-Einstein is 2×10^{-7} cm^2/sec, which is small compared to the permeation flux through the nanoporous surface. Therefore the formation of the stagnant layer is due to excessive permeation flux relative to the shear forces translating the cells. During stagnant layer formation, five stages have been clearly demarcated in the literature in the past [8]. These are described as (1) Fast initial sorption of macromolecules (2) Buildup of the first mono-layer

(3) Buildup of multi-layers (4) Densification of multi-layers. Stage 3 and 4 are associated with decreased permeation flux through the porous surface. In this thesis, we will only focus on conditions up until formation of the monolayer, as it is the onset of the monolayer formation that is detrimental to specific cell capture (see section 5.2).

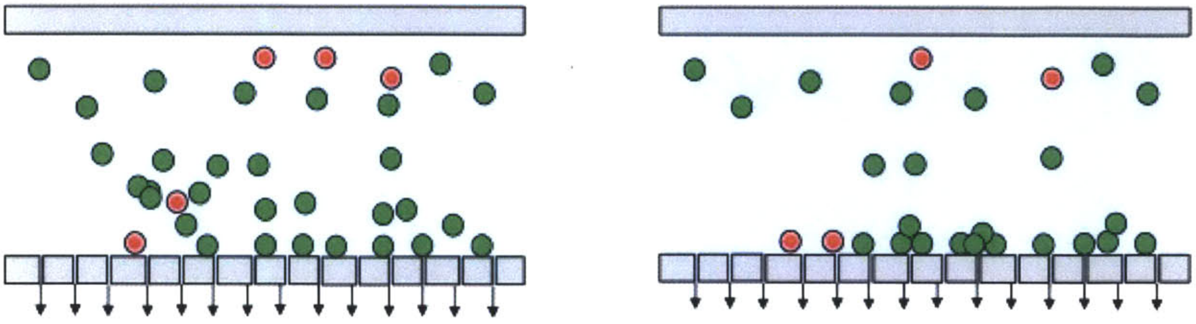

Stage 1- Initial deposit

Stage 2 - Aggregate formation

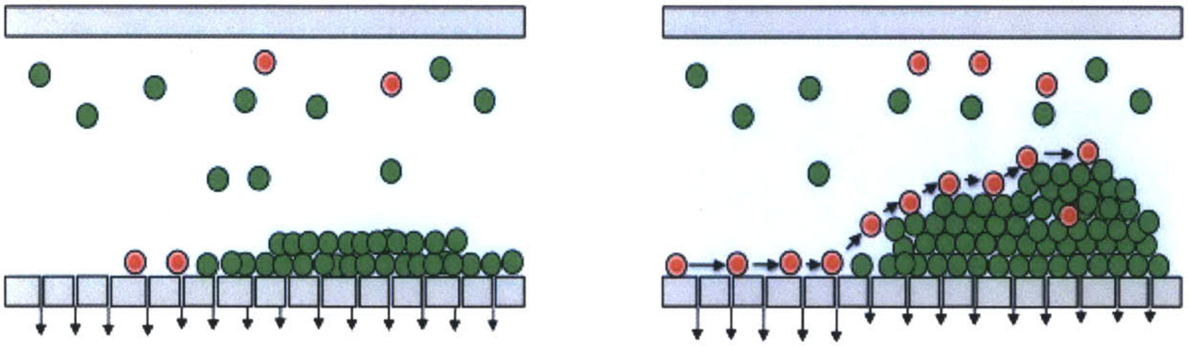

Stage 3 - Sublayer rearrangement

Stage 4 – Multiple layer formation

Fig. 5-3 Periods of different physical phenomena during cake formation and flux decline [8]

5.3.1 Theoretical considerations and stagnant layer onset modeling

In order to understand the qualitative observations in section 5.1 and 5.2, we explore the forces underlying the stagnant layer formation. The theoretical analysis consists mainly of two parts, the fluid and particle trajectory calculations (see section 4.2) and the stagnant layer deposition and permeation flux calculations. The governing equations for the fluid and particle trajectories make use of Navier-Stokes equations and modification of Newton's second law (Faxen's law). To calculate the onset of cake growth we use the critical flux and critical distance calculations. Together, these subdomain models allow prediction of stagnant layer formation in terms of global parameters such as sample concentration, particle radius, channel shear and permeation flux. In order to simplify the model, the following assumptions are considered.

1) Sample is a dilute suspension of cells; The particles do not influence the fluid field nor do they interact with each other
2) Cells are rigid and non-deformable and Brownian motion and inertial effects are negligible
3) Pressure difference and the wall flux is constant
4) Material properties of the fluid and membrane remain constant and the sample is well mixed, implying that the entering particles are uniformly distributed at entrance.

The physical situation under consideration is described in Fig. 5-4. The sample suspension is composed of a Newtonian fluid and neutrally non-bouyant cells in the bulk are convected from the dilute suspension to the porous surface. In the bulk the cells do not interact with each other and the cells follow the fluid streamlines. The particle suspension far away from the wall is constant and given by ϕ_o. Close to the porous surface a concentrated layer of cells translates and acts as a non-Newtonian fluid and the flow of solution above this layer imparts a tangential shear stress $\tau(x)$ which we assume to decrease linearly along the channel length because of constant permeation flux. This shear stress is position and viscosity dependent and is given by

$$\tau(x) = \frac{6\mu_o \eta(\varphi) Q_{out}}{h^2 w}(1 - \frac{Q_{in}}{Q_{out}}.\frac{x}{L}) \tag{5-2}$$

The effective viscosity of the concentrated cell layer has been experimentally found and described in terms of the local concentration [114]. As can be seen from Eqn. 5-3, the effective viscosity in the concentrated cell layer increases with the cell volume fraction

$$\eta(\phi) \sim \{1 + 1.5\frac{\phi_w}{(1 - \frac{\phi_w}{0.58}}\}^2 \tag{5-3}$$

Where ϕ_W is the cell volume fraction in the stagnant bioparticle layer. Previously, Romero and Davis modeled a similar system where the permeation flux through the porous surfaces was small. However, even in this system they found that the formation of stagnant layers occurs when the cell packing fraction at the wall reaches a certain maximum (ϕ_{max}). Therefore, the onset of stagnant bioparticle layer is a function of three key variables: Shear stress, permeation flux and cell volume fraction in the concentrated layer.

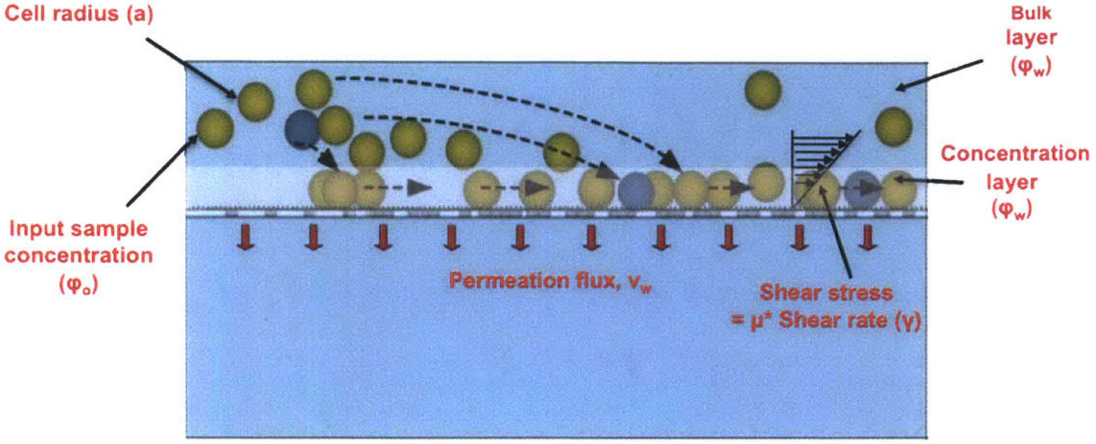

Fig. 5-4 Schematic showing the important parameters under consideration for onset of stagnant layer and the difference in the cell volume fractions in the bulk and concentration layers.

However, avoiding stagnant layer formation scenario requires that the flux of cells being advected to the surface must not exceed the flux of cells translating across the surface, or at steady state

$$\dot{M}_{in} - \dot{M}_{out} = \int_0^{\partial_{fl}} u_c(\phi)dy - \int_0^x V_w \phi_o dx > 0 \tag{5-4}$$

This condition can be achieved at a given bulk cell concentration (ϕ_o) by making the permeation flux as large as possible while retaining sufficient axial flow enough to drive cell rolling due to shear stress. Romero and Davis have considered the scenario of hard spheres accumulating at a porous surface and have derived an expression for a critical distance x_{cr} where particles become close-packed in a "cake" layer [115]:

$$x_{cr} = \frac{R_c^{\,4}\tau(x)\hat{Q}_{cr}(\varphi_0)}{\varphi_0 U_{w0}^{\,3}} \tag{5-5}$$

where *a* is the particle radius, $\tau(x)$ is the surface shear stress, φ_0 is the initial bulk volume fraction and μ_0 is the solution viscosity.

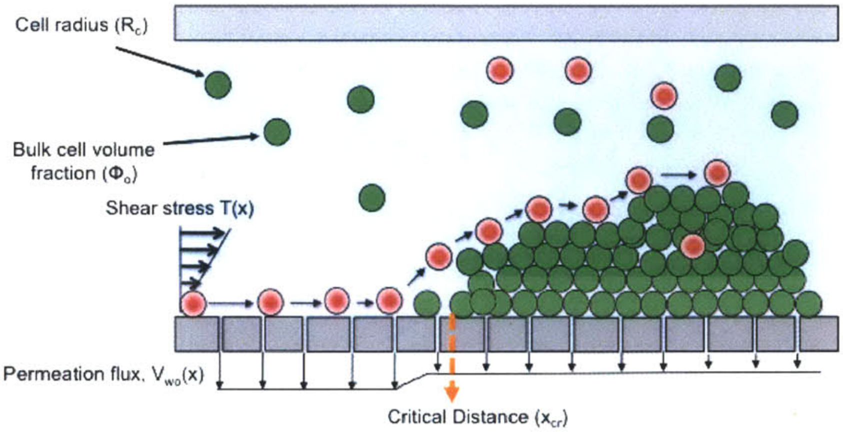

Fig. 5-5 Schematic depicting the critical distance for the onset of stagnant layer cake formation and the important parameters associated.

The critical permeation flux $\hat{Q}_{cr}$ is primary a function of the bulk cell concentration and is given by:

$$\hat{Q}_{cr}(\varphi_0) = \int_{\varphi_0}^{\varphi_{max}} \left\{ \int_{\varphi_0}^{\varphi_{max}} \frac{D(\varphi')\,d\varphi'}{\varphi'\eta^2(\varphi')} \right\} \frac{(\varphi-\varphi_0)\,D(\varphi)\,d\varphi}{\varphi\eta(\varphi)} \tag{5-6}$$

where φ_{max} is the maximum packing density on the surface, assumed to be ~ 0.6 for hard spheres and $\eta(\phi)$ is the effective viscosity as described in Eqn. 5-3. This is a conservative estimate which may underestimate the packing density of deformable cells [115]. Nevertheless, the empty space between cells in a close packed layer (~40%) is still considerably larger than the membrane porosity (~10%), making it unlikely that a single close-packed layer of cells would block a significant number of pores or lead to a large cake resistance (R_c~ 10^{12}) thereby maintaining constant permeation flux. This calculation thus assumes that the presence of ~10 μm cells does not affect the fluidic resistance of the membrane or associated transverse flux. The permeation flux and thickness of stagnant particle layer formation in the critical and the pre-critical region are defined as:

$$\text{Pre-critical region } (x < x_{cr})\text{: } V_w(x) = V_{w0} = \frac{J}{A_m}; \partial_{st} = 0 \tag{5-7}$$

$$\text{Post-critical region } (x > x_{cr})\text{: } V_w(x) = V_{w0} = \frac{J}{A_m}; \partial_{st} = 2H_o[1-(\frac{x_{cr}}{x})^{1/6}] \tag{5-8}$$

Where, δ_{st} is the thickness of the stagnant layer formed along the porous channel. Onset of caking along with the thickness of the stagnant layer achieved as a function of distance from the entrance of the channel is shown in Fig. 5-6.

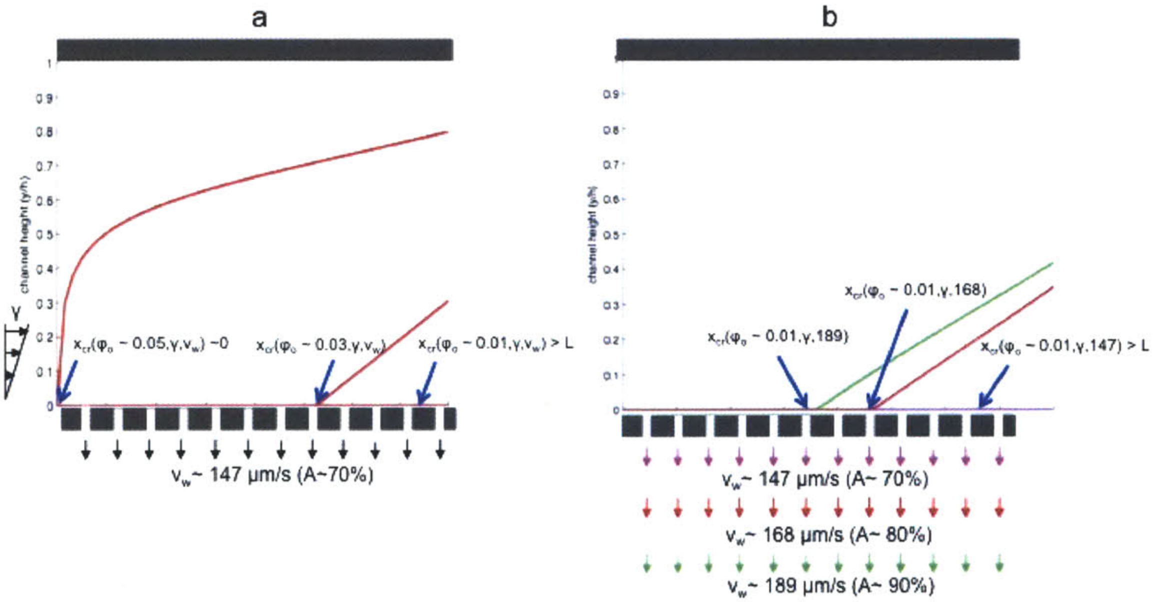

Fig. 5-6 (a) Distance from the device entrance where the caking onset takes place and the thickness of the cake reached at each location as a function of feed concentration ϕ_o (0.05, 0.03 and 0.01) **(b)** and, permeation flux v_w (A=70%, 80% and 90%).

Phase diagrams for the critical distance x_{cr} as a function of axial distance x and initial cell volume fraction φ_0 at varying permeation fluxes are shown in Fig. 5-6. To prevent caking,the critical distance x_{cr} should exceed the device length L at any point along the length of the channel so that the particle fraction on the porous surface never reaches its maximum cell packing density, φ_{max}.

In general, the critical distance x_{cr} decreases with increasing initial cell volume fraction φ_0, since a smaller enhancement in concentration is required to reach the maximum. In the case of minimal permeation flux (A = 10%), slow advection to the surface means that caking will only occur at relatively high bulk volume fractions. For instance, for $\varphi_0 = 0.04 \sim 2 \cdot 10^6$ cells/mL, φ_{max} is reached at x_{cr} = 3 cm. Experimentally, operating in this regime leads to a visible buildup of white blood cells on the reaction surface, despite the lack of specific cell-surface interactions. A further increase to $\varphi_0 = 0.05 \sim 2.5 \cdot 10^6$ cells/mL, corresponds to x_{cr} essentially at the entrance, which is not a usable condition. In general, operating at this minimal flux regime (A = 10%) is both inefficient and unselective, since 90% of the cells never reach the surface, but those that do are not subjected to sufficient shear to remove white blood cells while retaining cancer cells.

At the higher permeation flux described previously (A = 70%) and $\varphi_0 = 0.1$; x_{cr} = 0.8 cm, corresponding to caking within the device (Fig. 5-7). Instead, at $\varphi_0 = 0.1$, corresponding to ~ 500,000 cells/mL, the critical length x_{cr} = 5 cm is larger than the length of the channel (L = 4 cm) and caking should not occur within the device. Experimentally, device operation was optimal under these conditions, achieving efficient cell transport, selective capture and minimal accumulation of white blood cells at relatively high flow rates.

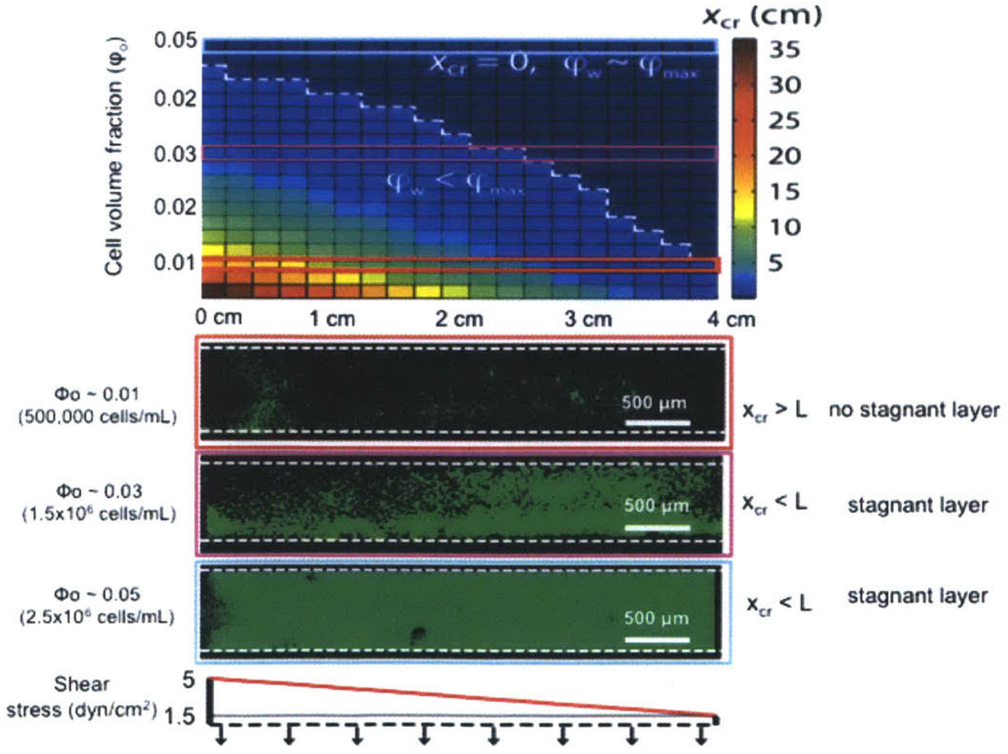

Fig. 5-7 High permeation flux (A = 70%) condition. At a critical value of initial volume fraction, the maximum close packing is reached along the length of the channel, causing excess cell buildup ("caking") and hindering cell capture (white dotted line). Devices were operated in the optimum regime ($\varphi_o = 0.1$, Q_{in} = 6 mL/hr, A = 70%) to maximize throughput without excess cell buildup (red line).

5.4 Temporal formation characteristics of stagnant bioparticle layers

In the previous section we investigated important parameters that dictate steady state onset of stagnant layer formation on the porous surface. The question remains as to how long it takes to reach this steady state? Does it deposit very quickly, on the order of seconds or minutes or is a much longer term phenomenon. An understanding of the temporal stagnant layer growth would allow us to define the operating conditions for the porous surface device. In order to understand the timescale at which this cake layer forms, we used fluorescently labeled white blood cells to track fraction of channel area covered by cake as a function of time.

5.4.1 Image analysis of stagnant layers

Caking kinetics were analyzed using built-in functions in MATLAB. Grayscale images of accumulating fluorescent cells were thresholded to binary black and white images using Otsu's method. This threshold value was recomputed for every image to compensate for photo-bleaching and manually verified. The total area coverage of fluorescent cells was measured using a pattern-weighted formula that accounts for distortions due to pixel biasing. Spatially localized caking phenomena were assessed by integrating pixel intensities for selected regions of interest of varying width and distance from the centerline.

5.4.2 Temporal growth of stagnant layers

In section 4.8 we found that a permeation flux of 70% through the porous surface allowed a 20 fold increased throughput (6mL/hr) while maintaining the capture efficiency (~73%) over its solid counterpart in PC3 cells. Keeping the input feed cell fraction constant, the rate of stagnant bio-particle layer formation increased with increasing percentage permeation flux. At A=50%, the time taken to form a monolayer of leukocytes ~ 400s at $\phi_o \sim 0.05$. However, at $\phi_o \sim 0.03$ and $\phi_o \sim 0.01$, the fractional area covered saturates before reaching ~ 0.6 (Fig. 5-8). At these low cell volume fractions even though considerable area remains "un-caked", the throughput remains limited because of lower number of cells/mL. However, at A=70% we see substantial fractional area of the channel covered for $\phi_o \sim 0.05$, 0.03 and 0.01. At $\phi_o \sim 0.05$, fractional area coverage reaches 0.6 around 220 s, whereas $\phi_o \sim 0.03$ saturates at 0.6 at 1050 s. A lower cell volume fraction of $\phi_o \sim 0.03$ saturates at 0.5 ~ 1200 s. It is however, interesting to note that even for low permeation conditions and cell fraction volumes in the bulk, there is stagnant bioparticle layer buildup on along the channel edges. Analysis of this phenomenon will be studied in the next section. It is also to be emphasized that the rate of particle deposition is nearly constant up until the steady state is reached for each combination of input cell feed fraction, shear rate and permeation flux. This phenomenon can be explained because the permeation flux through the surface is dependent and limited by the resistance of the membrane (10^{12}) and output bottom resistance (10^{13}) compared to the low resistance offered by the monolayer of cells (10^{12}) on the surface according to Carman-Kozeny equation. Therefore theoretical predictions for the stagnant bioparticle layer formation in our system follow the standard filtration theory for dead end filtration systems for operating regimes where stagnant bioparticle layer forms [116].

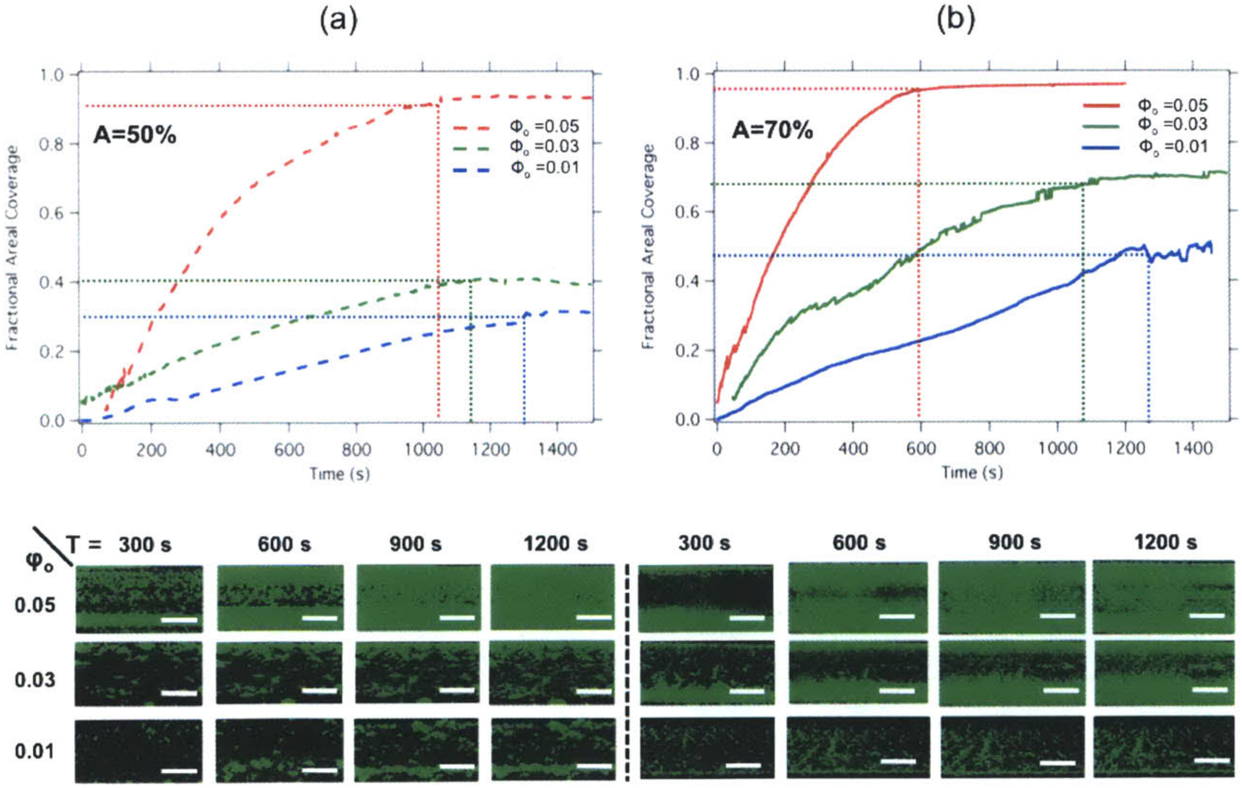

Fig. 5-8 (a) Channel area fraction growth rate for A=50% at ϕ_o = 0.05, 0.03 and 0.01 **(b)** for A = 50% at ϕ_o = 0.05, 0.03 and 0.01. Scale bar = 500 μm

Color coded kymographs represent the deposition of fluorescently labeled leukocytes across the width of the channel on the porous surface over the span of ~ 1200 s. We see that for a permeation flux of 70% the stagnant bioparticle layer formation occurs at higher feed fractions (ϕ_o~0.03) and the onset happens around ~ 200 s for the top edge and 240 s for the bottom edge (Fig. 5-9).This is represented by the red color on the kymograph which indicated formation of at least a single monolayer of leukocytes on the surface. The asymmetry in cake onset could be due to local porosity and particle distribution across the channel. With time, as more leukocytes get to the surface, the small immobilized layer of cells acts as a catalyst for the stagnant layer to grow inwards towards the center. It was experimentally observed that once a critical size of stagnant layer (> 500 μm^2) is reached, it becomes a local barrier for the cells that travel with linear surface trajectory directly behind it thereby allowing growth of stagnant layer over time. Similar conditions are seen for A=50%, however, for this condition the stagnant layer formation begins at a higher concentration of ϕ_o~0.05 or $2.5x10^6$ cells/ mL.

In the pictures shown in Fig. 5-8 it is interesting to note that even for low permeation conditions and cell fraction volumes in the bulk (ϕ_o~0.01), formation of stagnant bioparticle layer buildup along the channel edges and small islands in the center were observed. Formation of small islands for different permeation conditions and at low cell volume fractions can be described by the local variation in the porosity of the surface which leads to a imbalance of permeation relative to the local shear field. Upon measurement of these small islands, the size of most these islands was less than $100\mu m^2$ at the end of the experiment.

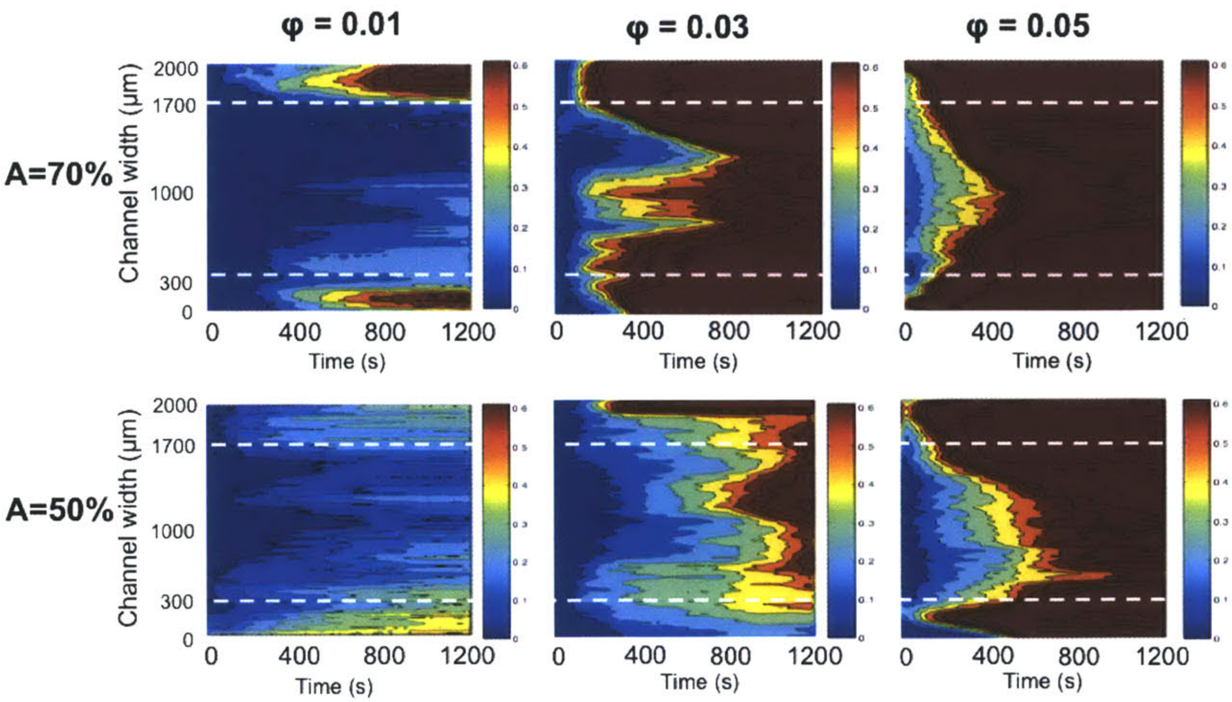

Fig. 5-9 Kymographs of cake growth for different sample feed fractions (ϕ_o = 0.01, 0.03 and 0.05) and permeation fluxes (A=50% and 70%).

Further, analysis of the growth rate of stagnant layer formation at the edges (~ 300 μm from the wall) and center of the channel showed that the stagnant layer grows faster along the edges (~10 fold in the transparent blue region) in comparison to the center of the channel (Fig. 5-10) till both reach saturation. The transparent red section in the figure demarcates the amount of time it takes for the porous surface to form a monolayer (fractional coverage ~ 0.6). We see that although the edges reach the monolayer stage at ~170 s, the middle part never reaches the monolayer stage. Theoretical understanding of why this occurs will be studied in the next section.

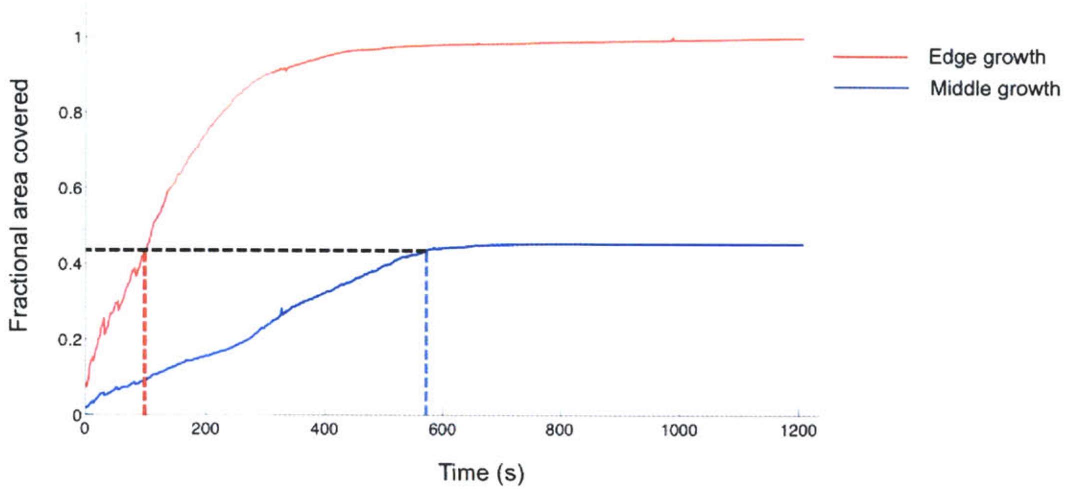

Fig. 5-10 Fractional area coverage as a function of time for the edges (red) and middle of the channel (blue).

5.5 Edge effects in microfluidic channels

The stagnant leukocyte layer growth experiments showed that the onset of cake first happens within 300 μm from the channel edge (Fig. 5-9). We believe that this phenomenon is a result of the wall edge effects of the microfluidic channel which reduces the tangential shear that translates the cells along the porous surface. The resulting imbalance between the shear and permeation flux results in initiation and continuation of stagnant layer growth.

Usually, analysis of microfluidic devices neglects the role of the side walls of the channel due to the assumption that the width of the channel is large compared to its height. In our device, the width to height ratio (w/h) is ~ 20. To evaluate the edge effects we begin with the navier stokes equation, derive an analytical expression for $v_x(y,z)$ and finally use the velocity field in the x direction to find the shear stress in the channel with the presence of walls.

Navier stokes equation in the vector form can be written as

$$\rho\frac{\partial v}{\partial t}+\rho v.\nabla v=-\nabla p+\mu\nabla^2 v+\rho g \tag{5-9}$$

Eqn. 5-9 simplifies based on the assumptions (1) steady state and fully developed flow (2) no velocity components in y- and z- direction with pressure variation along x, resulting in

$$0 = -\nabla p + \mu \nabla^2 v_x \tag{5-10}$$

With boundary conditions that velocity on each surface is o

$$\begin{aligned} &BC's : y = \pm h/2, v_x(\pm h/2, z) = 0 \\ &z = \pm w/2, v_x(y,0) = v_x(y,w) = 0 \end{aligned} \tag{5-11}$$

Additionally, since in this case we are not going to use the general assumption that w>>h, we also cannot assume that Eqn. 5-10 is homogeneous. The velocity component v_x, can therefore be written as a sum of two terms, one that depends on y coordinate only and the second term that depends on y- and z- coordinates:

$$v_x(y,z) = v_x(y) + \phi(y,z) \tag{5-12}$$

where,

$$v_x(y) = \frac{\Delta p h^2}{8\mu L}(1 - \frac{4y^2}{h^2}) \tag{5-13}$$

Substituting Eqn. 5-12 in 5-13 we get two equations

$$\begin{aligned} 0 &= \frac{\Delta p}{L} + \mu \frac{d^2 v_x}{dy^2} \\ 0 &= \frac{\partial^2 \varphi}{\partial y^2} + \frac{\partial^2 \phi}{\partial z^2} \end{aligned} \tag{5-14}$$

In addition to satisfying BC's 5-11, Eqn. 5-12 should also satisfy

$$\begin{aligned} &BC's : y = \pm h/2, v_x = 0, \phi = 0 \\ &z = \pm w/2, \phi = -v_x \\ &z = 0, \frac{\partial \phi}{\partial z} = 0 \end{aligned} \tag{5-15}$$

Using these boundary conditions, the solution for the velocity field is

$$v_x(y,z)_{edge\_effect} = \frac{\Delta p h^2}{8\mu L}\left(1-\frac{4y^2}{h^2}\right) - \frac{\Delta p h^2}{8\mu L}\sum_{n=0}^{\infty} \frac{32(-1)^n \cosh\left(\frac{(2n+1)\pi z}{h}\right)\cos\left(\frac{(2n+1)\pi y}{h}\right)}{[(2n+1)\pi]^3 \cosh\left(\frac{(2n+1)\pi w}{2h}\right)} \tag{5-16}$$

Under the assumption that close to surface (height 5 μm over the porous surface (center of the cell)) the shear variation is linear we use Eqn. 5-17 to get obtain an expression for shear stress,

$$\tau_x(y,z)_{edge\_effect} = \mu \frac{v_x(y,z)}{y} \tag{5-17}$$

Eqn. 5-17, describes the reduced shear stress dependence in the Y and Z directions due to edge effects in a microfluidic channel with an aspect ratio of w/h. The resulting normalized shear variations across the channel width for a micro-fluidic channel with aspect ratio of w/h~ 50 and w/h ~ 20 are shown in Fig. 5-11a and fig. 5-11b respectively. For an aspect ratio of 50, the variation in shear stress due to the wall is ~ 2%. However, when the aspect ratio drops down to 20, a decrease of 30% compared to the channel center occurs within 300 μm of the channel edge. Since our channel has a aspect ratio of 20, this implies shear decrease not only along the channel length due to decrease in shear as a result of permeation flux, but also a decrease in shear across the channel width due to the channel edge effect.

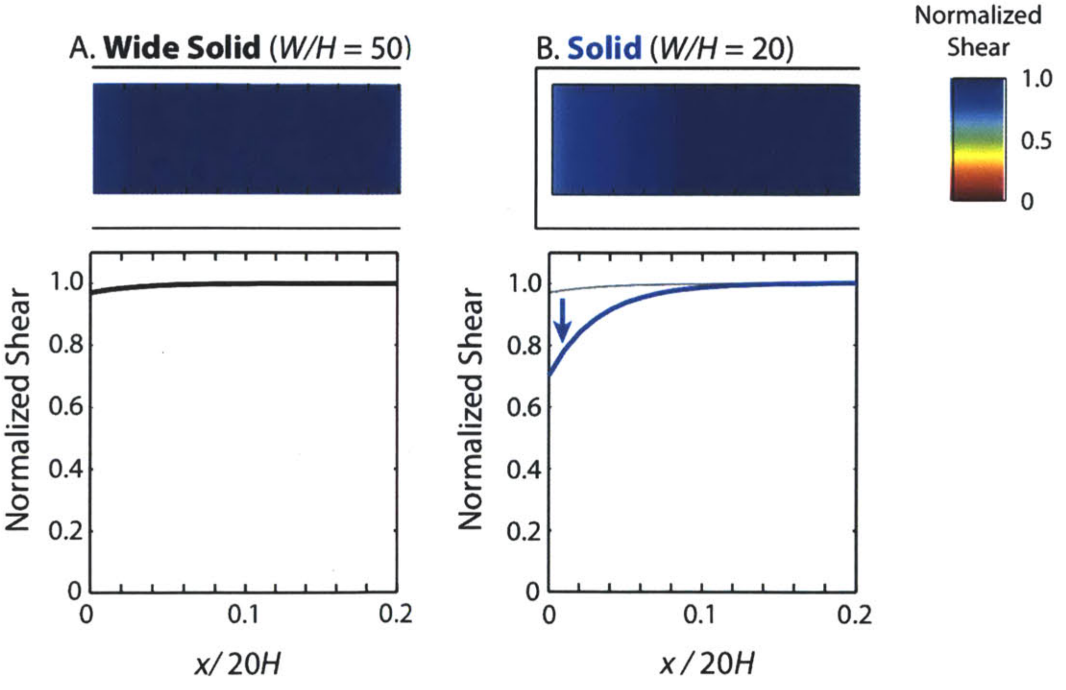

Fig. 5-11 (a) Percentage difference between the shear stress in an infinitely wide channel on a solid surface and on a **(b)** porous surface

5.6 Spatially modulated micro-flows for enhanced cell capture

A number of hydrodynamic mechanisms have been explored to suppress cake formation at high concentrations and throughput, including surface roughness, inertial lift, pulsatile (unsteady) flows, and Dean flows [87]. Unfortunately, these schemes cannot be easily applied to selective separation, since the enhanced local shear could also remove captured target cells. In order to remove the stagnant bio-particle growth at the edges of the channel, we therefore fabricate a spatially modulated microfluidic porous surface device where the surface of the device close to the edges was made solid. The fabrication and integration process for these PDMS channels was similar to the process described in section 3.1 with the top channel dimensions L=4 cm, w=2 mm, and h=100 μm and bottom channel dimensions L=4 cm, w=1.6 mm, and h=100 μm.

5.6.1 Shear variation on a porous and spatially modulated porous surface

As discussed in the previous section, there is a considerable decrease in translational shear close to the channel edges (~30%) even on solid surfaces. This phenomenon is further enhanced on a porous surface where in addition to shear variation across the channel width, the translational shear also decreases along the length. At the channel outlet (x=L) the shear stress at the edges is therefore only 20% of its value at the center for a representative case of A=70% (Fig. 5-12). Therefore if we are operating under the optimized conditions shown previously in Fig. 4-8, the shear along the edge of the channel at the outlet would be 0.3 dyn/cm^2 (20% or 1.5 dyn/cm^2 at x=L in Fig. 5-12). A combination of low translational shear (0.3 dyn/cm^2) and high permeation (A=70%) gives a zero critical distance at the channel end based on Eqn. 5-5 indicating that stagnant layer formation should occur even at ϕ_o~0.01. In order to limit the wall effect we therefore used a partly porous surface. Solid surface at the edges (x=2H ~ 200 μm in our case) pacify the wall effect and pushes the shear back up to the same level as it would be for a solid surface case i.e. 76% of the shear down the center of the channel (Fig. 5-12). Since for x>2H the wall effect is negligible, the center of the channel still benefits from the optimized reduced shear and increased cell-surface interaction on the porous surface.

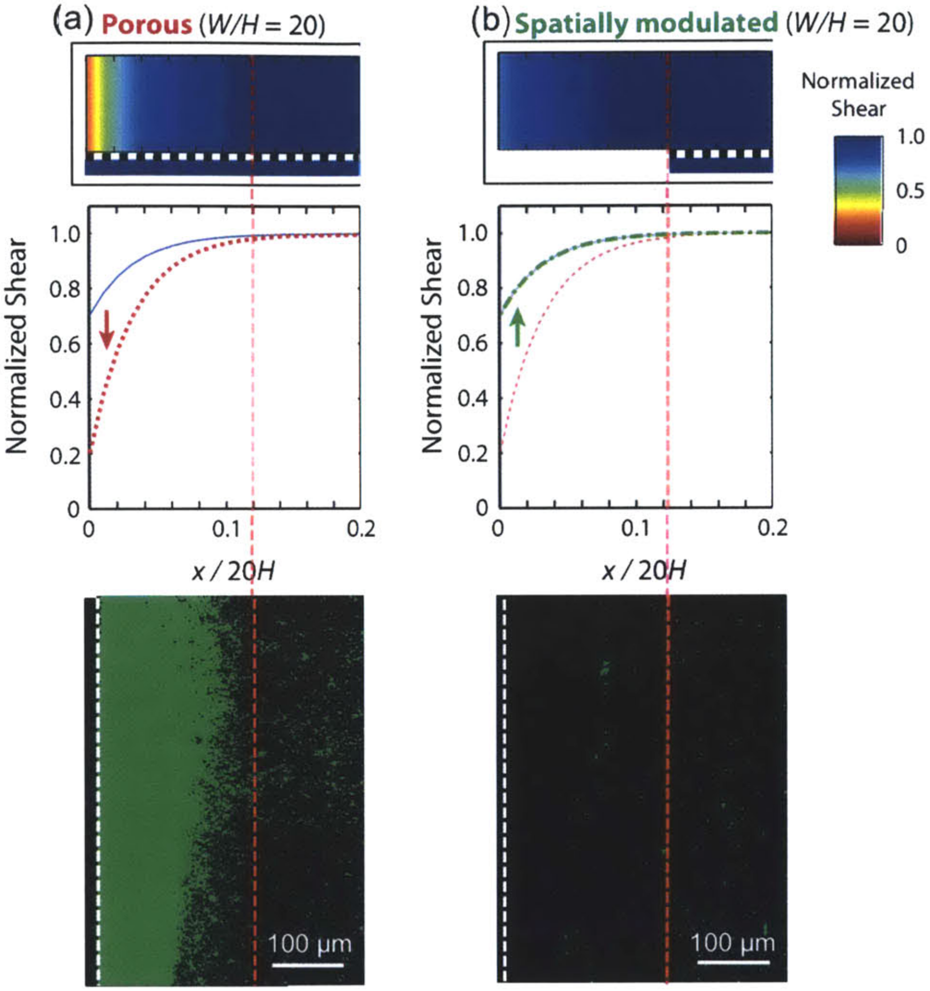

Fig. 5-12 (a) shear variation across the channel width on a porous surface **(b)** on a spatially modulated porous surface, and the corresponding stagnant leukocyte layer (green)

5.6.2 Effect of partly porous surface on stagnant layer formation

In order test and quantify the effect of stagnant layer formation on the surface of the modulated porous surface device we used fluorescently labeled leukocytes and measured the effect of increasing particle fraction on stagnant layer formation over time. The other operating conditions for the experiments included an input flow rate (Qin) ~ 6 mL/h and permeation flux ~ 70%. The fractional area covered was calculated based on the image processing algorithm described in section 5.4.1. It was found that the stagnant layer reduced to less than 10% for the spatially modulated channels as opposed to the completely porous surface counterpart at ϕ_o=0.05 and 0.03 (equivalent of $2.5\text{x}10^6$ cells/mL and $1.5\text{x}10^6$ cells/mL). Various widths of solid surface were tried at the edges, however, the smallest width at with the fractional stagnant layer coverage was found to be ~ 200 μm. Increasing the solid surface width further led to an increase in the number of cells traversing this region without capture, leading to a reduction in the overall capture efficiency.

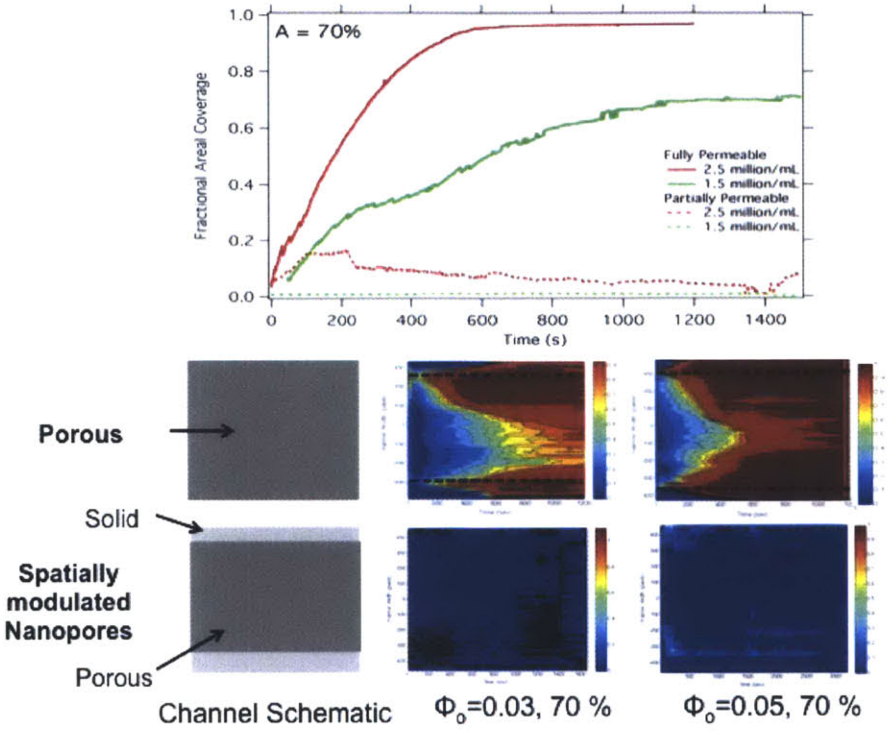

Fig. 5-13 (a) Growth kinetics of the stagnant leukocyte layer on the porous surface on porous and spatially modulated nanoporous surfaces **(b)** Kymographs for the growth curves, show the onset of set across the width of the channel for the two kinds of surfaces at $\phi o=0.05$ and 0.03 and permeation of A=70%.

5.6.3 Specific cell capture efficiency on a spatially modulated porous device

PC3 cells labeled with Cell tracker Orange dye were spiked into buffy coat obtained from human blood through deterministic lateral displacement. The channel surface was functionalized with anti-EpCAM antibody using the protocol mentioned in section 3-1. The PC3 spiked sample was flown into the spatially modulated device at 6 mL/hr for 1 hr at A=70% and $\phi_o \sim 0.03$ and 0.05. The cells were then subsequently fixed and counted using an automated image processing algorithm developed in NIS elements. Capture efficiency of PC3 cells achieved on complimentary anti-EpCAM at $\phi_o=0.03$ is 68% ± 6% and 54% ± 5%at $\phi_o= 0.05$. The capture efficiency on the indented channels was ~ 10 fold higher than its porous counterpart at ϕ_o=0.03 and 9 fold higher at ϕ_o=0.05 (Fig. 5-14). These experiments were repeated 3 times for each condition for mean and standard deviation calculation.

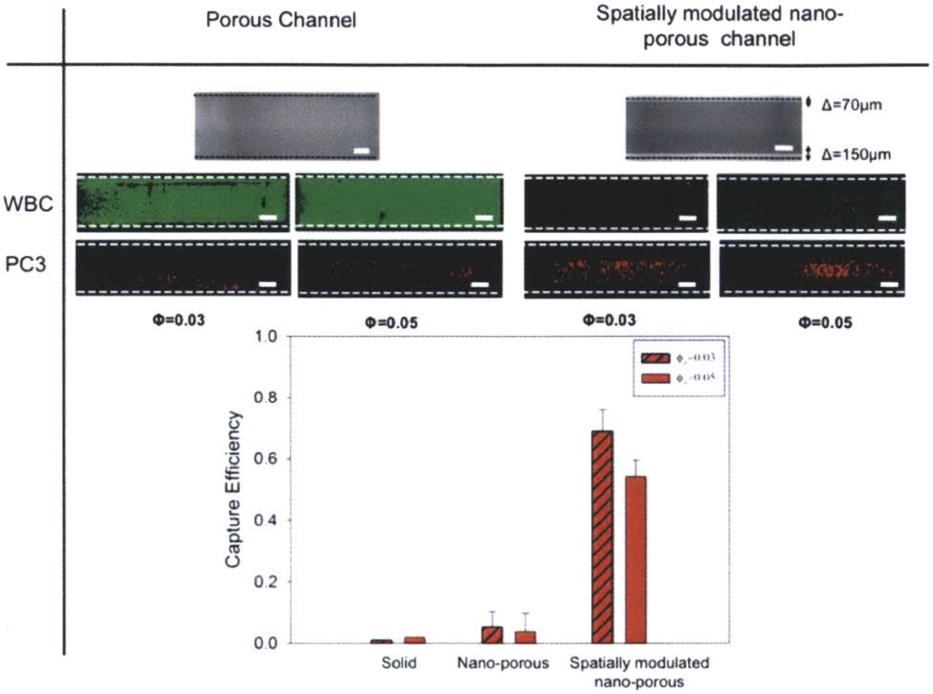

Fig. 5-14 (a) Images of the leukocyte stagnant layer (green) and the target PC3 cell capture (red) on a porous surface **(b)** on partly porous surface **(c)** Capture efficiency comparison on solid, porous and partly porous surface for ϕ_o~ 0.01 and ϕ_o~ 0.03. Scale bar = 500 μm

5.7 High throughput cell capture

Use of partly porous channels reduces the stagnant bio-particle formation on the porous surface and allows for increased input cell feed fraction to be used in the device (ϕ_o~0.05, 5 fold) over its completely porous counterpart (ϕ_o~0.01). This allows for sample processing to be closer to concentrations of "buffy coat" (2.5x10^6 cells/mL) obtained from deterministic lateral displacement method derived from human blood. Given the physical scalability of the current device, we fabricated a 8 parallel channel spatially modulated device using methods described in section 3.1 (Fig. 3-1). The device demonstrated linearly scalability in the sample throughput processed through the device and was capable of processing samples at 48 mL/h, 8 times the flow rate of the single channel mentioned in section 4.8. Therefore, the spatially modulated porous surface immuno-chromatography device offers considerable advantage (~ 10 fold) over the other solid surface immuno-chromatography devices of similar footprint area. Additionally, even at these high sample processing speeds, the device maintains an impressive capture efficiency for low and high expressing cancer cell lines (PC3-9 and H1650 respectively) spiked into buffy coat mixtures. We observe a capture efficiency of ~54% ± 3%, 60% ± 4% and 67% ± 2% for 5, 50 and 500 PC3-9 prostate cancer cells (~ 5000 antigens/cell) spiked into $2.5\text{x}10^6$ WBC's/mL. Similarly, capture efficiency for PC3 prostate cancer cells is 65% ± 6%, 70% ± 4% and 69% ± 5% is seen for 5, 50 and 500 PC3 cancer cells (~ 50,000 antigens/cell) spiked into $2.5\text{x}10^6$ WBC's/mL and 69% ± 3%, 70% ± 3% and 69% ± 5% is seen for 5, 50 and 500 H1650 non small lung cancer cells (~ 250,000 antigens/cell). These results indicate that the device is effective for capturing cells with low antigen expression as well as high antigen expression. Further, large throughput allows processing substantial volumes (48mL) in 1 h thereby making it possible for small number of target cells to be spiked/mL of the sample. Together, these two attributes open up avenues in the future for isolating rare cells from complex samples.

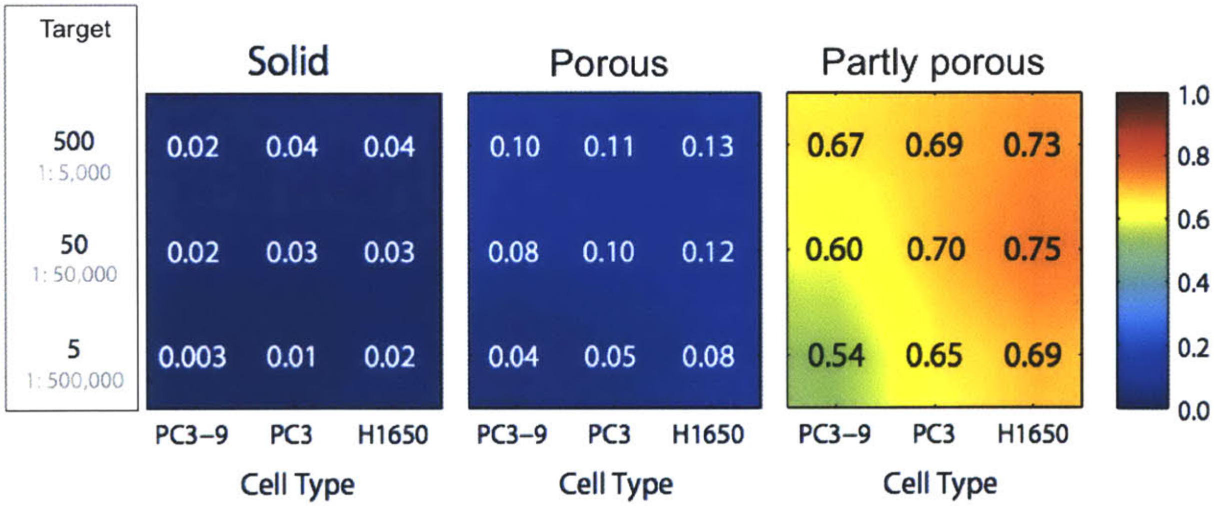

Fig. 5-15 Heat map showing the capture efficiency of PC3 cells in spatially patterned partly porous surface device for different target cell to background cell concentration and cell lines.

5.8 Summary

In this chapter we understood the effect of stagnant leukocyte layer on capture efficiency and critical parameters responsible for its formation. We observe that under optimal specific cell capture parameters (shear ~ 5 dyn/cm^2, A=70%) discussed in chapter 4, the stagnant layer forms above a cell volume fraction of ϕ ~ 0.03 and results in a precipitous drop (~ 68% to ~20%) in capture efficiency once the fractional channel area covered reaches ~ 65%. Additionally we understand that this stagnant layer formation happens over the course of minutes (~ 5 min). Under these circumstances, the device function would be suboptimal as it would stop capturing specific cells. We explored leukocyte layer growth at the edges and middle and found that accelerated stagnant layer growth in our system and found that the onset and growth at the edges is much faster than in the center (~10 fold). Once formed at the edges, the stagnant layer infiltrates inwards and covers the entire channel. We understood the issue of onset of stagnant layer at the edges and found that for low aspect ratio channels the shear at the edges (within ~ 300 μm) decreases by 80%, which creates an imbalance between the translation shear and normal suction force. Insights from the theoretical model were used to design a spatially modulated porous surface device, where the surface close to the walls (~250 μm) was made solid and the rest was porous. This device maintained a substantially high shear (>1.5 dyn/cm^2) at the edges to prevent stagnant layers, while the central channel benefitted from the increased interactions and optimal shear described in chapter 4. Finally, we implemented the concept of partly porous surface for a multiplexed 8 channel device with the capability of processing samples at a flow rate of 48 mL/h.

The ability to multiplex channels allows us to linearly increase the input sample flow rate in proportion with the number of parallel channels. The partly porous microfluidic design approach described in section 5.7 further elucidates the devices capability to process samples at high concentrations without stagnant layer cake formation (Fig. 5-16). A combination of increase in flow rate and increase in initial concentration leads to a total increase in throughput (~150 fold) for capturing specific cells from complex mixtures that are otherwise similar in physical characteristics to the target cells of interest.

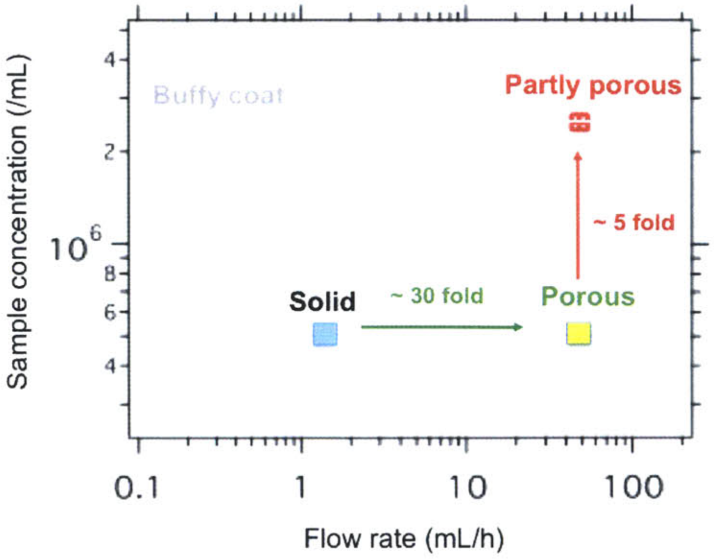

Fig. 5-16 Schematic summary of increase in concentration (~5 fold) of the input sample using a partly porous surface compared to a porous surface while maintaining a capture efficiency of theoretical maximum (~70%).

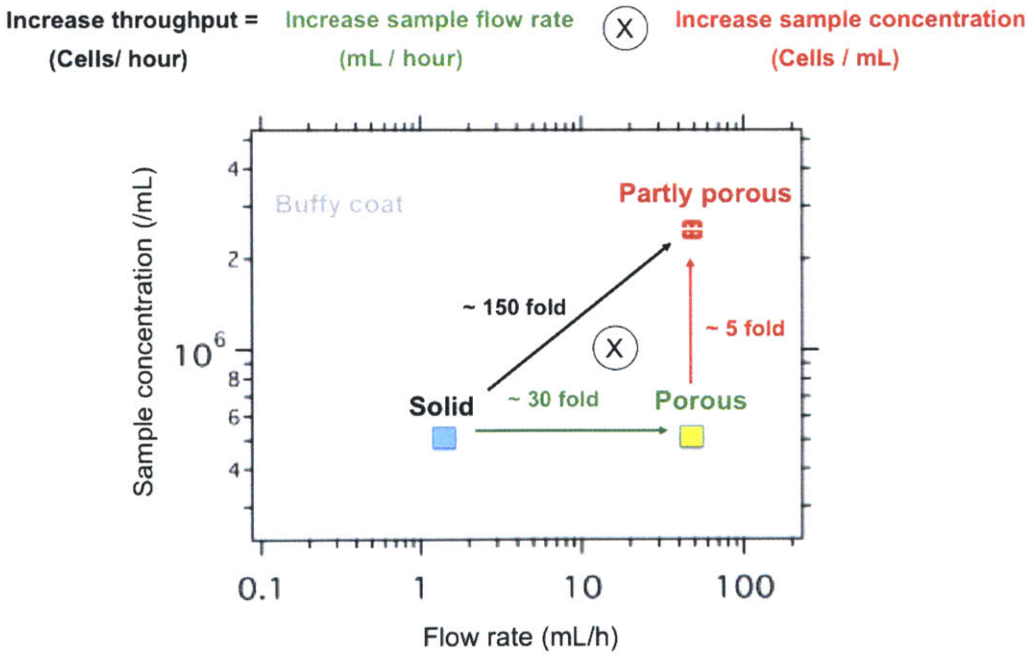

Fig. 5-17 Schematic summary of the total increase in throughput (~150 fold) by increasing flow rate of sample processing (~30 fold) and increasing sample concentration (~5 fold)

Chapter 6

Conclusions and Future Work

6.1 Conclusions

A fluid-permeable capture surface has been demonstrated that overcomes both of these limitations, enabling excellent capture efficiency and selectivity at flow rates 20-fold higher than a comparable device with a solid surface. Remarkably, by controlling the fluid permeation through the membrane, streamlines can be diverted into the membrane even at high flow rates. On a cellular scale, the transverse flux has an additional advantage in that the transverse flow through the membrane significantly decreases the axial fluid flow near the surface. Thus, despite high overall flow rates, cells near the surface experience a considerably diminished shear as well as a "braking" suction force. In contrast, these reduced surface shear conditions can only be achieved near a solid surface at substantially lower flow rates. These transport and cell-surface mechanisms can be independently varied by adjusting the overall flow rate or ratio of transverse to axial flux, respectively, allowing for device operation to be optimized.

In order to reproducibly perform the experiments we developed the lumped resistor model that helped predict the fluid flux through the top and bottom channels of the device by taking into account all the dependent geometrical parameters of the elements in the system (channels and membranes). The use of high resistances at the top and bottom outlets of the device, helped "short out" the variations in the porosity of the membrane, thereby allowing the fluid flux split and the flow rates to be controlled precisely. Further, the use of resistances allowed a constant pressure drop across the membrane which resulted in constant permeation flux through the membrane. Compares to similar systems without these high external resistances, our device was able to bias streamlines and reduce shear along the entire length of the channel.

Conventional platforms based on adhesion-based cell capture on solid surfaces exhibit highly diminished capture efficiency at elevated flow rates due to two coupled mechanisms. The rapid advection of cells through the device limits the transport of cells to the capture surface. As a result, only a small fraction of the total cells in a sample actually reach the surface.

Second, cells near the surface experience strong shear stresses that cause rapid rolling and translation across the surface. The limited interaction between cellular receptors and surface ligands hinders the formation of strong adhesive bonds; any transient bonds that do form are more likely to dissociate at elevated forces. Although the first limitation has been addressed by increasing the capture surface area or enhancing mixing, the second limitation is more difficult to overcome, since the shear stress scales directly with the flow rate near a solid surface. Given this limiting flow rate, the overall throughput can still be increased by scaling up to multiple parallel channels, but this approach soon becomes impractical for device manufacture and readout.

Theoretical and experimental analysis of increased mass transport to the porous surface revealed that there exists a critical state of device operating parameters (Shear stress, input cell volume fraction and permeation flux) beyond which the device starts acting like a mechanical filter. Under these conditions a stagnant layer of leukocytes in the cancer cell spiked sample forms on the cell surface which precludes the target specific cells from interacting with the reactive porous surface. Our analysis showed that once the fractional area covered by the leukocytes reached ~ 60%, there was a precipitous drop in the capture efficiency of the device. It is therefore imperative to understand the mechanics of the stagnant layer formation in order to assuage its formation. We use the critical distance parameter (x_{cr}) to help us estimate the location at which the stagnant layer onset begins and determine the operating conditions such that at steady state the critical distance is greater than the length of the channel. Based on our channel dimensions and previously determined optimal conditions for specific cell capture (shear 5000 s^{-1}, A=70%), we were able to successfully process a sample with $0.5x10^6$ cells/ mL without any bio-particle layer formation. However, as the cell concentration is increased to $1.5x10^6$ cells/ mL we see a layer of leukocytes form. A deeper dive into understanding the kinetics of stagnant layer growth revealed that this stagnant layer formation begins at the edges of the channel and grows inwards. The onset of the cake layer at the edges can be attributed to the substantial shear variation across the width of the microfluidic channels with low aspect ratio ($w/h < 20$). Analysis of the velocity and shear variation showed that on a porous surface the edge effect becomes more pronounced s decreasing the shear at the edges by upto 80% within $x < 2H$. A temporal analysis of the cake layer onset confirms that the onset happens within 250 μm of the channel edge. We therefore establish a complete understanding of the operating conditions under which the porous surface in microfluidic channels would not experience stagnant layer formation.

Based on our understanding of the temporal and steady state formation of stagnant layers and target cell capture, we designed a spatially modulated porous surface that alleviated the decrease in the shear stress at the edges. Solid surface at the edges ($x=2H \sim 200$ μm in our case) pacify the wall effect and pushes the shear back up to the same level as it would be for a solid surface case i.e. 76% of the shear down the center of the channel Since for $x > 2H$ the wall effect is negligible, the center of the channel still benefits from the optimized reduced shear and increased cell-surface interaction on the porous surface. The capture efficiency on the indented channels was ~ 10 fold higher than its porous counterpart at $\phi_o=0.03$ and 9 fold higher at $\phi_o=0.05$. Since the goal of this thesis was to improve throughput of sample processing, we improved the throughput of the device ~ 50 fold over its porous counterpart. Finally, we extended the use of spatially modulated porous surfaces to a microfluidic device with 8 channels in parallel with a throughput capability which scaled linearly. As such we were able to achieve sample processing flow rates of 48 mL/h which allowed us to isolate cancer lines (low and high EpCAM antigen expressing) as low as 5 cells/mL spiked into buffy coat in 1 hr.

6.2 Outlook

Work in this thesis has opened up several new avenues for investigations

As seen in chapter 4, fluid-permeable surfaces is that the shear stress decreases linearly along the length of the channel, reminiscent of microfluidic devices that use a Hele-Shaw channel geometry (with solid surfaces) [117]. As a result, the density of captured cells increases with distance in the channel, since cells are more likely to remain arrested at lower shear. This trend is the opposite of what is often observed on solid surfaces, where the shear is constant and the density of captured cells decreases exponentially along the length of the device [22]. In both cases, the spatial distribution of captured cells reflects how the target subpopulation interacts specifically with an antibody-functionalized surface at a particular shear rate. An intriguing possibility is that additional biophysical information may be encoded in this distribution, such as the variation in receptor expression levels. For instance, circulating tumor cells in a clinical sample may exhibit much greater heterogeneity than a spiked cell line [106], leading to a different distribution of captured cells in the channel. These effects could be explored using improved surface chemistries [118] as well as spatial patterning schemes such as stripes [119], gradients [120], or discrete regions of different capture antibodies [121].

In addition to selective cell capture, microfluidic platforms incorporating porous surfaces may be useful as a well-controlled *in vitro* assay to elucidate cell trafficking behaviors *in vivo*. Indeed, a variety of cell types undergo rolling and arrest *in vivo* in order to be separated from a highly heterogeneous background population [122]. For example, leukocytes are selectively recruited from the circulation to "home in" on sites of inflammation [123], while mesenchymal stem cells participate in organogenesis, wound-healing and natural cell turnover [124]. Similar strategies may be utilized by circulating tumor cells prior to extravasation and metastasic colonization [125, 126]. Many of these behaviors are associated with a porous vasculature, such as capillaries in the bone marrow and discontinuous fenestrated sinusoid cells in the liver [127]. This vascular permeability can be enhanced during acute and chronic inflammation as well as cancer [128]. Although cell rolling and adhesion is frequently observed along sinusoids *in vivo* [129], previous *in vitro* assays have only used solid surfaces to elucidate the biochemical interactions between cellular receptors and surface ligands.

By using porous surfaces with slightly larger pores, it may be possible to delve deeper into the multistep trafficking cascade under biomimetic conditions. In particular, this geometry is highly reminiscent of the transwell/Boyden chamber assay for chemotaxis studies [130]. After capturing cells, the flow conditions in the microfluidic device could be reconfigured to minimize transverse permeation while achieving identical continuous flows in the top and bottom chambers. By loading the bottom chamber with a chemo-attractant solution, a stable gradient would be formed through the membrane, promoting cell migration through the pores. A further step could be to culture a layer of endothelial cells on the porous surface instead of simply patterning ligands [131-133]. By combining biomimetic features with precisely controlled microfluidic flows, it may be possible to recapitulate complex biological behaviors *in vitro*, replicating the dynamics of the leaky vasculature within tumor microenvironments.

Fluid-permeable surfaces represent a powerful and versatile approach for specific analyte capture, overcoming fundamental limitations associated with interfacial effects near solid surfaces [134, 135]. This work has elucidated the physical mechanisms governing both transport and cell-surface interactions in these conditions, establishing engineering design rules for future devices. An exciting prospect is to further increase the performance and utilization of this device by designing and fabricating a tunable microfabricated porous structure that would allow better control over the local and global shear and permeation flux. For example, fabrication of patterned sub-wavelength porous structures in mechanically robust SiN_x films using extremely large electron beam currents has previously been shown . By defining decreasing porosity on the surface, through different sized pores or variable frequencies of pores, it is conceivable to maintain ideal shear along the entire channel length required to capture as opposed to a decreasing shear in non-controllable commercial surfaces. This would lead to a more judicious use of the surface with capture occuring along the entire length. Consequently, the channel length and the channel dimesions can be reduced, which would reduce the area of post sample processing investigation. This capability for efficiently processing hundreds of mL of blood may enable transformative possibilities for point-of-care diagnostics and personalized medicine, such as the capture of extremely rare antigen-specific T-cells or fetal cells. Further, numerous methods available for functionalizing Si with antibody covered biodegradable polymers , opens up possibilities of an integrated capture and release chip from blood [136, 137]. In many applications, it is desirable to release desired bioparticles from the capture surface after isolation, either for downstream culturing or for further counting and sorting.

Bibliography

1. van Reis, R. and A. Zydney, *Bioprocess membrane technology.* Journal of Membrane Science, 2007. **297**(1-2): p. 16-50.
2. Ash, S.R., *Hemofiltration and plasmafiltration devices and methods.* 1999, Google Patents.
3. Fatoyinbo, H.O., K.F. Hoettges, and M.P. Hughes, *Rapid-on-chip determination of dielectric properties of biological cells using imaging techniques in a dielectrophoresis dot microsystem.* Electrophoresis, 2008. **29**(1): p. 3-10.
4. Wang, M.M., et al., *Microfluidic sorting of mammalian cells by optical force switching.* Nature biotechnology, 2004. **23**(1): p. 83-87.
5. Ramadan, Q., D.P. Poenar, and C. Yu, *Customized trapping of magnetic particles.* Microfluidics and nanofluidics, 2009. **6**(1): p. 53-62.
6. Forbes, T.P. and S.P. Forry, *Microfluidic Magnetophoretic Separations of Immunomagnetically Labeled Rare Mammalian Cells.* Lab Chip, 2012.
7. Chen, G.D., et al., *Nanoporous Elements in Microfluidics for Multiscale Manipulation of Bioparticles.* Small, 2011.
8. Nagata, N., et al., *Cross-flow membrane microfiltration of a bacteriol fermentation broth.* Biotechnology and bioengineering, 1989. **34**(4): p. 447-466.
9. Didar, T.F. and M. Tabrizian, *Adhesion based detection, sorting and enrichment of cells in microfluidic Lab-on-Chip devices.* Lab Chip, 2010. **10**(22): p. 3043-3053.
10. Toner, M. and D. Irimia, *Blood-on-a-chip.* Annu. Rev. Biomed. Eng., 2005. **7**: p. 77-103.
11. Pratt, E.D., et al., *Rare cell capture in microfluidic devices.* Chemical Engineering Science, 2011. **66**(7): p. 1508-1522.
12. Greer, J.P. and M.M. Wintrobe, *Wintrobe's clinical hematology.* Vol. 1. 2008: Lippincott Williams & Wilkins.
13. Yu, M., et al., *Circulating tumor cells: approaches to isolation and characterization.* The Journal of Cell Biology, 2011. **192**(3): p. 373.
14. Gossett, D.R., et al., *Label-free cell separation and sorting in microfluidic systems.* Anal. Bioanal. Chem., 2010. **397**(8): p. 3249-3267.
15. Bonner, W.A., et al., *Fluorescence activated cell sorting.* Rev. Sci. Instrum., 1972. **43**(3): p. 404-409.
16. Miltenyi, S., et al., *High gradient magnetic cell separation with MACS.* Cytometry, 1990. **11**(2): p. 231-238.
17. Didar, T.F. and M. Tabrizian, *Adhesion based detection, sorting and enrichment of cells in microfluidic Lab-on-Chip devices.* Lab Chip, 2010. **10**(22): p. 3043-53.
18. Pratt, E.D., et al., *Rare cell capture in microfluidic devices.* Chem. Eng. Sci., 2011. **66**(7): p. 1508-1522.
19. Kotz, K.T., et al., *Clinical microfluidics for neutrophil genomics and proteomics.* Nat. Med., 2010. **16**(9): p. 1038-1043.
20. Sekine, K., et al., *Panning of multiple subsets of leukocytes on antibody-decorated poly(ethylene) glycol-coated glass slides.* J. Immunol. Methods, 2006. **313**(1-2): p. 96-109.
21. Murthy, S.K., et al., *Effect of Flow and Surface Conditions on Human Lymphocyte Isolation Using Microfluidic Chambers.* Langmuir, 2004. **20**(26): p. 11649-11655.

22. Cheng, X., et al., *A microfluidic device for practical label-free CD4(+) T cell counting of HIV-infected subjects.* Lab Chip, 2007. **7**(2): p. 170-178.
23. Plouffe, B.D., et al., *Controlled capture and release of cardiac fibroblasts using peptide-functionalized alginate gels in microfluidic channels.* Lab Chip, 2009. **9**(11): p. 1507-10.
24. Plouffe, B.D., et al., *Development of microfluidics as endothelial progenitor cell capture technology for cardiovascular tissue engineering and diagnostic medicine.* FASEB J., 2009. **23**(10): p. 3309-3314.
25. Narasipura, S.D., et al., *Purification of CD45+ hematopoietic cells directly from human bone marrow using a flow-based P-selectin-coated microtube.* Am. J. Hematol., 2008. **83**(8): p. 627-629.
26. Guo, K.-T., et al., *A New Technique for the Isolation and Surface Immobilization of Mesenchymal Stem Cells from Whole Bone Marrow Using High-Specific DNA Aptamers.* Stem Cells, 2006. **24**(10): p. 2220-2231.
27. Nagrath, S., et al., *Isolation of rare circulating tumour cells in cancer patients by microchip technology.* Nature, 2007. **450**(7173): p. 1235-1239.
28. Stott, S.L., et al., *Isolation of circulating tumor cells using a microvortex-generating herringbone-chip.* Proc. Natl. Acad. Sci. USA, 2010. **107(43)**: p. 18392-18397.
29. Wang, S., et al., *Highly Efficient Capture of Circulating Tumor Cells by Using Nanostructured Silicon Substrates with Integrated Chaotic Micromixers.* Angew. Chem. Int. Ed, 2011. **50**(13): p. 3084-3088.
30. Wang, S., et al., *Three-dimensional nanostructured substrates toward efficient capture of circulating tumor cells.* Angew. Chem. Int. Ed, 2009. **48**(47): p. 8970-8973.
31. Gleghorn, J.P., et al., *Capture of circulating tumor cells from whole blood of prostate cancer patients using geometrically enhanced differential immunocapture (GEDI) and a prostate-specific antibody.* Lab Chip, 2010. **10**(1): p. 27.
32. Phillips, J.A., et al., *Enrichment of Cancer Cells Using Aptamers Immobilized on a Microfluidic Channel.* Anal. Chem., 2009. **81**(3): p. 1033-1039.
33. Stone, H.A., A.D. Stroock, and A. Ajdari, *Engineering Flows in Small Devices.* Annu. Rev. Fluid. Mech., 2004. **36**(1): p. 381-411.
34. Squires, T.M. and S.R. Quake, *Microfluidics: Fluid physics at the nanoliter scale.* Rev. Mod. Phys., 2005. **77**(3): p. 977-1026.
35. Gervais, T. and K.F. Jensen, *Mass transport and surface reactions in microfluidic systems.* Chem. Eng. Sci., 2006. **61**(4): p. 1102-1121.
36. Squires, T.M., R.J. Messinger, and S.R. Manalis, *Making it stick: convection, reaction and diffusion in surface-based biosensors.* Nature Biotechnol., 2008. **26**(4): p. 417-426.
37. Liu, J., et al., *Enhanced Signals and Fast Nucleic Acid Hybridization By Microfluidic Chaotic Mixing.* Angew. Chem. Int. Ed, 2006. **45**(22): p. 3618-3623.
38. Hammer, D.A. and D.A. Lauffenburger, *A dynamical model for receptor-mediated cell adhesion to surfaces.* Biophys. J., 1987. **52**(3): p. 475-487.
39. Hammer, D.A. and M. Tirrell, *Biological adhesion at interfaces.* Annu. Rev. Mater. Sci., 1996. **26**: p. 651-691.
40. Nagrath, S., et al., *Isolation of rare circulating tumour cells in cancer patients by microchip technology.* Nature, 2007. **450**(7173): p. 1235-1239.
41. Kotz, K.T., et al., *Clinical microfluidics for neutrophil genomics and proteomics.* Nature medicine, 2010. **16**(9): p. 1042-1047.

42. Andersen, P., et al., *Specific immune-based diagnosis of tuberculosis.* The Lancet, 2000. **356**(9235): p. 1099-1104.
43. Cheung, M.C., J.D. Goldberg, and Y.W. Kan, *Prenatal diagnosis of sickle cell anaemia and thalassaemia by analysis of fetal cells in maternal blood.* Nature Genetics, 1996. **14**(3): p. 264-268.
44. Leu, W.F. and F. Tiller, *An overview of solid--liquid separation in coal liquefaction processes.* Powder technology, 1984. **40**(1-3): p. 65-80.
45. MacDonald, M., G. Spalding, and K. Dholakia, *Microfluidic sorting in an optical lattice.* Nature, 2003. **426**(6965): p. 421-424.
46. Applegate Jr, R., et al., *Optical trapping, manipulation, and sorting of cells and colloids in microfluidic systems with diode laser bars.* Opt. Express, 2004. **12**(19): p. 4390-4398.
47. Voldman, J., et al., *A microfabrication-based dynamic array cytometer.* Analytical chemistry, 2002. **74**(16): p. 3984-3990.
48. Albrecht, D.R., et al., *Probing the role of multicellular organization in three-dimensional microenvironments.* Nature methods, 2006. **3**(5): p. 369-375.
49. Lapizco-Encinas, B.H., et al., *An insulator-based (electrodeless) dielectrophoretic concentrator for microbes in water.* Journal of microbiological methods, 2005. **62**(3): p. 317-326.
50. Neild, A., et al., *Simultaneous positioning of cells into two-dimensional arrays using ultrasound.* Biotechnology and bioengineering, 2007. **97**(5): p. 1335-1339.
51. Wiklund, M. and H.M. Hertz, *Ultrasonic enhancement of bead-based bioaffinity assays.* Lab Chip, 2006. **6**(10): p. 1279-1292.
52. Norris, J.V., et al., *Acoustic differential extraction for forensic analysis of sexual assault evidence.* Analytical chemistry, 2009. **81**(15): p. 6089-6095.
53. Evander, M., et al., *Noninvasive acoustic cell trapping in a microfluidic perfusion system for online bioassays.* Analytical chemistry, 2007. **79**(7): p. 2984-2991.
54. Huang, L.R., et al., *Continuous particle separation through deterministic lateral displacement.* Science, 2004. **304**(5673): p. 987.
55. Davis, J.A., et al., *Deterministic hydrodynamics: Taking blood apart.* Proceedings of the National Academy of Sciences, 2006. **103**(40): p. 14779.
56. Russom, A., et al., *Differential inertial focusing of particles in curved low-aspect-ratio microchannels.* New journal of physics, 2009. **11**: p. 075025.
57. Di Carlo, D., et al., *Continuous inertial focusing, ordering, and separation of particles in microchannels.* Proceedings of the National Academy of Sciences, 2007. **104**(48): p. 18892.
58. Di Carlo, D., et al., *Equilibrium separation and filtration of particles using differential inertial focusing.* Analytical chemistry, 2008. **80**(6): p. 2204-2211.
59. Hur, S.C., H.T.K. Tse, and D. Di Carlo, *Sheathless inertial cell ordering for extreme throughput flow cytometry.* Lab Chip, 2009. **10**(3).
60. Ashcroft, R.G. and P.A. Lopez, *Commercial high speed machines open new opportunities in high throughput flow cytometry (HTFC).* Journal of immunological methods, 2000. **243**(1-2): p. 13-24.
61. Fu, A.Y., et al., *A microfabricated fluorescence-activated cell sorter.* Nature biotechnology, 1999. **17**(11): p. 1109-1111.
62. Pamme, N., *Magnetism and microfluidics.* Lab Chip, 2005. **6**(1): p. 24-38.

63. Lee, H., A. Purdon, and R. Westervelt, *Manipulation of biological cells using a microelectromagnet matrix.* Applied Physics Letters, 2004. **85**: p. 1063.

64. Zborowski, M., et al., *Red blood cell magnetophoresis.* Biophysical Journal, 2003. **84**(4): p. 2638-2645.

65. Grodzinski, P., et al., *A modular microfluidic system for cell pre-concentration and genetic sample preparation.* Biomedical Microdevices, 2003. **5**(4): p. 303-310.

66. Furdui, V.I. and D.J. Harrison, *Immunomagnetic T cell capture from blood for PCR analysis using microfluidic systems.* Lab Chip, 2004. **4**(6): p. 614-618.

67. Bourgeat-Lami, E. and J. Lang, *Encapsulation of Inorganic Particles by Dispersion Polymerization in Polar Media* 1:: 1. Silica Nanoparticles Encapsulated by Polystyrene.* Journal of colloid and interface science, 1998. **197**(2): p. 293-308.

68. Whitesides, G.M., et al., *Soft lithography in biology and biochemistry.* Annual review of biomedical engineering, 2001. **3**(1): p. 335-373.

69. Didar, T.F., A. Dolatabadi, and R. Wüthrich, *Characterization and modeling of 2D-glass micro-machining by spark-assisted chemical engraving (SACE) with constant velocity.* Journal of Micromechanics and Microengineering, 2008. **18**: p. 065016.

70. Goto, M., et al., *Micro-and nanometer-scale patterned surface in a microchannel for cell culture in microfluidic devices.* Analytical and Bioanalytical Chemistry, 2008. **390**(3): p. 817-823.

71. Cheng, X., et al., *A microfluidic device for practical label-free CD4+ T cell counting of HIV-infected subjects.* Lab Chip, 2006. **7**(2): p. 170-178.

72. Stott, S.L., et al., *Isolation of circulating tumor cells using a microvortex-generating herringbone-chip.* Proc Natl Acad Sci U S A, 2010. **107**(43): p. 18392-7.

73. De Jong, J., R. Lammertink, and M. Wessling, *Membranes and microfluidics: a review.* Lab Chip, 2006. **6**(9): p. 1125-1139.

74. Balasubramanian, K. and M. Burghard, *Chemically functionalized carbon nanotubes.* Small, 2005. **1**(2): p. 180-192.

75. Chen, R.J., et al., *Noncovalent sidewall functionalization of single-walled carbon nanotubes for protein immobilization.* Journal of the American Chemical Society, 2001. **123**(16): p. 3838-3839.

76. Maehashi, K., et al., *Label-free protein biosensor based on aptamer-modified carbon nanotube field-effect transistors.* Analytical chemistry, 2007. **79**(2): p. 782-787.

77. Star, A., et al., *Electronic detection of specific protein binding using nanotube FET devices.* Nano Letters, 2003. **3**(4): p. 459-463.

78. Yu, X., et al., *Protein immunosensor using single-wall carbon nanotube forests with electrochemical detection of enzyme labels.* Mol. Biosyst., 2005. **1**(1): p. 70-78.

79. Bianco, A., K. Kostarelos, and M. Prato, *Applications of carbon nanotubes in drug delivery.* Current Opinion in Chemical Biology, 2005. **9**(6): p. 674-679.

80. Liu, Z., et al., *Carbon nanotubes in biology and medicine: in vitro and in vivo detection, imaging and drug delivery.* Nano research, 2009. **2**(2): p. 85-120.

81. Chirica, G.S. and V.T. Remcho, *Novel monolithic columns with templated porosity.* Journal of Chromatography A, 2001. **924**(1-2): p. 223-232.

82. Chueh, B., et al., *Leakage-free bonding of porous membranes into layered microfluidic array systems.* Analytical chemistry, 2007. **79**(9): p. 3504-3508.

83. Aran, K., et al., *Irreversible, direct bonding of nanoporous polymer membranes to PDMS or glass microdevices.* Lab Chip, 2010. **10**(5): p. 548-552.

84. Kim, J.E., J.H. Cho, and S.H. Paek, *Functional membrane-implanted lab-on-a-chip for analysis of percent HDL cholesterol.* Analytical Chemistry, 2005. **77**(24): p. 7901-7907.
85. Belfort, G., R.H. Davis, and A.L. Zydney, *The behavior of suspensions and macromolecular solutions in crossflow microfiltration.* J. Membr. Sci., 1994. **96**(1-2): p. 1-58.
86. Zeman, L.J. and A.L. Zydney, *Microfiltration and ultrafiltration: principles and applications*. 1996, New York: M. Dekker. 618.
87. Jaffrin, M.Y., *Hydrodynamic Techniques to Enhance Membrane Filtration.* Annu. Rev. Fluid. Mech., 2012. **44**(1): p. 77-96.
88. Moorthy, J. and D.J. Beebe, *In situ fabricated porous filters for microsystems.* Lab Chip, 2003. **3**(2): p. 62-66.
89. Song, S., A.K. Singh, and B.J. Kirby, *Electrophoretic concentration of proteins at laser-patterned nanoporous membranes in microchips.* Analytical chemistry, 2004. **76**(15): p. 4589-4592.
90. Cui, T., et al., *Fabrication of microreactors for dehydrogenation of cyclohexane to benzene.* Sensors and Actuators B: Chemical, 2000. **71**(3): p. 228-231.
91. Karnik, S.V., M.K. Hatalis, and M.V. Kothare, *Towards a palladium micro-membrane for the water gas shift reaction: Microfabrication approach and hydrogen purification results.* Microelectromechanical Systems, Journal of, 2003. **12**(1): p. 93-100.
92. Cabodi, M., et al., *A microfluidic biomaterial.* Journal of the American Chemical Society, 2005. **127**(40): p. 13788-13789.
93. Ismagilov, R.F., et al., *Microfluidic arrays of fluid-fluid diffusional contacts as detection elements and combinatorial tools.* Analytical chemistry, 2001. **73**(21): p. 5207-5213.
94. Xu, N., et al., *A microfabricated dialysis device for sample cleanup in electrospray ionization mass spectrometry.* Analytical chemistry, 1998. **70**(17): p. 3553-3556.
95. Duffy, D.C., et al., *Rapid prototyping of microfluidic systems in poly (dimethylsiloxane).* Analytical chemistry, 1998. **70**(23): p. 4974-4984.
96. Eddings, M.A., M.A. Johnson, and B.K. Gale, *Determining the optimal PDMS–PDMS bonding technique for microfluidic devices.* Journal of Micromechanics and Microengineering, 2008. **18**: p. 067001.
97. Bora, U., et al., *Photochemical activation of a polycarbonate surface for covalent immobilization of a protein ligand.* Talanta, 2006. **70**(3): p. 624-629.
98. Xu, Q. and K.S. Lam, *Protein and chemical microarrays-powerful tools for proteomics.* Journal of Biomedicine and Biotechnology, 2003. **2003**: p. 257-266.
99. Kennedy, J.F. and I.M. Kay, *The use of titanium (IV) oxide for the immobilisation of carbohydrate-directed enzymes.* Carbohydrate Research, 1977. **56**(2): p. 211-218.
100. Suye, S., Y. Kumon, and A. Ishigaki, *Immobilization of glucose oxidase on poly-(L-lysine)-modified polycarbonate membrane.* Biotechnology and applied biochemistry, 1998. **27**(3): p. 245-248.
101. Davis, J.A., et al., *Deterministic hydrodynamics: taking blood apart.* Proc. Natl. Acad. Sci. USA, 2006. **103**(40): p. 14779-14784.
102. Munn, L.L., R.J. Melder, and R.K. Jain, *Analysis of cell flux in the parallel plate flow chamber: implications for cell capture studies.* Biophys. J., 1994. **67**(2): p. 889-895.
103. Goldman, A.J., R.G. Cox, and H. Brenner, *Slow viscous motion of a sphere parallel to a plane wall--II Couette flow.* Chem. Eng. Sci., 1967. **22**(4): p. 653-660.

104. Goldman, A., R. Cox, and H. Brenner, *Slow viscous motion of a sphere parallel to a plane wall--I Motion through a quiescent fluid.* Chemical Engineering Science, 1967. **22**(4): p. 637-651.
105. Goetz, D.J., et al., *Dynamics of neutrophil rolling over stimulated endothelium in vitro.* Biophysical Journal, 1994. **66**(6): p. 2202-2209.
106. Yu, M., et al., *Circulating tumor cells: approaches to isolation and characterization.* J. Cell. Biol., 2011. **192**(3): p. 373-382.
107. Chang, K.C. and D.A. Hammer, *The forward rate of binding of surface-tethered reactants: effect of relative motion between two surfaces.* Biophysical Journal, 1999. **76**(3): p. 1280-1292.
108. Bell, G.I., M. Dembo, and P. Bongrand, *Cell adhesion. Competition between nonspecific repulsion and specific bonding.* Biophysical Journal, 1984. **45**(6): p. 1051-1064.
109. Bell, G.I., *Models for the specific adhesion of cells to cells.* Science, 1978. **200**(4342): p. 618-627.
110. Loberg, R.D., et al., *Detection and isolation of circulating tumor cells in urologic cancers: a review.* Neoplasia (New York, NY), 2004. **6**(4): p. 302.
111. Braun, S. and C. Marth, *Circulating Tumor Cells in Metastatic Breast Cancer—Toward Individualized Treatment?* New England Journal of Medicine, 2004. **351**(8): p. 824-826.
112. Mittal, S., et al., *Antibody-Functionalized Fluid-Permeable Surfaces for Rolling Cell Capture at High Flow Rates.* Biophys. J., 2012. **102**(4): p. 721-730.
113. Romero, C.A. and R.H. Davis, *GLOBAL-MODEL OF CROSS-FLOW MICROFILTRATION BASED ON HYDRODYNAMIC PARTICLE DIFFUSION.* Journal of Membrane Science, 1988. **39**(2): p. 157-185.
114. Leighton, D. and A. Acrivos, *The shear-induced migration of particles in concentrated suspensions.* Journal of Fluid Mechanics, 1987. **181**(1): p. 415-439.
115. Romero, C.A. and R.H. Davis, *Global model of crossflow microfiltration based on hydrodynamic particle diffusion.* J. Membr. Sci., 1988. **39**(2): p. 157-185.
116. Davis, R.H., *Modeling of fouling of crossflow microfiltration membranes.* Separation and purification methods, 1992. **21**(2): p. 75-126.
117. Usami, S., et al., *Design and construction of a linear shear stress flow chamber.* Ann. Biomed. Eng., 1993. **21**(1): p. 77-83.
118. Hong, S., et al., *Covalent immobilization of p-selectin enhances cell rolling.* Langmuir, 2007. **23**(24): p. 12261-12268.
119. Karnik, R., et al., *Nanomechanical control of cell rolling in two dimensions through surface patterning of receptors.* Nano Lett., 2008. **8**(4): p. 1153-1158.
120. Herman, C.T., et al., *Probing dynamic cell–substrate interactions using photochemically generated surface-immobilized gradients: application to selectin-mediated leukocyte rolling.* Integr. Biol., 2011. **3**: p. 779-791.
121. Myung, J.H., et al., *Enhanced Tumor Cell Isolation by a Biomimetic Combination of E-selectin and anti-EpCAM: Implications for the Effective Separation of Circulating Tumor Cells (CTCs).* Langmuir, 2010. **26**(11): p. 8589-8596.
122. Mcever, R.P. and C. Zhu, *Rolling cell adhesion.* Annu. Rev. Cell Dev. Biol., 2010. **26**: p. 363-396.
123. Luster, A.D., R. Alon, and U.H. von Andrian, *Immune cell migration in inflammation: present and future therapeutic targets.* Nature Immunol., 2005. **6**(12): p. 1182-1190.

124. Laird, D.J., U.H. von Andrian, and A.J. Wagers, *Stem cell trafficking in tissue development, growth, and disease.* Cell, 2008. **132**(4): p. 612-630.
125. Wirtz, D., K. Konstantopoulos, and P.C. Searson, *The physics of cancer: the role of physical interactions and mechanical forces in metastasis.* Nature Rev. Cancer, 2011. **11**: p. 512.
126. Shibue, T. and R.A. Weinberg, *Metastatic colonization: Settlement, adaptation and propagation of tumor cells in a foreign tissue environment.* Semin Cancer Biol, 2011. **21**(2): p. 99-106.
127. Jain, R.K., *Determinants of tumor blood flow: a review.* Cancer Res., 1988. **48**(10): p. 2641-2658.
128. Nagy, J.A., et al., *Vascular permeability, vascular hyperpermeability and angiogenesis.* Angiogenesis, 2008. **11**(2): p. 109-119.
129. Mazo, I.B., et al., *Hematopoietic progenitor cell rolling in bone marrow microvessels: parallel contributions by endothelial selectins and vascular cell adhesion molecule 1.* J. Exp. Med., 1998. **188**(3): p. 465-474.
130. Boyden, S., *The chemotactic effect of mixtures of antibody and antigen on polymorphonuclear leucocytes.* J. Exp. Med., 1962. **115**: p. 453-466.
131. Huh, D., et al., *Reconstituting organ-level lung functions on a chip.* Science, 2010. **328**(5986): p. 1662-1668.
132. Srigunapalan, S., et al., *A microfluidic membrane device to mimic critical components of the vascular microenvironment.* Biomicrofluidics, 2011. **5**(1): p. 013409.
133. Song, J.W., et al., *Microfluidic Endothelium for Studying the Intravascular Adhesion of Metastatic Breast Cancer Cells.* PLOS ONE, 2009. **4**(6): p. e5756.
134. Yanik, A.A., et al., *Integrated nanoplasmonic-nanofluidic biosensors with targeted delivery of analytes.* Appl. Phys. Lett., 2010. **96**(2): p. 021101.
135. Chen, G.D., et al., *Nanoporous Elements in Microfluidics for Multiscale Manipulation of Bioparticles.* Small, 2011. **7**(8): p. 1061-1067.
136. Plouffe, B.D., et al., *Controlled capture and release of cardiac fibroblasts using peptide-functionalized alginate gels in microfluidic channels.* Lab on a Chip, 2009. **9**(11): p. 1507-1510.
137. Zhu, J., et al. *Specific cell capture and temperature-mediated release using surface-immobilized aptamers in a microfluidic device*. 2011: IEEE.